Submitted in accordance with the requirements for the degree of
Doctor of Philosophy

UNIVERSITY OF LEEDS

SCHOOL OF PHYSICS & ASTRONOMY

Quantum metrology with Bose-Einstein condensates

Jessica Jane Cooper

March 2011

The candidate confirms that the work submitted is her own, except where work which has formed part of jointly-authored publications has been included. The contribution of the candidate and the other authors to this work has been explicitly indicated below. The candidate confirms that the appropriate credit has been given within the thesis where reference has been made to the work of others.

Several chapters within this thesis are based on work from jointly-authored publications as detailed below:

Chapter 5 - Based on work published in Journal of Physics B 42 105301 titled 'Scheme for implementing atomic multiport devices'. This work was completed with my supervisor Jacob Dunningham and a postdoctoral researcher David Hallwood.

Chapter 6 - Based on work published in Physical Review A 81 043624 titled 'Entanglement enhanced atomic gyroscope'. Again, this work was completed with Jacob Dunningham and David Hallwood.

Chapter 7 - The research presented in this chapter has recently been added to a pre-print server [arxiv:1101.3852] and will be soon submitted to a peer-reviewed journal. It is titled 'Robust Heisenberg limited phase measurements using a multimode Hilbert space' and was completed during a visit to Massey University where I collaborated with David Hallwood and his current supervisor Joachim Brand.

Chapter 8 - Based on work completed with Jacob Dunningham which has recently been submitted to New Journal of Physics. It is titled 'Towards improved interferometric sensitivities in the presence of loss'.

For all the above work I was the main contributor to the research but sought assistance and guidance from the other authors. The results of Chapter 7, however, contain some numerical results which were obtained using code written in MATLAB. There were two main sections of code (one to create the initial wavefunction and one to model particle losses from the system) one of which was written by David Hallwood (the initial wavefunction code) and the other by myself (the loss code).

Acknowledgements

I would like to begin by thanking Jacob Dunningham for his supervision during my PhD. He has provided me with an interesting project and has always been around to help me work through the many problems I have encountered due to my lack of understanding. He has patiently answered my repeated questions and his knowledge and passion for physics have often inspired me.

I would also like to thank David Hallwood for answering all my trivial questions. He too provided me with an interesting project as the work presented in Chapter 7 is the result of his idea. I must also take a moment to thank both David and his current supervisor, Joachim Brand, for their hospitality on a visit to Massey University. They both made me feel very welcome and some promising results were obtained from this visit.

On non-project related matters I would like to thank Neil Lovett for some great times over the last few years. He has been, and I'm sure will continue to be, a great friend - it has been a lot of fun sharing an office. I am especially grateful for the welcome distractions from thesis writing and the many games of WordTwist we have enjoyed. Neil has also patiently helped me with my computing problems and taught me many valuable computing related skills. I must also thank all the other members of the QI group, in particular, Michal, Andreas and Jonathan for some fun times.

Finally, I would like to thank my friends and family for their continued support and belief in me. A special thank you must go to Simon who has, as well as showing interest in my work, put up with my worries about my PhD. He has provided great encouragement throughout.

Abstract

The ability to make ultra-precise measurements is fundamentally important to science as it allows theories to be tested and refined. Interferometers offer unrivalled measurement precision and therefore form the basis of many metrology schemes. Research has shown that by using quantum states as inputs to interferometers, precisions better than anything possible classically can be achieved. Nevertheless, these states are difficult to produce and fragile to particle losses. Consequently, classical inputs, which are extremely robust, are used in experiments. Here, however, we propose experimentally accessible schemes to make quantum-limited measurements, in particular rotation measurements using Bose-Einstein condensates, that are robust to losses.

We begin by describing how, by loading a Bose-Einstein condensate into an optical ring lattice, multiport beam splitters are created through a simple raising and lowering of potential barriers between sites. We then use these 'splitters' to create an atomic gyroscope. We demonstrate how to create several quantum states in the gyroscope, all capable of making rotation measurements. Whilst NOON states afford best precision in idealised set-ups, we find they are outperformed by 'bat' states for modest loss rates.

However, bat states are not ideal as they are outperformed by classical states for large losses. A second gyroscope scheme is therefore developed. Using multiple momentum modes, rather than just two, we show quantum-limited precisions can be reached using states that have similar robustness to classical states.

The final section focuses on the precision of linear interferometers. Recent work

[1, 2] has calculated the theoretical optimum initial states for two-mode lossy interferometers. Here we present an experimental way to produce initial states that afford similar precisions to this optimum. We also consider lossy multimode interferometry and demonstrate a potential advantage over two-mode systems. It is thought with further investigation other advantages will be found.

Thesis publications

1. 'Towards improved interferometric sensitivities in the presence of loss', J. J. Cooper and J. A. Dunningham, submitted to New Journal of Physics (2011).

2. 'Quantum metrology with rotating matter waves in different geometries', J. A. Dunningham, J. J. Cooper and D. W. Hallwood, arxiv:1102.0164 (2011).

3. 'Robust Heisenberg limited phase measurements using a multimode Hilbert space', J. J. Cooper, D. W. Hallwood and J. Brand, arxiv:1101.3852 (2011).

4. 'Entanglement enhanced atomic gyroscope', J. J. Cooper, D. W. Hallwood and J. A. Dunningham, Physical Review A **81**, 043624 (2010).

5. 'Measuring atomic NOON states and using them to make measurements', D. W. Hallwood, A. Stokes, J. J. Cooper and J. A. Dunningham, New Journal of Physics **11**, 103040 (2009).

6. 'Scheme for implementing atomic multiport devices', J. J. Cooper, D. W. Hallwood and J. A. Dunningham, Journal of Physics B **42**, 105301 (2009).

7. 'Single particle nonlocality with completely independent reference states', J. J. Cooper and J. A. Dunningham, New Journal of Physics **10**, 113024 (2008).

Contents

List of Figures

Chapter 1

Introduction

1.1 The classical and quantum worlds

Ever since quantum mechanics was first conceived differences between the quantum and classical world have been evident. Perhaps one of the greatest differences is the existence of superpositions in the quantum world and lack thereof in the classical world. This difference was emphasised by Schrödinger in 1935 in his famous thought experiment [3] where, in an attempt to highlight the bizarreness of quantum mechanics, he demonstrated how quantum theory allows a cat to be in a superposition of being dead and alive at the same time, something that we never observe in the everyday classical world.

The thought experiment is as follows: a cat is put into a box with a radioactive atom. Over the course of an hour the atom may decay, but also, with equal probability, it may not. If it does decay, some form of radiation is emitted that can be detected. Detection of such radiation triggers a vial of poison to be smashed and the cat dies. However, if the atom does not decay the vial remains intact and the cat survives. If the box is left for an hour the radioactive atom, which is a quantum object, will be in an equal superposition of decayed and not decayed. The cat, whose state depends on the state of the radioactive atom, is therefore said to be in a superposition of being alive and dead. We never actually see cats that are in

such a superposition, nevertheless this scenario is allowed by quantum mechanics. The experiment, therefore, clearly highlights just one of many differences between classical and quantum physics.

Another nice demonstration of a difference between the quantum and classical world is given by the double slit experiment in which a beam of electrons is fired at a screen containing two slits [4, 5]. A second screen that contains detectors which can record when an electron strikes a given point is placed behind the first screen. Classically an electron is considered a localised particle and therefore each one can pass through only one slit. The resulting intensity of electrons detected on the second screen will therefore be the sum of the intensity of electrons passing through each individual slit. In experiments, however, this is not what is found. Instead an interference pattern is observed which can only be explained by treating the electrons as waves. However, on detection every electron exhibits purely particle like properties as each electron is localised at a particular detector. And so, in just one experiment, both the particle and wave like properties of the electrons have been observed. The fact that all matter exhibits both wave and particle properties is central to quantum physics. It is very different from our classical interpretation of an electron existing as a localised particle.

We note the same interference pattern has also been shown to exist when single electrons are passed through the slits one at a time [6]. This confirms that the interference is due to the interaction of the electron and the slits, not due to interactions between different electrons. We also note that closing one of the slits destroys the interference pattern leading us to conclude that the electron must be in a superposition of having passed through both slits when interference is observed. The results of this experiment are impossible to explain using the laws of classical physics and lead to Feynman's famous quote that the single electron double slit experiment "has in it the heart of quantum mechanics, In reality, it contains the only mystery".

The aim of the field of quantum information research is to exploit the differences between quantum and classical physics to, for example, speed up certain computa-

tions [7], teleport information between spatial locations [8] and ensure the secure transmission of information [9]. Another consequence of these differences is the potential to use quantum physics to improve the precision of measurements beyond what is possible classically. This field of research is known as quantum metrology and will be the focus of this thesis. A detailed introduction to the field will be given in Chapter 3. For now we provide a quick overview but first we must introduce another peculiarity of the quantum world, the uncertainty principle.

1.1.1 The uncertainty principle

The Heisenberg uncertainty principle, formulated by W. Heisenberg in 1927 [10], is one of the most well known ideas of quantum physics. It states that certain pairs of physical properties of a system, such as position and momentum, cannot be simultaneously known to arbitrarily high precision. For the particular case of a particle's position, x, and momentum, p, the uncertainty relation takes the form

$$\Delta x \Delta p \geq \frac{\hbar}{2} \tag{1.1}$$

from which it is clear that reducing the uncertainty in the position (momentum) of a particle leads to an increase in the uncertainty of its momentum (position).

Heisenberg demonstrated this relation through a simple thought experiment in which one attempts to measure the position of a particle as precisely as possible by illuminating it with light of wavelength λ and observing the image through a microscope. Using classical optics the microscope can resolve the position of the particle to a precision of

$$\Delta x = \frac{\lambda}{\sin \theta_m} \tag{1.2}$$

where θ_m is the angular aperture of the microscope. Consequently, we see that the uncertainty in the position measurement can be reduced by using light of a shorter wavelength. However, in order to make the measurement we know that at least one photon must scatter from the particle into the microscope. This scattering

imparts a recoil momentum to the particle which is proportional to the momentum of the photon. But this recoil momentum cannot be determined exactly since the direction of the scattered photon can only be determined to within an angle θ_m. The momentum of the particle can therefore be determined to a precision of

$$\Delta p_x \simeq p \sin\theta_m = \frac{h}{\lambda} \sin\theta_m. \tag{1.3}$$

From these equations we see $\Delta x \Delta p_x \simeq \hbar$ and so whilst using light of shorter wavelength leads to a reduction in the uncertainty in the position measurement, this is accompanied by an increase in the uncertainty of the momentum measurement.

Similar uncertainty relations exist for other pairs of variables. In fact it can be shown that for any two Hermitian operators Q and R

$$\Delta q \Delta r \geq \frac{1}{2} \left| \langle [Q, R] \rangle \right|. \tag{1.4}$$

The uncertainties Δq and Δr are not experimental errors but instead refer to the average spread of a set of repeated measurements of q and r, that is, they are the best predictions we can make about the outcome of an experiment. As will be discussed here (and in more detail in Chapter 3) this has very important consequences in quantum metrology.

1.2 Quantum metrology

Metrology, the science of measurement, is central to our everyday lives as we are constantly making measurements of our surroundings through observations. In fact most of us are obsessed with measurements - we 'need' to know the time, the speed of our internet connection, the temperature, the list goes on. Science allows us to make these measurements and, over time, advances in science have enabled these measurements to become more and more precise. The ability to make precise measurements is of considerable importance to a huge variety of people. A pilot, for example, must know the precise position of their aircraft in order to prevent mid-air

collisions. Advances in science have led to the development of ultra-precise gyroscopes and accelerometers thereby rendering this possible.

It is easy to see why as scientific methods improve more precise measurements can be made. The converse, however, is also true. That is, as measurements become more precise improvements are made to science as, for example, the ability to make more precise measurements allows scientific theories to be proved/disproved. Indeed, many scientific theories have failed to stand up to the results of precise measurements. The existence of the 'ether', for example, was famously disproved when Michelson and Morely made precise interferometric measurements. Consequently finding ways to improve measurement precision is of fundamental importance to all areas of science. With this in mind a great deal of research has been, and continues to be, concentrated on precisely this.

As we have said, advances in science tend to lead to improvements in measurement precision. The relatively recent advent of quantum physics is proving to be no exception to this rule as theory predicts quantum systems should allow physical quantities to be measured with much greater precision than is possible classically. Indeed, proof of principal experiments have already been performed demonstrating the potential of quantum physics to improve measurement precision [11]. Nevertheless the true potential of quantum systems for making ultra-precise measurements, as predicted by the theory, remains unseen in experiments as of yet. This is largely due to the difficulties associated with producing the required quantum set-up and will be discussed later in the thesis. For now we give an intuitive feel as to why quantum physics allows for such vast improvements in measurement precision.

Measurement is a physical process and as such the precision of a measurement is governed by the laws of physics. Since we know that the classical and quantum laws of physics differ considerably this immediately suggests that the precision of classical measurements will be different to the precision of quantum measurements.

To understand the precision capabilities of measurements governed by the laws of classical physics we consider a simple statistical experiment in which a fair coin

is tossed N times and the result of the toss (head or tails) is recorded. After the coin has been tossed a great many number of times we would expect the number of heads and tails that are recorded to differ by a small percentage. If, however, N is small there may be a significantly disproportionate number of heads or tails. Therefore if we repeat the N tosses several times we would expect the results to fluctuate a lot between each run for small values of N. And so we see that the larger N the more reproducible, or the more precise, our results become. It can be, and will be (in Chapter 3), shown that the precision in fact scales as $1/\sqrt{N}$. This same scaling is found for all independent events and is due to the discrete nature of the measurement outcomes. It presents a limit to the precision attainable given a fixed number of resources. This limit is called the standard quantum limit and represents the best precision that can be achieved in a classical system. Nevertheless there is a way to improve measurement precision beyond this limit by exploiting quantum systems.

Quantum systems are governed by the laws of quantum physics and as such it is Heisenberg's uncertainty relation that places a limit on the precision to which measurements can be made in these systems. So if, for example, we know the position of a particle to a precision of Δx the uncertainty in its momentum can be no less than $\hbar/(2\Delta x)$. It can be shown that for a system consisting of N objects fluctuations in the observable that is to be measured can be made to scale as $1/N$ in a quantum system and that this is the ultimate precision allowed by quantum physics [12]. This is a $1/\sqrt{N}$ improvement in precision over the classically equivalent system and is due to the fact that in a quantum system objects can be made to have correlations that are not possible classically. So instead of having discrete measurement outcomes where each coin, for example, acts independently of the other $N-1$ coins, in a quantum system the coins 'share' information with one another. Nevertheless, achieving this scaling experimentally remains challenging due to the high degree of control and isolation of the system from the environment that is required. As such most precision measurement experiments to date rely on

classical physics.

This thesis focusses on the precision of interferometric measurements as interferometers offer unrivalled precision for the measurement of phase shifts. These devices also allow for an easy way to see the potential of quantum physics to improve measurement precision from the $1/\sqrt{N}$ scaling to the $1/N$ scaling and are discussed at length in Chapter 3. We now give a detailed thesis aim and overview.

1.3 Thesis aim

The primary aim of this thesis is to determine ways quantum states can be used to improve the precision of interferometric phase measurements, in particular those corresponding to rotation rates. We restrict our investigation to ways to improve precision solely by optimising the initial quantum state of the interferometer (readout methods are beyond the scope of this thesis and will be only briefly mentioned). Particular attention will be paid to the effects of particle loss on interferometric precision. Ultimately we aim to find initial states that allow for precise measurements even when particle losses are accounted for. We also wish to determine ways to create such states in an experimentally realistic set-up.

We focus our attention on creating quantum states with Bose-Einstein condensates as, when loaded into an optical lattice, a high degree of control of the system variables is experimentally feasible. Using atoms, rather than light, will prove particularly advantageous when we wish to measure rates of rotation.

1.4 Thesis overview

The structure of the thesis is as follows. Chapter 2 introduces the theory of Bose-Einstein condensates necessary to understand the thesis, in particular, the theory of a Bose-Einstein condensate confined to an optical lattice. Such a system is described by the Bose-Hubbard model [13] which is discussed in detail in this chapter. Central to the thesis is the effect of rotations on a Bose-Einstein condensate in a ring lattice.

The corresponding rotating Bose-Hubbard model is introduced towards the end of the chapter.

Chapter 3 is the second of three introductory theory chapters. It looks at the Mach-Zehnder interferometer and how it can be used to make precise phase measurements. A way to quantify the precision of these phase measurements is introduced and the precision capabilities of several different quantum states are determined. Finally the effects of particle loss on the precision of phase measurements are considered. We introduce a simple way to model particle losses and demonstrate the extreme fragility of certain quantum states.

In Chapter 4 we demonstrate how linear interferometers can be implemented in ring geometries to make precise measurements of rotation rates. We focus on the Sagnac geometry [14] and demonstrate how different quantum states achieve different precisions in this setting. Here we provide motivation for our use of atoms rather than light to make our rotation measurements in the proceeding work. The remaining chapters (excluding 'conclusion and future work') present original work completed during the course of my PhD.

Chapter 5 presents work completed with Jacob Dunningham and David Hallwood published in Journal of Physics B [15]. We show how, by loading a Bose-Einstein condensate into an optical ring lattice of S sites, multiport beam splitting operations can be performed on the condensate simply by changing the intensity of the trapping laser light. The scheme is theoretically simple and, as we demonstrate, is within reach of current experimental techniques. This work was largely motivated by its potential to create entangled states in a ring geometry, making it an ideal resource for ultra-precise atomic gyroscope schemes. Indeed, the three port beam splitter described here is central to the atomic gyroscope in the next chapter.

The first of two atomic gyroscope schemes is introduced in Chapter 6. Once again we consider a Bose-Einstein condensate loaded into an optical ring lattice. This time, however, we consider a ring of just three lattice sites (the minimum number of sites required to create a ring). We demonstrate how, using simple beam

splitting operations, the atoms can be made to be in a superposition of flowing in opposite directions around the ring. We show how this then allows us to measure some external rotation rate. Ways to create different rotating superpositions are considered and the precision afforded by each initial superposition is determined both in the presence of and absence of particle loss. We find that whilst quantum limited precisions can be achieved, the states that afford these precisions are extremely fragile to the effects of particle loss. This work was completed with Jacob Dunningham and David Hallwood and is published in Physical Review A [16].

The work presented in Chapter 7 is the result of a visit to Massey University and was completed with David Hallwood and Joachim Brand [17]. Within this chapter a second atomic gyroscope scheme is presented. As before we load a Bose-Einstein condensate into an optical potential. This time, however, we use a continuous optical ring potential with a single barrier rather than a ring of lattice sites. We show how, through the use of multiple momentum modes, rather than just two as for the gyroscope scheme of Chapter 6, quantum limited precision rotation measurements can be made that demonstrate unprecedented robustness to particle loss.

In Chapter 8 we turn our attention solely to ways to improve the precision of lossy interferometry. In particular, we focus on the recent work of references [1, 2] which determined a theoretical optimum initial state for two-mode lossy interferometry, i.e. a state that is both precise and robust. We propose an experimentally accessible scheme that can measure general phase shifts with precisions close to that of this theoretical optimum initial state. Motivated by the results of the Chapter 7, we also begin to look at the potentials of multimode interferometry for making precise and robust phase measurements. This is still a work in progress but nevertheless we demonstrate one way multimode interferometers can be made to increase the precision of phase measurements in lossy environments. We expect to find other advantages of these multimode devices as this work progresses. The results presented in this chapter form the basis of a paper recently submitted to New Journal of Physics.

Concluding remarks are given in Chapter 9 along with other ideas for future work.

Chapter 2

Bose-Einstein condensates

In 1995 a new state of matter was produced by cooling a gas of weakly interacting bosons to a temperature close to absolute zero. At such cold temperatures a large fraction of the particles in the gas occupy the same quantum state, thereby producing a macroscopic quantum object called a Bose-Einstein condensate. Bose-Einstein condensates have uses in many different branches of physics, not least in the quantum world where it is hoped they will prove useful in the creation of macroscopic quantum superpositions, precision measurements and quantum information processing.

In this thesis we shall focus on their potential for making ultra-precise measurements, in particular rotation rate measurements. We introduce the theory of Bose-Einstein condensates necessary to understand how they can be used to achieve this in this chapter. We begin by giving an overview of the steps leading up to the first experimental demonstration of a Bose-Einstein condensate in a weakly interacting gas. We then introduce the theory of these condensates in ideal gases, briefly discuss the methods used to create them, introduce the Bose-Hubbard model which is used to describe the motion of bosons in an optical lattice and finally consider the effects of rotations of the optical lattice on the condensate.

2.1 History

The theory of Bose-Einstein condensates (BEC) began in 1924 when Bose introduced a new statistical description of photons [18]. Instead of treating these massless bosons as distinguishable particles he found that by treating them as identical particles, and thereby introducing identical particle statistics, he was able to derive Planck's law of radiation. The following year Einstein extended this statistical description of identical particles to gases of non-interacting massive bosons [19]. He showed that, below a certain temperature, a large fraction of the particles in the gas would occupy the lowest-energy single particle state. The resulting state of matter is known as a BEC after its two discoverers.

The next major step in the field of BECs came in 1937 when it was shown that cooling ^{4}He to below 2.17K results in a new type of fluid, called a superfluid [20, 21]. It was shown shortly after that the properties of this superfluid were due to partial Bose-Einstein condensation of the helium [22, 23]. However, the large interactions that exist between helium atoms meant there were difficulties describing the superfluid using BEC theory. As a result research began to focus on ways to produce BECs in weakly interacting gases.

The first suggested candidate was spin-polarised hydrogen. However, initial experimental attempts to form an atomic hydrogen condensate proved unsuccessful due to problems associated with cooling the gas. It was not until 1998, three years after the first experimental demonstration of a BEC in a weakly interacting gas, that Bose-Einstein condensation of atomic hydrogen was achieved [24]. Nevertheless it was cooling techniques developed during these early attempts that ultimately allowed for the first creation of a BEC in a weakly interacting gas in 1995 at JILA [25]. Here Eric Cornell and Carl Wieman created a BEC of approximately 2000 ^{87}Rb atoms at a temperature near 170nK. This was shortly followed by the creation of sodium condensate at MIT [26] by Wolfgang Ketterle and a lithium condensate at Rice University [27]. Following the success of their experiments Cornell, Wieman and Ketterle were all awarded the 2001 Nobel Prize in Physics.

2.2 Bose-Einstein condensation in an ideal gas

In this section we introduce the theory of an ideal, non-interacting Bose gas. In reality of course some small interactions will always exist between the particles, however this mathematical model is both elegant and useful for the realisation of a BEC.

In 1924 Bose discovered that quantum particles do not obey the laws of classical statistics. He realised that instead of acting as individual, distinguishable particles they act as identical, indistinguishable particles. This means that exchanging two quantum particles in a many body system must leave all the observables of that system unchanged. Consequently, the only possible change to the system's wavefunction after the exchange of two particles is the introduction of a global phase factor. However, since reversing the exchange must return the original wavefunction, the global phase factor is limited to +1 or -1. Particles for which the phase factor is +1 are called bosons and those for which the phase factor is -1 are called fermions. The wavefunction of a boson is symmetric whilst that of a fermion is anti-symmetric which means that fermions cannot occupy the same quantum state whilst bosons can. In fact, it is the accumulation of many bosons in the same single particle state that leads to the formation of a BEC and we will now show what conditions are required to achieve this.

It is well known that for a non-interacting Bose gas in thermal equilibrium the expected number of particles in any particular energy state i is given by

$$N(\epsilon_i, T) = \frac{1}{e^{(\epsilon_i - \mu)/k_B T} - 1} \tag{2.1}$$

where ϵ_i is the energy of state i, k_B the Boltzmann constant, T the temperature of the gas and μ the chemical potential which physically corresponds to the amount of energy required to add a particle to the system whilst keeping the entropy and volume fixed. From this equation we can see that μ must be less than ϵ_0 to prevent negative values of $N(\epsilon_0, T)$ which are clearly unphysical. Here we set $\epsilon_0 = 0$ meaning

the chemical potential must always be negative. We determine μ by the condition that the total number of particles is equal to the sum of the occupancies of each of the individual levels

$$N = \sum_{\epsilon_i} \frac{1}{e^{(\epsilon_i - \mu)/k_B T} - 1}. \tag{2.2}$$

Replacing the sum in equation 2.2 with an integral is commonplace in thermodynamic calculations involving gases since, for systems with large volumes, the spacing between energy levels is small and the distribution varies slowly between these levels. However, for the ground state this approximation fails so we treat it separately from the integral. This gives,

$$N = N_0 + \int d\epsilon D(\epsilon) N(\epsilon_i, T) \tag{2.3}$$

where $N_0 = 1/(e^{-\mu/k_B T} - 1)$ is the number of particles in the ground state and $D(\epsilon)$ is the density of states which for free particles in three dimensions is

$$D(\epsilon) = \frac{V}{4\pi^2} \left(\frac{2m}{\hbar^2} \right)^{3/2} \epsilon^{1/2}. \tag{2.4}$$

Evaluation of the above integral gives the number of particles in all the excited states N_{ex}.

The population of each energy level increases with μ and T and therefore, so as to keep the total number of particles in the system constant, any decrease in temperature must be accompanied by an increase in μ. However, since μ must always be negative its largest possible value is 0 which means the maximum number of particles that can be in the excited states is

$$N_{\text{ex}}^{\max} = V\zeta(3/2) \left(\frac{m k_B T}{2\pi\hbar^2} \right)^{3/2} \tag{2.5}$$

where $\zeta(3/2) \approx 2.612$. The critical temperature, T_c, is found by setting $N_{\text{ex}}^{\max} = N$. This gives

$$T_c = \frac{2\pi\hbar^2}{m k_B} \left(\frac{N}{\zeta(3/2) V} \right)^{2/3}. \tag{2.6}$$

Below this temperature the atoms have no choice but to populate the ground state leading to a macroscopic build up of atoms in this mode, the condensate mode. Using equations 2.5 and 2.6 we can see that, for $T < T_c$, the proportion of atoms in the condensate is given by

$$\frac{N_0}{N} = 1 - \left(\frac{T}{T_c}\right)^{3/2} \tag{2.7}$$

and that at $T = 0$ all N atoms are in the ground state.

This relation is most often expressed in terms of the length scales of the system, namely the inter-particle spacing, $(N/V)^{1/3}$, and the thermal de Broglie wavelength which is defined as

$$\lambda_{dB} = \left(\frac{2\pi\hbar^2}{mk_BT}\right)^{1/2}. \tag{2.8}$$

Substituting this into equation 2.6 we can rewrite $T < T_c$ as,

$$\lambda_{dB}^3 \frac{N}{V} > 2.612 \tag{2.9}$$

which shows that BECs form when λ_{dB} of the atoms is similar to their separation. This is equivalent to the commonly quoted criteria that the wavefunctions of the atoms must overlap. In experiments the densities tend to range from $10^{13}-10^{15}\text{cm}^{-3}$ which corresponds to transition temperatures of order 100nK. In the next section we discuss ways to cool atoms to these extremely low temperatures but first we note the results presented above are for a homogenous condensate. However, experimentally it most likely that the condensate will be trapped in an approximate harmonic potential and so will have a non-uniform density. In this case equation 2.6 becomes,

$$T_c = \frac{\hbar\omega_T}{mk_B}\left(\frac{N}{\zeta(3)}\right) \tag{2.10}$$

where ω_T is the angular frequency of the trap and $\zeta(3) \approx 1.202$ and for $T < T_c$ the proportion of atoms in the condensate is,

$$\frac{N_0}{N} = 1 - \left(\frac{T}{T_c}\right)^3. \tag{2.11}$$

2.3 Creating a Bose-Einstein condensate

As previously discussed, extremely low temperatures are required to produce a BEC in a weakly interacting bose gas. For many years experimental realisation of these temperatures eluded experimentalists. It was not until 1995, 70 years after Einstein first developed his theory, that cooling techniques advanced enough to achieve Bose-Einstein condensation. The first successful experiments cooled atoms using a combination of laser cooling and evaporative cooling which we briefly describe here. For a good review see [28].

2.3.1 Laser cooling

The atoms are initially cooled by using light beams to reduce their thermal motion. This process is known as laser cooling and its origin can be traced back to 1933 when Frisch deflected a beam of sodium atoms using resonance radiation from a lamp [29]. However, the intensity of the lamp was too low to manipulate the atoms in a useful way. It was not until the advent of the laser that the ability to control the thermal motion of atoms with light proved experimentally feasible. Between 1970 and 1975 a number of schemes were proposed to slow atoms with laser beams [30, 31]. These schemes relied on the well known fact that when a photon is absorbed by an atom there is a momentum transfer in a particular direction. A photon is then emitted in a random direction which also transfers momentum but over many cycles this particular momentum transfer will average to zero. So by bombarding an atom with a laser beam that opposes its motion its velocity is reduced. Since atoms in a gas move in all directions three orthogonal pairs of counter-propagating laser beams that are red-detuned from atomic resonance are typically used to slow the atoms. Due to the Doppler effect each atom is most likely to absorb a photon from a laser that opposes its motion. So, regardless of its initial direction each atom feels a force that acts to slow it down. This was first demonstrated in 1985 when a cloud of 10^5 sodium atoms were cooled to about 240μK [32].

Laser cooling comes to a halt when, because their velocities have changed, the

atoms are no longer in resonance with the laser. Nevertheless this problem can be overcome by tuning the atomic transition frequency using magnetic fields in a process known as Zeeman slowing. Here a magnetic field is created using a solenoid whose diameter gradually decreases along the atom's path thus leading to an increase in magnetic field strength. The variation in field strength enables the atom to remain on resonance with the laser for longer and consequently colder temperatures are achieved when the Zeeman slowing technique is employed.

2.3.2 Evaporative cooling

The temperatures achieved by laser cooling are extremely low, typically of the order of a few micokelvin, however they are not cooled enough to achieve Bose-Einstein condensation in gases. To reach the required nanokelvin temperatures an additional cooling technique must be performed. The technique that proved most successful is called evaporative cooling and was first developed in the context of a gas in a trap by Hess in 1986 [33]. It relies on the fact that if particles escaping from a system have more energy than the average energy of particles in the system, the remaining particles will rethermalise at a lower temperature.

In order to employ this technique the gas is trapped in a magnetic field at the end of the laser cooling period. A 'hole', from which atoms can escape, is then made high up the side of the trap. In order for an atom to escape its energy must be at least equal to the energy of the trap at the hole ensuring only the most energetic atoms escape. After the loss of these high energy atoms the remaining ones undergo elastic collisions and the temperature of the gas is therefore decreased. By gradually lowering the hole the temperature is reduced further still.

It was the combination of these two cooling techniques that ultimately lead to the formation of the first BEC in 1995. Since then the techniques have been employed in numerous experiments to produce condensates of many different atomic species.

2.4 The Bose-Hubbard model

Since the first realisation of a BEC in a dilute weakly interacting gas there has been much talk of their potential uses in fields such as quantum information processing, metrology and quantum state engineering. Some of the properties that sparked this interest include the long condensate life times (of the order of several seconds) that have been experimentally observed, the ability to image and move the condensate without immediately destroying it and its strong interaction with laser light. Perhaps the most promising BEC experiments for future applications in these fields are those in which the BEC is loaded into an optical lattice (a periodic array of mircotraps generated by standing wave laser light fields) [1]. The greatest appeal of this set-up is the high degree of control of the condensate that is achieved simply by varying the laser parameters and configurations. Another important feature is, because of the high particle densities associated with the condensate, interactions exist between particles on the same lattice site. These interactions can be controlled and exploited, again, simply by altering the intensity of the laser light. Together these features make BECs in optical lattices ideal candidates for many experimental schemes in quantum information processing and metrology. The focus of this thesis, however, is their potential applications in quantum metrology.

In this section we first discuss how atoms are trapped by laser light in an optical potential, we then show how periodic potentials (optical lattices) are created using counter-propagating lasers, derive the Bose-Hubbard model (BHM) that describes the dynamics of the condensate in the lattice and finally show how this model can be modified to account for rotations of the optical lattice.

2.4.1 Optical potentials

When an atom is subjected to an electric field, such as that of a laser, it acquires an electric dipole moment and its energy levels are shifted. BEC experiments often exploit this shift in energy levels to trap atoms at a particular spatial location. Here

[1] For a good review see [34].

we briefly describe this process in a system where we assume spontaneous emissions can be neglected. This assumption is valid because laser light is usually tuned far away from the atomic resonance frequency.

For simplicity we consider a single two-level atom with Hamiltonian

$$H_A = \hbar\omega_0 |e\rangle\langle e| \tag{2.12}$$

where $|e\rangle$ denotes the excited state which has energy $\hbar\omega_0$ and the ground, $|g\rangle$, has zero energy. The atom is subjected to the electric field of a laser of the form, $\mathbf{E}(\mathbf{x},t) = E_0(\mathbf{x})e^{-i\omega_L t} + E_0^*(\mathbf{x})e^{i\omega_L t}$ where ω_L is the angular frequency of the laser and $E_0(\mathbf{x})$ is the amplitude of the field at position $\mathbf{x}$. The action of the laser on the atom produces a dipole in the atom of the form $\mathbf{d} = \mathbf{d}_{eg}|e\rangle\langle g| + \mathbf{d}_{eg}^*|g\rangle\langle e|$ where $\mathbf{d}_{eg} = \langle e|\mathbf{d}|g\rangle$. Using the dipole approximation, which assumes the electric field varies slowly compared to the size of the atom, the interaction between the atom and the laser is described by

$$H_{\mathrm{I}} = -\mathbf{d}\cdot\mathbf{E} = -\left(\mathbf{d}_{eg}|e\rangle\langle g| + \mathbf{d}_{eg}^*|g\rangle\langle e|\right)(E_0(\mathbf{x})e^{-i\omega_L t} + E_0^*(\mathbf{x})e^{i\omega_L t}\right). \tag{2.13}$$

At this point we use the rotating wave approximation to simplify the above equation. In the rotating wave approximation high frequency terms are ignored since, on any considerable time scale, the interactions of these quickly oscillating terms will soon average to zero. This is valid here because $\delta = \omega_L - \omega_0 \ll \omega_L + \omega_0$. Applying this approximation gives

$$H_{\mathrm{I}} = \frac{\hbar}{2}\Omega e^{-i\omega_L t}|e\rangle\langle g| + \frac{\hbar}{2}\Omega^* e^{i\omega_L t}|g\rangle\langle e| \tag{2.14}$$

where $\Omega = -2\mathbf{d}_{eg}E_0(\mathbf{x})/\hbar$ is the Rabi frequency which drives transitions between the ground and excited state.

If $|\delta| \gg \Omega$ the interaction between the light and the atom is weak and as such the shift in atomic energy levels can be calculated using second order perturbation

theory,

$$\Delta E_{g,e} = \pm \frac{|\langle g|H_I|e\rangle|^2}{\hbar\delta} = \pm\hbar\frac{|\Omega|^2}{4\delta} \tag{2.15}$$

where the sign refers to the ground and excited states respectively. This shift in the energy levels can be regarded as an effective potential, V_{dip}, felt by the atom which acts to trap it since $\mathbf{F}(\mathbf{x}) = -\nabla V_{\text{dip}}(\mathbf{x})$.

Crucial to the form of the potential is the sign of the detuning as when $\delta > 0$ (blue detuning) the atoms will feel a repulsive force and so will move towards regions of low field strength, whilst when $\delta < 0$ (red detuning) the atoms will feel an attractive force and so will be attracted to regions of high field strength.

2.4.2 Optical lattices

An optical lattice is a periodic arrangement of the above optical potentials (see reference [35] for a nice review). They are most easily created by superimposing two counter-propagating laser beams with electric fields of the form $E(\mathbf{x}, t) = E_0 e^{ikx}$ and $E(\mathbf{x}, t) = E_0 e^{-ikx}$ where E_0 is the field amplitude and $k = 2\pi/\lambda$ is the wave number of the laser light. The interference between the two laser beams results in an optical standing wave with period $\lambda/2$. The resulting potential has the form $V(\mathbf{x}) = V_0 \cos^2(kx)$ where V_0 is the lattice potential depth which is most often given in units of recoil energy $E_R = \hbar^2 k^2/(2m)$ where m is the mass of an atom. This set-up is easily extended to three dimensions by introducing two further pairs of counter-propagating laser beams placed orthogonal to both one another and the first laser pair. This results in a trapping potential of the form $V(\mathbf{x}) = V_{0,x}\cos^2(kx) + V_{0,y}\cos^2(ky) + V_{0,z}\cos^2(kz)$.

These optical lattices can be easily controlled by the experimenter. The depth of the potential, for example, can be dynamically altered during an experiment simply by changing the intensity of the trapping light. In fact the depth in each dimension can be controlled individually by tuning the intensity of the corresponding pair of lasers. By increasing the intensity of the trapping light in a particular dimension the energy levels in that dimension become so widely spaced that the atoms are

restricted to the lowest energy level. Motion in this dimension is therefore frozen resulting in an effectively two dimensional system. Similarly increasing the laser intensity in two spatial dimensions, so that it is significantly larger than in the third dimension, particle movement can be made to occur in just one dimension.

It is also possible to create a variety of trapping geometries simply by changing the laser configurations. Central to this thesis will be developing ways to precisely measure rotations with BECs. This is most easily achieved using the traditional ring geometry and as such we require an optical ring lattice. These ring lattice potentials have already been experimentally demonstrated [36, 37].

2.4.3 Single particle system

So far we have shown how atoms can be trapped in an optical lattice using the dipole force. We now wish to demonstrate how these atoms can propagate through the lattice. The basic physics of the system is very similar to that of an electron moving through a solid and as such the mathematical techniques used will be similar. For simplicity we consider a single particle moving in a one dimensional lattice potential with period $\mathbf{X}$ which implies $V(\mathbf{x}) = V(\mathbf{x} + \mathbf{X})$.

The single particle wavefunction, $\Psi(\mathbf{x})$, of a particle in a one dimensional potential obeys the following Schrödinger equation

$$\left[\frac{-\hbar^2}{2m}\nabla^2 + V(\mathbf{x})\right]\Psi(\mathbf{x}) = E\Psi(\mathbf{x}) \tag{2.16}$$

where m is the mass of the particle. It is well known, from solid state physics, that the solution to this equation is given by the Bloch function

$$\Psi(\mathbf{x})_q^{(n)} = e^{iq\mathbf{x}}u_q^{(n)}(\mathbf{x}) \tag{2.17}$$

where $u_q^{(n)}(\mathbf{x})$ has the same period as the lattice meaning $u_q^{(n)}(\mathbf{x}) = u_q^{(n)}(\mathbf{x}+\mathbf{X})$, $e^{iq\mathbf{x}}$ is a plane wavefunction and n is the band index. The parameter q plays a similar

role to momentum in free space and for this reason it is called quasi-momentum [2]. It is confined to the first Brillouin zone, $-\pi/X < q \leq \pi/X$.

As the potential depth increases the wavefunction becomes more localised on each lattice site and it becomes convenient to use Wannier functions to describe the trapped particles. In this set-up Wannier functions prove particularly useful as they allow a mean position to be attributed to the particles and allow interactions between particles on the same lattice site to be easily accounted for. Wannier functions are unitary transformations of Bloch functions and are given by

$$w^{(n)}(x - x_j) = \frac{1}{\sqrt{S}} \sum_q e^{-iqx_j} \Psi_q^{(n)}(x) \tag{2.18}$$

where x_j is the position of the jth particle, S is the number of lattice sites and the sum is over the first Brillouin zone. This is the wavefunction of a single particle in a periodic optical lattice when the barriers are high enough to consider the atoms as well localised particles.

2.4.4 Derivation of the Bose-Hubbard Model

The BHM for a weakly interacting Bose gas was first suggested by Jaksch *et al.* in 1998 [13]. It describes the dynamics of interacting BEC atoms in an optical lattice. Starting from the full many body Hamiltonian we follow reference [38] to give a naïve derivation of the Bose-Hubbard Hamiltonian.

The Hamiltonian of a weakly interacting Bose gas in an optical lattice is

$$H_{\mathrm{MB}} = \int d^3x \hat{\Psi}^\dagger(\mathbf{x}) \left(\frac{-\hbar^2}{2m} \nabla^2 + V(\mathbf{x}) \right) \hat{\Psi}(\mathbf{x}) + \frac{g}{2} \int d^3x \hat{\Psi}^\dagger(\mathbf{x}) \hat{\Psi}^\dagger(\mathbf{x}) \hat{\Psi}(\mathbf{x}) \hat{\Psi}(\mathbf{x}) \tag{2.19}$$

where $\hat{\Psi}(\mathbf{x})$ and $\hat{\Psi}^\dagger(\mathbf{x})$ are the bosonic field operators for atoms in a given internal state that annihilate and create an atom at position $\mathbf{x}$ respectively. They obey the

[2] Although strictly speaking the quasi-momentum is $\hbar q$.

commutation relations,

$$[\hat{\Psi}(\mathbf{x}'), \hat{\Psi}(\mathbf{x})] = [\hat{\Psi}^\dagger(\mathbf{x}'), \hat{\Psi}^\dagger(\mathbf{x})] = 0 \tag{2.20}$$

$$[\hat{\Psi}^\dagger(\mathbf{x}'), \hat{\Psi}(\mathbf{x})] = \delta(\mathbf{x}' - \mathbf{x}). \tag{2.21}$$

and are normalised so that

$$\left\langle \int d^3x \hat{\Psi}^\dagger(\mathbf{x})\hat{\Psi}(\mathbf{x}) \right\rangle = N. \tag{2.22}$$

The parameter $V(\mathbf{x})$ is the optical lattice potential and g is the interaction strength between two atoms. If the atoms only interact via s-wave scattering $g = 4\pi a_s \hbar^2/m$ where a_s is the s-wave scattering length. We assume that the system is cold enough to consider only the lowest band of the optical lattice and the barriers are high enough to expand the field operators in terms of Wannier functions, $\hat{\Psi}(\mathbf{x}) = \sum_j a_j w^{(0)}(\mathbf{x} - \mathbf{x_j})$ where a_j ($a_j^\dagger$) is the annihilation (creation) operator for an atom at site $\mathbf{x}_j$. These operators obey the following commutation relations

$$[a_j, a_k] = [a_j^\dagger, a_k^\dagger] = 0 \tag{2.23}$$

and

$$[a_j, a_k^\dagger] = \delta_{j,k}. \tag{2.24}$$

Substituting the Wannier functions into equation 2.19 and only considering one dimension gives

$$H_{\mathrm{MB}} = -\sum_{j,k} J_{jk} a_j^\dagger a_k + \frac{1}{2} \sum_{j,k,l,m} U_{jklm} a_j^\dagger a_k^\dagger a_l a_m \tag{2.25}$$

where

$$J_{jk} = -\int dx w^{(0)}(\mathbf{x} - \mathbf{x}_j) \left(\frac{p^2}{2m} + V(\mathbf{x}) \right) w^{(0)}(\mathbf{x} - \mathbf{x}_k), \tag{2.26}$$

and

$$U_{jklm} = g \int dx w^{(0)}(\mathbf{x} - \mathbf{x}_j) w^{(0)}(\mathbf{x} - \mathbf{x}_k) w^{(0)}(\mathbf{x} - \mathbf{x}_l) w^{(0)}(\mathbf{x} - \mathbf{x}_m). \tag{2.27}$$

The J_{jk} term describes the tunnelling between lattice sites whilst U_{jklm} gives the inter-particle interactions. Tunnelling between sites other than nearest neighbours and the off-site interactions are small compared to tunnelling between nearest neighbours and onsite interactions meaning the only terms we need to consider are $U_{jjjj} = U$ and $J_{j,j+1} = J$. Using these approximations gives the Bose-Hubbard Hamiltonian

$$H_{\mathrm{BH}} = -J \sum_{j=0}^{S-1} \left(a_j^\dagger a_{j+1} + a_{j+1}^\dagger a_j \right) + \frac{U}{2} \sum_{j=0}^{S-1} a_j^\dagger a_j^\dagger a_j a_j. \tag{2.28}$$

In the literature this Hamiltonian often contains an extra term of the form $\sum_j \epsilon_j a_j^\dagger a_j$. This term arises due to the presence of an additional trapping potential, $V_T(\mathbf{x})$, which varies slowly compared to $V(\mathbf{x})$. It is created using an additional two lasers propagating at small angles θ_ϵ and $\pi - \theta_\epsilon$ with respect to the x-axis and results in an energy offset ϵ_j of lattice site $\mathbf{x}_j$. The Bose-Hubbard Hamiltonian is therefore, more completely,

$$H_{\mathrm{BH}} = -J \sum_{j=0}^{S-1} \left(a_j^\dagger a_{j+1} + a_{j+1}^\dagger a_j \right) + \frac{U}{2} \sum_{j=0}^{S-1} a_j^\dagger a_j^\dagger a_j a_j + \sum_{j=0}^{S-1} \epsilon_j a_j^\dagger a_j \tag{2.29}$$

however throughout the thesis we take all $\epsilon_j = 0$ unless otherwise stated. We now describe each of the terms in the Hamiltonian in more detail, discussing how they each effect the system dynamics.

Tunnelling strength, J

The parameter J describes the amount of tunnelling between adjacent lattice sites. When $J \gg U$ the wavefunction is delocalised over the whole system and the BEC forms a superfluid $|\psi_{\mathrm{sf}}\rangle \propto (\sum_j a_j^\dagger)^N |\mathrm{vac}\rangle$.

Onsite interaction, U

The onsite interaction strength is given by the U term in H_{BH} and is divided by two to account for double counting of the two particle interactions. Note $\sum_j a_j^\dagger a_j^\dagger a_j a_j = \sum_j n_j(n_j - 1)$ which shows that, as usual, the two particle interaction energy increases with the square of the particle density and the -1 term ensures that a single particle does not gain any interaction energy. When $U \gg J$ a quantum phase transition takes place and the system becomes a Mott insulator. In this regime the atoms become localised to single lattice sites and for commensurate filling of one particle per lattice site $|\psi_{\mathrm{MI}}\rangle \propto \prod_j a_j^\dagger |\mathrm{vac}\rangle$.

The ratio U/J is directly related to the depth of the lattice sites, which is in turn controlled by the laser intensities. As the depth of the lattice potentials are adiabatically increased the atomic wavefunction becomes increasingly localised. This leads to a decrease in the tunnelling strength and an increase in the onsite interaction.

Energy off-set, ϵ

For most of the work in this thesis all $\epsilon_j = 0$ which is simply achieved by not introducing the additional potential $V_T(\mathbf{x})$. However, in Chapter 6 an energy off-set will be applied to one lattice site. This is achieved using an additional pair of lasers as briefly described earlier.

2.5 Rotating the system

A considerable portion of this thesis will be devoted to schemes designed to measure rotation rates. These schemes follow the traditional Sagnac geometry where a single beam of particles is split into two beams which are then made to flow in opposite directions around a ring [14] [3]. These two beams are later recombined and an interference pattern is observed. If the ring is allowed to rotate at some angular velocity ω the resulting interference pattern is shifted and the size of this shift is

[3] Sagnac gyroscopes are discussed in more detail in Chapter 4.

directly proportional to the angular velocity of the ring. Therefore, by measuring the shift of the interference pattern ω can be determined.

2.5.1 Flow states

In order to implement such a rotation measurement using a BEC we first require our BEC to be in a ring potential. We use an optical ring lattice which is simply a set of S lattice sites that form a ring geometry. These lattice rings have already been experimentally demonstrated [36, 37] for different numbers of sites. Loading a BEC into such a ring results in a system that is described by the one dimensional BHM. This can be seen from figure 2.1 which shows a ring of three lattice sites. The system can be effectively described by the single variable $x = R\varphi$ where site 0 is at $x = 0$, $0 \leq \varphi < 2\pi$ and R is the radius of the ring which is fixed. Using x as the system variable it is easy to show that the 1D Bose-Hubbard Hamiltonian previously derived can be used to describe a BEC in a ring of lattice sites. [4]

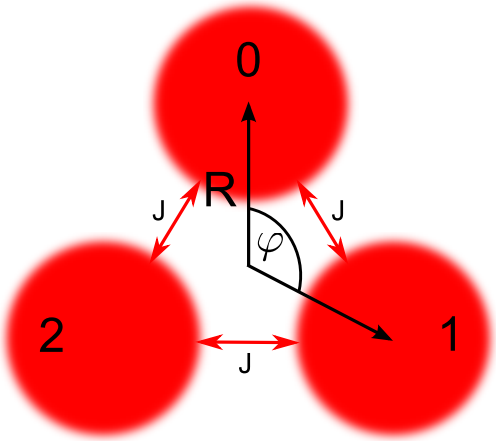

Figure 2.1: An optical ring lattice of three sites. The tunnelling between adjacent sites is shown by the red arrows. The strength of this tunnelling is J. Every point around the ring is uniquely defined by $x = R\varphi$ where R is the radius of ring and $0 \leq \varphi < 2\pi$.

The second requirement to implement a Sagnac measurement is the ability to split our BEC so we have atoms flowing in opposite directions around the ring. We propose a scheme to do this in Chapter 6 however, we must first introduce the flow

[4] For a ring of S sites $a_j = a_{j+S}$ due to the ring geometry.

basis. This will allow us to represent the state of the system in terms of the angular momentum of the atoms rather than their position. First we must highlight some important points about this set-up.

The wavefunction of a BEC is given by $\psi(x) = \psi_0 e^{i\Phi(x)}$, where ψ_0 is the density of the condensate which is taken to be the same for all x and $\Phi(x)$ is the phase of the condensate. Due to the requirement that the wavefunction at every point in space must be uniquely defined the phase around the ring must always be an integer multiple of 2π. This condition is known as the phase matching condition and assuming that the phase varies linearly around the ring we can therefore write $\psi(x) = \psi_0 e^{i2\pi nx/L}$ where $L = 2\pi R$ is the circumference of the ring and n is an integer. Applying the velocity operator, $-i(\hbar/m)\nabla$, to this wavefunction gives $v = \hbar 2\pi n/(mL)$. From this we see that the phase matching condition leads to the quantisation of velocity, and hence angular momentum and flow, of the atoms in the ring.

The ability to describe a system consisting of a BEC in a ring lattice potential in terms of its angular momentum, or flow, rather than in terms of the number of atoms on a particular site will prove extremely valuable later in the thesis. The transformation from the site basis to the flow basis is easily achieved using the discrete Fourier transform

$$\alpha_k = \frac{1}{\sqrt{S}} \sum_{j=0}^{S-1} a_j \exp\left(i\frac{2\pi jk}{S}\right) \tag{2.30}$$

where α_k ($\alpha_k^\dagger$) annihilates (creates) a particle with angular momentum $k\hbar$, or equivalently, a particle with k quanta of flow. These operators obey the commutation relations

$$[\alpha_k, \alpha_l] = [\alpha_k^\dagger, \alpha_l^\dagger] = 0 \tag{2.31}$$

and

$$[\alpha_k, \alpha_l^\dagger] = \delta_{k,l}. \tag{2.32}$$

The number of different flow states allowed around a ring is equal to the number

of sites that ring contains. For example, for a ring with three sites there are three allowed flow states,

$$\begin{aligned} \alpha_0 &= (a_0 + a_1 + a_2)/\sqrt{3} \\ \alpha_1 &= (a_0 + e^{i2\pi/3}a_1 + e^{i4\pi/3}a_2)/\sqrt{3} \\ \alpha_2 &= (a_0 + e^{-i2\pi/3}a_1 + e^{-i4\pi/3}a_2)/\sqrt{3}. \end{aligned} \tag{2.33}$$

The restriction to three flow states can be clearly seen by inputting other values of k into equation 2.30 as any other value will result in a flow state equivalent to one of the three given above. For example when $k = -1$ we find $\alpha_{-1} = (a_0 + e^{-i2\pi/3}a_1 + e^{-i4\pi/3}a_2)/\sqrt{3} = \alpha_2$.

The angular momentum, L_m, of each of these flow states is found by considering the wavefunction of the BEC, $\psi(x) = \psi_0 e^{i2\pi nx/L}$. The integer n corresponds to the particular flow state the system is in, that is $k = n$. So, for example, for a system with $k = 1$ the total phase around the ring is 2π whilst for a system with $k = 0$ the total phase is 0 and for $k = -1$ the total phase is -2π. The angular momentum of a system with k quanta of flow is,

$$\begin{aligned} L_m &= \langle \psi(x) | R\mathbf{p} | \psi(x) \rangle = -i\hbar \int_0^L \psi^*(x) \nabla \psi(x) dx \\ &= \hbar k \end{aligned} \tag{2.34}$$

where $\mathbf{p}$ is the momentum operator.

The Hamiltonian, H_{BH} (see equation 2.28), can be rewritten in the flow basis with its exact form depending on how many sites the ring contains. For a ring with three sites H_{BH} becomes

$$\begin{aligned} H_{\mathrm{BH}} &= -J(2\alpha_0^\dagger\alpha_0 - \alpha_1^\dagger\alpha_1 - \alpha_2^\dagger\alpha_2) + \frac{U}{6}((\alpha_0^\dagger)^2(\alpha_0)^2 + (\alpha_1^\dagger)^2(\alpha_1)^2 + (\alpha_2^\dagger)^2(\alpha_2)^2 \\ &+ 4(\alpha_0^\dagger\alpha_0\alpha_1^\dagger\alpha_1 + \alpha_0^\dagger\alpha_0\alpha_2^\dagger\alpha_2 + \alpha_1^\dagger\alpha_1\alpha_2^\dagger\alpha_2) + 2((\alpha_0)^2\alpha_1^\dagger\alpha_2^\dagger \\ &+ (\alpha_1)^2\alpha_0^\dagger\alpha_2^\dagger + (\alpha_2)^2\alpha_0^\dagger\alpha_1^\dagger + \mathrm{h.c.})) \end{aligned} \tag{2.35}$$

in the flow basis. Immediately we see that in this basis the J terms are diagonal and that the interactions couple states with different flows.

2.5.2 Rotations

To measure a rotation rate we let the ring of lattice sites move under the influence of that rotation, ω, thereby changing the angular velocity of the ring from zero to ω. In the laboratory frame the flow states described above remain unchanged and the phase matching condition is always satisfied. In the frame of the rotating ring, however, the α_k are altered. The α_0 flow state for example, no longer appears to be stationary. In this rotating frame α_k is

$$\alpha_{kRot} = \frac{1}{\sqrt{S}} \sum_{j=0}^{S-1} e^{i2\pi jk/S - i\theta j/S} a_j \tag{2.36}$$

meaning

$$a_{jRot} = \frac{1}{\sqrt{S}} \sum_{k=0}^{S-1} e^{-i2\pi jk/S + i\theta j/S} \alpha_k \tag{2.37}$$

where θ is a phase established around the ring due to the rotation ω. To understand the origin of θ consider the wavefunction of a condensate at point X_L in the laboratory, $\psi(X_L(0)) = \psi_0 e^{i\Phi(X_L)}$. Initially point X_L corresponds to point $X_R(0)$ on the ring and $\psi(X_L(0)) = \psi(X_R(0))$. If the condensate flows around the ring after some time, t, it will return to its original position in the laboratory i.e. point X_L. Due to the phase matching condition we know $\psi(X_L(t)) = \psi(X_L(0))$. However, if the ring is left rotate during this time, by the time the condensate returns to its original position in the laboratory this will no longer coincide with its original position on the ring. This means $\psi(X_R(t)) = \psi_0 e^{i\Phi(X_L) + i\theta(X_L - X_R(t))/L}$ (assuming the ring moves at a constant angular velocity). Note that θ does not have to satisfy the phase matching condition as it refers to the phase of the ring, not the condensate. Recognising that, for a general X_L, the effect of ω is to alter the wavefunction of the BEC by an amount $\psi_0 e^{i\theta x/L}$ a relationship between θ and ω can be determined

as follows,

$$\begin{aligned} \omega &= \left\langle \psi(x) \left| \frac{\mathbf{p}}{mR} \right| \psi(x) \right\rangle = -i\frac{\hbar}{mR} \int \psi^*(x) \nabla \psi(x) dx \\ &= \frac{\hbar\theta}{mLR} = \frac{h\theta}{mL^2}. \end{aligned} \tag{2.38}$$

From equation 2.37 we can see that in the rotating frame of reference the Bose-Hubbard Hamiltonian becomes [39]

$$H_{\mathrm{BH}\theta} = -J \sum_{j=0}^{S-1} \left(a_j^\dagger a_{j+1} e^{i\theta/S} + a_{j+1}^\dagger a_j e^{-i\theta/S} \right) + \frac{U}{2} \sum_{j=0}^{S-1} a_j^\dagger a_j^\dagger a_j a_j. \tag{2.39}$$

Note the rotation has no effect on the interaction term since interactions only depend on the number of atoms on a particular site.

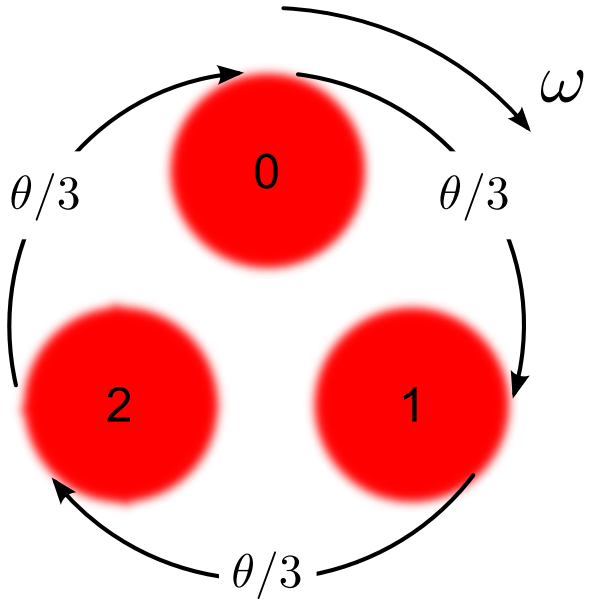

Figure 2.2: Applying a rotation ω to the lattice ring induces a phase θ around the ring. If the phase is linearly varying the phase difference between the three sites above is $\theta/3$.

As in the previous subsection it is possible, and often convenient, to convert $H_{\mathrm{BH}\theta}$ into the flow basis. Again, the exact form of the resulting Hamiltonian depends on the number of lattice sites in the ring. Here we give the Hamiltonian for a ring of

three sites,

$$\begin{aligned} H_{\mathrm{BH}\theta} &= -2J\left(\alpha_0^\dagger\alpha_0\cos\left(\frac{\theta}{3}\right)+\alpha_1^\dagger\alpha_1\cos\left(\frac{\theta-2\pi}{3}\right)+\alpha_2^\dagger\alpha_2\cos\left(\frac{\theta+2\pi}{3}\right)\right) \\ &+ \frac{U}{6}((\alpha_0^\dagger)^2(\alpha_0)^2+(\alpha_1^\dagger)^2(\alpha_1)^2+(\alpha_2^\dagger)^2(\alpha_2)^2+4(\alpha_0^\dagger\alpha_0\alpha_1^\dagger\alpha_1 \\ &+ \alpha_0^\dagger\alpha_0\alpha_2^\dagger\alpha_2+\alpha_1^\dagger\alpha_1\alpha_2^\dagger\alpha_2)+2((\alpha_0)^2\alpha_1^\dagger\alpha_2^\dagger+(\alpha_1)^2\alpha_0^\dagger\alpha_2^\dagger \\ &+ (\alpha_2)^2\alpha_0^\dagger\alpha_1^\dagger+\mathrm{h.c.})). \end{aligned} \tag{2.40}$$

This three site example will prove valuable in Chapter 6 where an atomic gyroscope scheme is described. It precisely measures small changes in rotations using an optical ring of three lattice sites into which a BEC has been loaded and is thus fully described by the above Hamiltonian and flow basis. First, however, we introduce the field of quantum metrology during which we describe ways to determine the precision of such a scheme, discuss the precision capabilities of different quantum states and begin to examine the effects of decoherence on our ability to make ultra-precise measurements.

Chapter 3

Interferometry and quantum metrology

Interferometry is the process by which one estimates an initially unknown parameter of a system or detects small changes in a known parameter. The concept is simple: a probe is allowed to interact with the system and is then measured. In a classical interferometer the parameter can be determined, providing the physical mechanism governing the system dynamics is known, by comparing the input and output state of the probe. Importantly these devices allow for extremely precise parameter estimation, especially when states with quantum correlations are employed as the probe. The ability to perform precise measurements is of fundamental importance to all quantitative fields of science as it allows theories to be tested and refined. As such much research has been, and is currently being, done into ways to improve measurement precision. It is the idea of using quantum correlations to improve measurement precision that will form the basis of this chapter. We begin with a review of Mach-Zehnder interferometry, then discuss a method to quantify the precision of measurement schemes, assess the precision capabilities of several different probes, introduce a decoherence model and describe some of the uses of precision measurement schemes in quantum technologies.

3.1 Interferometry

Measurement is a physical process and as such it is governed by the laws of physics. Since the behaviour of small scale systems is determined by the laws of quantum physics this implies that the measurement of these systems, and the precision of these measurements, will ultimately be determined by quantum mechanics. We know, through the Heisenberg uncertainty relation, that in quantum physics it is not possible to simultaneously measure two non-commuting observables such as position and momentum with arbitrary precision. This therefore presents a bound to quantum measurement precision. A second limit to the precision of quantum measurements arises from the measurement scheme itself and the resources employed in that scheme. For example, to measure the position of a particle one could scatter light from it and in this case the precision would be limited by diffraction effects (the measurement scheme) and the wavelength of the light used (the resources employed). To achieve infinite precision would require photons with infinite energy. The unfeasibility of this request highlights this second limit to measurement precision. One measurement scheme that is extremely effective at making precise measurements given a fixed number of resources is the Mach-Zehnder interferometer (MZI).

A typical MZI is shown in figure 3.1. It consists of two beam splitters, which are usually taken to be 50:50 beam splitters, two mirrors and a relative phase shift which is the parameter we wish to measure. The phase shift could correspond to a diverse range of physical quantities from a difference in path length to a variation in field strength.

To begin the interferometry scheme a state is put into the first beam splitter (BS1). For now we consider the input $|\psi_0\rangle = |1,0\rangle_{0,1}$ where the terms in the kets correspond to the number of particles in modes 0 and 1 respectively (other inputs will be considered later in the chapter). An equivalent way to write $|\psi_0\rangle$ is in terms of mode creation and annihilation operators, $|\psi_0\rangle = a_0^\dagger|0,0\rangle_{0,1}$ where $a_m^\dagger$ (a_m) corresponds to the creation (annihilation) of a particle in mode m. The action of

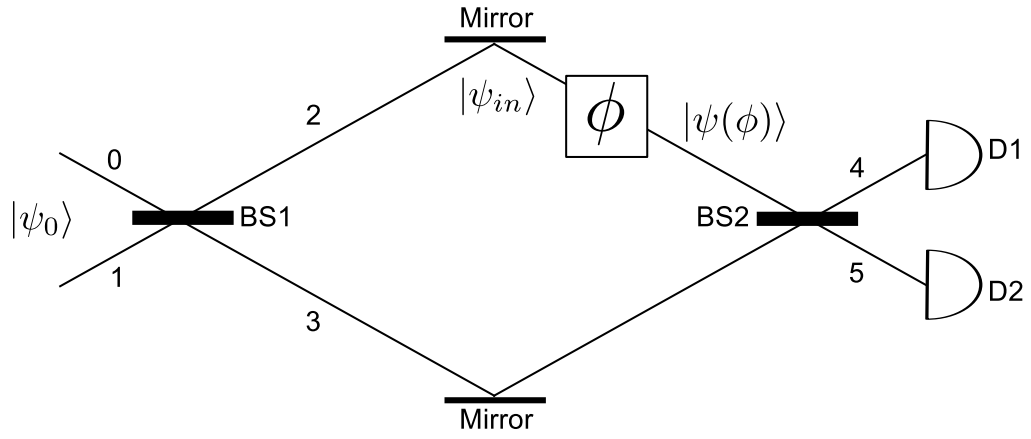

Figure 3.1: A typical Mach-Zehnder interferometer into which $|\psi_0\rangle$ is inputted. BS1 and BS2 are both 50:50 beam splitters, the phase shift ϕ is the quantity to be measured and D1 and D2 are detectors that fire when a particle hits them. The two mirrors are simply there to redirect the output modes of BS1 towards BS2. Their only effect on the state of the system is to introduce an irrelevant global phase factor. Throughout this thesis $|\psi_{in}\rangle$ (the initial state) refers to the state of the system immediately prior to the phase application and $|\psi(\phi)\rangle$ refers to the state of the system immediately after the phase application.

the first 50:50 beam splitter is to transform the mode creation operators as

$$\begin{pmatrix} a_0^\dagger \\ a_1^\dagger \end{pmatrix} \xrightarrow{BS1} \frac{1}{\sqrt{2}} \begin{pmatrix} i & 1 \\ 1 & i \end{pmatrix} \begin{pmatrix} a_2^\dagger \\ a_3^\dagger \end{pmatrix} \tag{3.1}$$

meaning

$$a_0^\dagger |0,0\rangle_{0,1} \xrightarrow{BS1} \frac{1}{\sqrt{2}}(ia_2^\dagger + a_3^\dagger)|0,0\rangle_{2,3} = \frac{1}{\sqrt{2}}(i|1,0\rangle_{2,3} + |0,1\rangle_{2,3}). \tag{3.2}$$

The mirrors then redirect modes 2 and 3 towards a second 50:50 beam splitter (BS2) which results in the state acquiring a global $e^{i\pi/2}$ phase factor which can be ignored. However, before the modes are recombined at BS2 the phase shift that is to be measured is applied through the unitary transformation $U(\phi) = e^{i\phi a_2^\dagger a_2}$ resulting in

$$\frac{1}{\sqrt{2}}(i|1,0\rangle_{2,3} + |0,1\rangle_{2,3}) \xrightarrow{\phi} \frac{1}{\sqrt{2}}(ie^{i\phi}|1,0\rangle_{2,3} + |0,1\rangle_{2,3}). \tag{3.3}$$

The second beam splitter then transforms the creation operators as

$$\begin{pmatrix} a_2^\dagger \\ a_3^\dagger \end{pmatrix} \xrightarrow{BS2} \frac{1}{\sqrt{2}} \begin{pmatrix} i & 1 \\ 1 & i \end{pmatrix} \begin{pmatrix} a_4^\dagger \\ a_5^\dagger \end{pmatrix} \tag{3.4}$$

which results in the output

$$\frac{1}{\sqrt{2}}(ie^{i\phi}|1,0\rangle_{2,3} + |0,1\rangle_{2,3}) \xrightarrow{BS2} \frac{1}{2}[(1-e^{i\phi})|1,0\rangle_{4,5} + i(1+e^{i\phi})|0,1\rangle_{4,5}]. \tag{3.5}$$

Detectors D1 and D2 are placed in modes 4 and 5 respectively and, from (3.5), fire with probability,

$$\begin{aligned} P_{D_1} &= \sin^2(\phi/2) \\ P_{D_2} &= \cos^2(\phi/2) \end{aligned} \tag{3.6}$$

where $P_{D_1}$is the probability D1 fires, that is state $|1,0\rangle_{4,5}$ is detected at the output of BS2, and P_{D_2} is the probability D2 fires which corresponds to a detection of the state $|0,1\rangle_{4,5}$. Altering ϕ results in oscillations of these probabilities.

In order to determine a value for ϕ, this experiment would need to be repeated many times each time recording which detector fired. Using the observed frequency of D1 firing it is possible to estimate a value for P_{D_1}. Then, using the known theoretical probability of this event (see equation 3.6) one can determine an estimate for ϕ. However, due to the unavoidable statistical fluctuations associated with a finite sample the value of ϕ cannot be determined exactly.

These statistical fluctuations can be understood in the context of a simple experiment in which a fair coin is tossed n_R times and the outcome (head or tails) is recorded. Defining $\Delta_c = |n_H - n_T|$ where $n_{H(T)}$ are the number of heads (tails) recorded we intuitively expect the fractional difference in the number of heads and tails recorded, Δ_c/n_R, to decrease with increasing n_R. Repeating the n_R tosses ν times we would therefore expect Δ_c/n_R to vary considerably between runs when n_R is small and less so as n_R increases. The precision of an experiment defines its ability

to reproduce the same result on each run when the conditions remain unchanged and so we see that a large sample is needed to improve precision. If on a single toss of the coin we could somehow measure the outcome as 50% heads and 50% tails we would immediately know P_H and P_T and we could thus say, with no uncertainty, the coin is fair. It is therefore the quantised nature of the outcome that introduces noise into the system.

This simple coin experiment directly relates to a MZI which uses N copies of $|\psi_0\rangle = |1,0\rangle_{0,1}$ to measure ϕ since we determine ϕ by measuring the discrete quantity of a detector firing or not firing. Due to the quantised nature of the outcome we would not expect the observed frequency of D1 firing to reflect the value of P_{D_1} exactly. However, the larger N, the smaller the error in the estimated value of P_{D_1}. This can be shown rigorously using statistical averages. First we define the outcome of the experiment to be $r = 1$ if D1 fires and $r = 0$ if D2 fires. The statistical average outcome of the experiment gives an estimate for P_{D_1} of $\sum_{j=1}^{N} r_j/N$. The error associated with this value of P_{D_1} is [40]

$$\Delta P_{D_1} = \Delta\left(\sum_{j=1}^{N}\frac{r_j}{N}\right) = \frac{\sqrt{\sum_{j=1}^{N}(\Delta r_j)^2}}{N} = \frac{\Delta r}{\sqrt{N}}. \tag{3.7}$$

Importantly Δr does not depend on N (providing the particles do not interact) because the events are independent meaning the uncertainty in the measured value of P_{D_1} scales as $1/\sqrt{N}$ and so we see the more particles we use the better the precision. We note that inputting N copies of $|\psi_0\rangle = |1,0\rangle_{0,1}$ is equivalent to inputting $|N,0\rangle_{0,1}$.

We will now show how the uncertainty in the value of ϕ can be quantified using a mathematical resource called quantum Fisher information, F_Q.

3.2 Fisher information

Recalling that the precision of an experiment describes its ability to reproduce results when experimental conditions are unchanged we now introduce a way to calculate a numerical value for the ultimate precision of any experiment. However we will

first develop an intuitive feel for possible ways to quantify precision. Consider two experiments, each with N measurement results. If in one of these experiments each of the N results are similar whilst in the other experiment there are large differences in the N results we would intuitively say the first experiment gave the best results, that is the more precise results. One way to quantify this precision is to use the standard deviation of the N results which describes their variation from the mean result.

In the interferometer scheme described in section 3.1 we determined ϕ by counting the number of times D1 fired. However, because of statistical fluctuations, the observed frequency of D1 firing is only an approximation to the true value of P_{D_1} and we demonstrated that the experimenter's uncertainty of P_{D_1} is $\Delta P_{D_1} = \Delta r/\sqrt{N}$. Since ϕ is determined using the observed frequency of D1 firing the uncertainty associated with the experimental value of P_{D_1} leads to an uncertainty in the value of ϕ. Error propagation theory tells us this uncertainty is

$$\Delta\phi = \frac{\Delta P_{D_1}}{|\partial P_{D_1}/\partial\phi|} \propto \frac{1}{\sqrt{N}} \tag{3.8}$$

and so we see that, as we would expect, the precision of our phase measurement is also improved as the number of resources employed in the measurement is increased.[1]

However it may not always be feasible to increase the number of resources used in the measurement procedure. Nevertheless the precision can usually be improved through optimisation of the initial state or the phase read-out method. These optimised initial states and phase read-out procedures may not, however, always be created/performed by a 50:50 beam splitter. As such a more general representation of a phase measurement scheme is given in figure 3.2.

The focus of this thesis will be ways to improve precision for a given number of resources solely through optimisation of the initial state. Consequently we would

[1]The actual value of $\Delta\phi$ here has a phase dependency, as it does in many measurement schemes, that is there are phases for which the measurement is more sensitive than others. This does not tend to be a problem, however, since it is always possible to perform some initial crude measurement from which a rough value for ϕ can be determined. The phase can then be modified to coincide with the region of peak sensitivity.

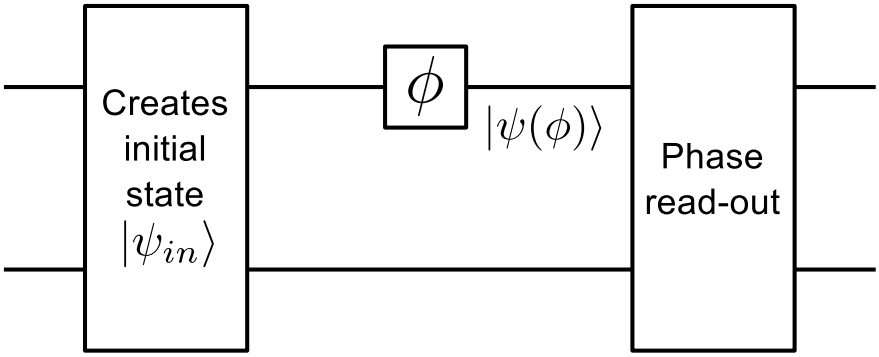

Figure 3.2: A general phase measurement scheme. The initial state $|\psi_{in}\rangle$ is created and then acquires a phase resulting in the state $|\psi(\phi)\rangle$. It is at this point that we calculate the F_Q. The phase is determined via some read-out procedure. In theory it is always possible to measure ϕ with the precision given by F_Q. In practice, however, it may not always be experimentally feasible.

like a way to determine the precision capabilities of a given state that is independent of the phase read-out procedure. Such a measure is given by the F_Q.[2] We introduce it by following the derivation given in reference [41]. This requires that we first give an intuitive derivation of the classical Fisher information bound followed by its extension to the quantum case.

3.2.1 Classical Fisher information

Generalised measurements are described by a set of non-negative Hermitian operators $X(x)$ where x is a particular measurement result and

$$\int X(x)\,dx = 1. \tag{3.9}$$

To determine ϕ in the interferometer set-up a measurement is performed on $\rho(\phi) = |\psi(\phi)\rangle\langle\psi(\phi)|$ and the measurement result x is recorded with probability density

$$p(x|\phi) = \mathrm{Tr}[X(x)\rho(\phi)]. \tag{3.10}$$

[2] F_Q gives the precision of a system when the read-out method has been optimised and it has been shown that theoretically the upper bound is always achievable [41]. In reality, of course, the optimum measurement protocol may not be physically practical and as such it is important to realise that F_Q is purely an upper bound used to compare the potential precision of different initial states. Read-out procedures will not be discussed in any great detail as it is beyond the scope of the thesis.

From this we estimate a value for ϕ using an estimator function $\phi_{est} = \phi_{est}(x_1, \ldots, x_N)$ which for a particular measurement result x gives an estimated value for ϕ of $\phi_{est}(x)$. We want the uncertainty in this estimated value of the phase to be as small as possible, i.e. we want to minimise the spread of the results,

$$(\Delta\phi)^2 = \int p(x|\phi)(\phi_{est}(x) - \phi)^2 \, dx. \tag{3.11}$$

Optimising the estimators for a given quantum measurement results in a classical bound on precision whilst further optimisation over all possible quantum measurements yields a quantum bound on precision which is ultimately what we want to achieve but first we look at the classical bound.

We assume the estimator is unbiased so that

$$\int (\phi_{est}(x) - \phi) p(x|\phi) \, dx = 0. \tag{3.12}$$

Differentiating this identity with respect to ϕ gives

$$\int (\phi_{est}(x) - \phi) p(x|\phi) \left(\frac{\partial \ln p(x|\phi)}{\partial \phi} \right) dx = 1. \tag{3.13}$$

If we then apply the Cauchy Schwarz inequality it can be shown that

$$\int (\phi_{est}(x) - \phi)^2 p(x|\phi) \, dx \int p(x|\phi) \left(\frac{\partial \ln p(x|\phi)}{\partial \phi} \right)^2 dx \geq 1 \tag{3.14}$$

or equivalently,

$$(\Delta\phi)^2 \geq \frac{1}{F} \tag{3.15}$$

where F is the classical Fisher information which is given by

$$F = \int p(x|\phi) \left(\frac{\partial \ln p(x|\phi)}{\partial \phi} \right)^2 dx = \int \frac{1}{p(x|\phi)} \left(\frac{\partial p(x|\phi)}{\partial \phi} \right)^2 dx. \tag{3.16}$$

Repeating the experiment ν times (i.e. making ν estimates of ϕ) improves this

precision to

$$(\Delta\phi)^2 \geq \frac{1}{\nu F}. \tag{3.17}$$

We now maximise F over all quantum measurements in order to determine F_Q.

3.2.2 Quantum Fisher information

The F_Q is, by definition, independent of the measurement procedure and as such we must remove all $X(x)$ terms from F in order to get an equation for F_Q. We do this here and show that it leads to an upper bound on the classical Fisher information.

First we introduce the symmetric logarithmic derivative, A, which is defined by

$$\frac{\partial\rho(\phi)}{\partial\phi} = \frac{1}{2}(A\rho(\phi) + \rho(\phi)A). \tag{3.18}$$

In the eigenbasis of $\rho(\phi)$ it is given by,

$$A_{j,k} = \frac{2}{\lambda_j + \lambda_k}\left[\frac{\partial\rho(\phi)}{\partial\phi}\right]_{j,k} \tag{3.19}$$

where $\lambda_{j,k}$ are the eigenvalues of $\rho(\phi)$. Whenever $\lambda_j + \lambda_k = 0$, $A_{j,k}$ is set to 0. The only property of A we need to know is that for Hermitian operators $\rho'(\phi)$ and B,

$$\mathrm{Tr}[B\rho'(\phi)] = \mathrm{Re}(\mathrm{Tr}[\rho(\phi)BA]) \tag{3.20}$$

where $\rho'(\phi) = \partial\rho(\phi)/\partial\phi$. As shown in equation 3.10 the probability distribution can be written in quantum form as $p(x|\phi) = \mathrm{Tr}[X\rho(\phi)]$ (where we have shortened $X(x)$ to X) which upon direct substitution into equation 3.16 gives

$$F_q = \int \frac{(\mathrm{Tr}[X\rho'(\phi)])^2}{\mathrm{Tr}[X\rho(\phi)]}dx. \tag{3.21}$$

Using property 3.20 F_q can be rewritten as

$$F_q = \int \frac{(\mathrm{Re}(\mathrm{Tr}[\rho(\phi)XA]))^2}{\mathrm{Tr}[X\rho(\phi)]}\,dx \leq \int \frac{|\mathrm{Tr}[\rho(\phi)XA]|^2}{\mathrm{Tr}[X\rho(\phi)]}\,dx = \tilde{F}_q. \tag{3.22}$$

Exploiting the cyclic nature of trace the integral on the far right can be rewritten as

$$\tilde{F}_q = \int \left| \mathrm{Tr}\left[\frac{\sqrt{\rho(\phi)}\sqrt{X}}{\sqrt{\mathrm{Tr}[X\rho(\phi)]}} \sqrt{X} A \sqrt{\rho(\phi)} \right] \right|^2 dx. \tag{3.23}$$

Finally, applying the Schwarz inequality $|\mathrm{Tr}[G^\dagger H]|^2 \leq \mathrm{Tr}[G^\dagger G]\mathrm{Tr}[H^\dagger H]$ gives

$$\tilde{F}_q \leq \int \mathrm{Tr}[XA\rho(\phi)A]\, dx = \mathrm{Tr}[\rho(\phi)A^2]. \tag{3.24}$$

The term on the far right is the quantum Fisher information

$$F_Q = \mathrm{Tr}[\rho(\phi)A^2] \tag{3.25}$$

which will be used throughout this thesis. We can see that it is independent of the measurement procedure as it has no dependence on the measurement outcomes x. It is related to the uncertainty of ϕ by

$$(\Delta\phi)^2 \geq \frac{1}{\nu F} \geq \frac{1}{\nu F_Q} \tag{3.26}$$

and determines the best possible precision with which a system can determine a parameter. It is true for both pure and mixed states, however, it can be simplified for pure states, $|\psi(\phi)\rangle$, to

$$F_Q = 4\left[\langle\psi'(\phi)|\psi'(\phi)\rangle - |\langle\psi'(\phi)|\psi(\phi)\rangle|^2\right] \tag{3.27}$$

where $|\psi'(\phi)\rangle = \partial|\psi(\phi)\rangle/\partial\phi$ and we have made use of the fact that for pure states $\rho^2 = \rho$, $\langle\psi(\phi)|\psi(\phi)\rangle = 1$ and $\partial\langle\psi(\phi)|\psi(\phi)\rangle/\partial\phi = 0$.

Another important property of F_Q that will be utilised later is that for two density matrices $\rho_1(\phi)$ and $\rho_2(\phi)$ that are supported on orthogonal subspaces and do not cease to be orthogonal for small changes in ϕ,

$$F_Q[p\rho_1(\phi) \oplus (1-p)\rho_2(\phi)] = pF_Q[\rho_1(\phi)] + (1-p)F_Q[\rho_2(\phi)] \tag{3.28}$$

where $F_Q[\cdot]$ denotes the F_Q of the state in brackets and p is the probability of being in the state $\rho_1(\phi)$. We also know that F_Q is convex, that is,

$$F_Q[p\rho_1(\phi) + (1-p)\rho_2(\phi)] \leq pF_Q[\rho_1(\phi)] + (1-p)F_Q[\rho_2(\phi)]. \tag{3.29}$$

This section has given a feel for the origin of the F_Q that will be used throughout this thesis to compare the precision of different initial states. We can see from equation 3.25 that it is independent of the measurement procedure thereby allowing us to focus solely on determining the best initial states to employ in measurement schemes.

3.3 Improving precision using entangled initial states

3.3.1 Unentangled initial states

In section 3.1 we discussed how a MZI could be used to measure a phase shift, ϕ. It was shown that inputting N copies of $|\psi_0\rangle = |1,0\rangle_{0,1}$, or equivalently inputting $|N,0\rangle_{0,1}$, into the interferometer allowed P_{D_1} to be determined with an uncertainty that scaled as $1/\sqrt{N}$. Using F_Q we can now show that this initial state allows ϕ to be determined with a precision that also scales as $1/\sqrt{N}$. This scaling is called the standard quantum limit (SQL) and is the best possible precision achievable when a classical initial state [3] is used to determine ϕ. At this point we note that the precision calculations in this section, and throughout the thesis, represent the precisions attainable on one experimental run. Any repetitions improve the precision by a factor of $1/\sqrt{\nu}$ (where ν is the number of repetitions) regardless of the initial state and as such we gain nothing, when comparing the precision capabilities of different initial states, by including this factor.

To calculate F_Q we must first determine how $|N,0\rangle_{0,1}$ is transformed by BS1.

[3] A classical, or unentangled, state is a state which has no quantum correlations between the particles.

Writing $|N,0\rangle_{0,1}$ in operator form it is easy to show

$$\frac{(a_0^\dagger)^N}{\sqrt{N!}}|0,0\rangle_{0,1} \xrightarrow{BS1} \frac{1}{\sqrt{2^N N!}}(ia_2^\dagger + a_3^\dagger)^N|0,0\rangle_{2,3} = \frac{1}{\sqrt{2^N}}\sum_{n=0}^{N}\binom{N}{n}^{1/2} i^n|n,N-n\rangle_{2,3}. \tag{3.30}$$

This is the state of the system immediately prior to the phase application, $|\psi_{in}\rangle$. Applying the unitary phase operation then gives

$$|\psi(\phi)\rangle = \frac{1}{\sqrt{2^N}}\sum_{n=0}^{N}\binom{N}{n}^{1/2} e^{in\phi}i^n|n,N-n\rangle_{2,3} \tag{3.31}$$

from which we can determine $F_Q = N$ using equation 3.27. From equation 3.26 the uncertainty in the measured value of ϕ, after one run of the experiment, is $\Delta\phi = 1/\sqrt{N}$. This is the best possible precision achievable using classical initial states. It is the same precision scaling that is found when the initial state is created by inputting a coherent state, with average particle number $\bar{n}$, and a vacuum state into the two ports of a 50:50 beam splitter. This is because a coherent state is a classical state in that there are no quantum correlations between the particles.

From this scaling it is clear that the more particles employed in the scheme, the better the precision of the phase measurement. However, the gain in precision comes at the cost of requiring an increase in the number of resources employed. Ideally, we would increase precision without having to increase the number of resources used, i.e. we would improve the scaling of the precision with N. It turns out this can be done by introducing quantum correlations between the particles.

3.3.2 Squeezed states

One of the first proposals to improve the precision scaling of phase measurements with N came from Caves in 1981 [42]. He proposed 'squeezing' the input to a MZI in order to reduce fluctuations in the phase measurement. We now briefly describe the idea behind this proposal.

We have shown that classical initial states achieve the SQL and that one such example of a classical initial state is achieved by inputting $|\psi_0\rangle = |\alpha,0\rangle_{0,1}$ into a 50:50

beam splitter. Here $|\alpha\rangle$ is a coherent state with mean particle number $\bar{n} = |\alpha|^2$ and $|0\rangle$ is a vacuum state, or equivalently, a coherent state with zero amplitude. These states can be described in terms of quadrature operators $X_1 = (a + a^\dagger)$ and $X_2 = -i(a - a^\dagger)$ which satisfy the commutation relation $[X_1, X_2] = 2i$ and the uncertainty relation $\Delta X_1 \Delta X_2 \geq 1$. They are minimum uncertainty states since $\Delta X_1 \Delta X_2 = 1$ and they also have equal fluctuations in each quadrature, $\Delta X_1 = \Delta X_2 = 1$. They can be represented by error circles in phase space, as shown in figure 3.3.

However, there are other minimum uncertainty states for which $\Delta X_1 \neq \Delta X_2$, that is, the uncertainty in one quadrature can be decreased at the expense of increased uncertainty in the second quadrature. These states are called squeezed coherent states. It should be noted, however, that general squeezed states do not have to, and usually do not, equalise the uncertainty relation. All that is needed for a state to be squeezed is $\Delta X_1 \neq \Delta X_2$ and $\Delta X_1 \Delta X_2 \geq 1$. A squeezed coherent state is most often represented as $|\alpha_\xi\rangle$ where α is the amplitude and $\xi = re^{i\theta}$ is the squeezing parameter. Here $0 \leq r < \infty$ is the magnitude of the squeezing and $0 \leq \theta \leq 2\pi$ is its direction. These states are far from a theoretical quirk. They were first produced in a laboratory in 1985 [43] and since then have been demonstrated in a diverse range of optical and atomic systems.

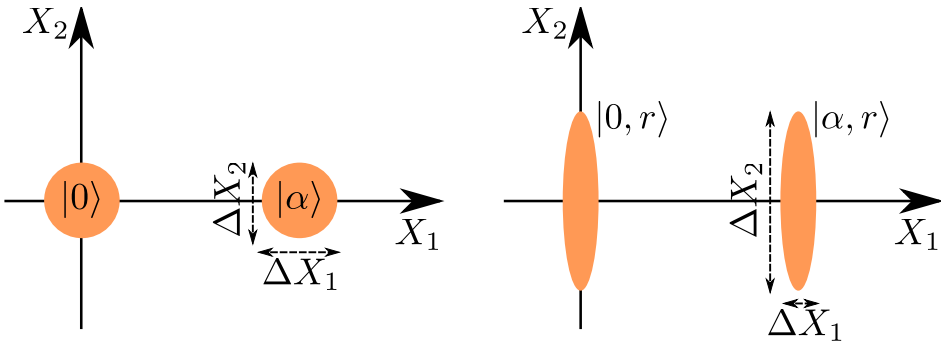

Figure 3.3: Left: Phase space representation of a vacuum, $|0\rangle$, and a coherent state, $|\alpha\rangle$. The centre of each circle is the amplitude of the state and the shaded area is the region of uncertainty. For simplicity the phase of the states has been set to $\theta = 0$. Left: The same but for a squeezed vacuum, $|0_\xi\rangle$, and a squeezed coherent state, $|\alpha_\xi\rangle$. We see the state is squeezed so that the fluctuations in the X_1 quadrature are less than those of $|\alpha\rangle$. This comes at the expense of increasing the uncertainty in the X_2 quadrature.

Figure 3.3 shows a squeezed vacuum state and a squeezed coherent state with amplitude α. In both cases the fluctuations in the X_1 quadrature are reduced by increasing the fluctuations in the X_2 quadrature. This makes them ideal for precision measurement schemes as by reducing the noise in one quadrature to much less than that of a coherent state we should be able to beat the SQL. It was shown that one way to beat the SQL using squeezed states is to input a coherent state into one input port of a standard MZI (see figure 3.1) and a squeezed vacuum into the second port [42]. As usual ϕ is determined by counting the number of particles detected at each output. This system allows the phase to be determined with precision

$$\Delta\phi = \sqrt{\frac{\bar{n}\exp(-2r) + \sinh^2(r)}{(\bar{n} - \sinh^2(r))^2}}. \tag{3.32}$$

Immediately it is clear that this MZI system allows for precision scalings better than the SQL. For example, when $\sinh^2(r) \ll |\alpha|^2$ the precision scales as $\Delta\phi \approx e^{-r}/\sqrt{\bar{n}}$. Such precisions have been demonstrated experimentally [44, 45] highlighting the true potential of squeezed states in measurement schemes.

Nevertheless, it should be noted that increasing r indefinitely does not lead to a continued increase in precision. This is because the read-out of a MZI measures the difference in the number of particles at the two output ports. Increasing squeezing increases the number of particles in the vacuum and thereby reduces the difference in the number of particles at the two output ports. Consequently the precision is degraded. It can be shown that in the MZI set-up of figure 3.1 where the read-out method involves measuring the difference in particle number at the two output ports the best possible precision for $\bar{n} \gg 1$ is $\Delta\phi \approx \bar{n}^{-3/4}$. Clearly this is an improvement on the SQL and as such squeezed states are highly valuable to the metrology community. However precision scalings can be improved further still by introducing quantum correlations between the particles as was first suggested by Yurke in 1986 [46]. In fact, by using highly entangled states the precision scaling can be improved to $1/N$. This scaling is called the Heisenberg limit and is the ultimate precision allowed by any system. Such highly entangled states are discussed in the

next subsection.

First, however, we note that the precision scaling of $\Delta\phi \approx \bar{n}^{-3/4}$ has not been calculated using the F_Q. Instead it depends on the phase read-out procedure which, in this case, involved counting the number of particles detected at each output port of a MZI. In 2008 [47] it was shown that the precision of squeezed states could be improved to the Heisenberg precision scaling of $1/\bar{n}$ when the phase read-out method employed is optimised. It was found that this scaling could also be attributed to entanglement created between the two modes of the MZI by BS1.

For the most part of this thesis we will be investigating ways to improve measurement precision using atomic Fock states which, unlike coherent states, cannot be squeezed in the conventional sense as there are no number fluctuations. However, in 1986 Yurke showed that by inputting an equal number of particles into each input port of a MZI in a highly entangled fashion, it was possible to achieve Heisenberg limited precision [46]. Since then other entangled states have been proposed to improve measurement precision. One such state that provides a theoretically simple way to reach the Heisenberg limit is the maximally entangled NOON state.

3.3.3 NOON states

The best possible phase precision attainable with N particles is given by the Heisenberg limit $\Delta\phi \sim 1/N$, so called due to its likeness to a Heisenberg uncertainty relation, i.e. $\Delta\phi\Delta N \gtrsim 1$. [4] Perhaps the simplest example of a measurement scheme that uses entangled particles to achieve Heisenberg limited precision is given by a MZI set-up in which the Hong-Ou-Mandel effect is employed [48].

So far we have shown that inputting $|\psi_0\rangle = |2,0\rangle_{0,1}$ into a MZI allows us to measure ϕ with a precision $\Delta\phi = 1/\sqrt{2}$. We will now show that inputting the same number of resources in a different fashion improves this precision to $1/2$. All we

[4] As a general rule increasing particle number uncertainty leads to a decrease in phase uncertainty, $\Delta\phi\Delta N \gtrsim 1$ as discussed earlier. Since the maximum uncertainty in the particle number for a system with N particles is $\Delta N = N$ this implies the minimum phase uncertainty is $\Delta\phi \sim 1/N$. This, however, is not a true Heisenberg uncertainty relation as there is no (undisputed) Hermitian phase operator.

need to do is input our two particles into the two different input modes of the MZI. This means the input state is given by $|\psi_0\rangle = |1,1\rangle_{0,1}$ which, using equation 3.1, is transformed by BS1 to

$$|1,1\rangle_{0,1} \xrightarrow{BS1} \frac{1}{\sqrt{2}}(|2,0\rangle_{2,3} + |0,2\rangle_{2,3}) \tag{3.33}$$

where a global phase has been ignored. Immediately it is apparent that there are correlations between the two particles as we see that they both travel along mode 2 and both along mode 3, they are always 'stuck' together. This means that when the unitary phase operation is applied the relative phase will be twice the size of the relative phase when $|\psi_0\rangle = |2,0\rangle_{0,1}$. That is,

$$\frac{1}{\sqrt{2}}(|2,0\rangle_{2,3} + |0,2\rangle_{2,3}) \xrightarrow{\phi} \frac{1}{\sqrt{2}}(e^{i2\phi}|2,0\rangle_{2,3} + |0,2\rangle_{2,3}). \tag{3.34}$$

We determine the precision afforded by this state using F_Q as described in section 3.2. Since the state of the system after the application of the phase, $|\psi(\phi)\rangle$, is a pure state we can calculate its F_Q using equation 3.27. We find $F_Q = 4$ which, using the Cramer-Rao bound, gives a lower bound on the precision of $\Delta\phi = 1/2$. This is the Heisenberg limited precision scaling of $1/N$ which is the best precision scaling allowed by quantum mechanics. And so we have shown that for a MZI with two particles, the precision of the measurement of ϕ can be improved by a factor of $\sqrt{2}$ by inputting the particles in a different way.

Inputting $|1,1\rangle_{0,1}$ into the MZI resulted in an initial state $|\psi_{in}\rangle = (|2,0\rangle_{2,3} + |0,2\rangle_{2,3})/\sqrt{2}$. This is a two particle balanced NOON state. A NOON state is defined as a state of the form $(|N,0\rangle + |0,N\rangle)/\sqrt{2}$ where the terms in the kets represent the number of particles in two different modes. Applying the unitary phase operator to a N particle NOON state results in $|\psi(\phi)\rangle = (e^{iN\phi}|N,0\rangle + |0,N\rangle)/\sqrt{2}$ which, using equations 3.27 and 3.26, can be shown to have precision $\Delta\phi = 1/N$. This is Heisenberg limited precision and as such balanced NOON states are ideal measurement tools as their precision cannot be beaten.

However, there are two major problems when it comes to using NOON states to make precision measurements. Firstly, they are very difficult to produce. Although we have shown a simple way to produce a two particle NOON state using only a 50:50 two-mode beam splitter with input $|1,1\rangle_{0,1}$ this idea does not extend to general N. Inputting $|N/2,N/2\rangle_{0,1}$ into a two-mode 50:50 beam splitter populates more than just the $|N,0\rangle_{2,3}$ and $|0,N\rangle_{2,3}$ states for all $N > 2$. Many different theoretical schemes have been proposed to produce larger NOON states with both photons and atoms [49–53] (to mention just a few) and whilst there has been some success at implementing these schemes in the laboratory this success is limited as NOON state production for any more than 10 particles continues to elude experimentalists [54–59].

Yet by far the greatest problem of using NOON states for precision measurements is their extreme fragility to decoherence effects such as particle loss. The effects of particle loss on different initial states will be discussed in detail in the latter chapters of this thesis, for now, however, we give an intuitive feel as to the origin of this fragility.

When a state interacts with the environment it gives information to the environment about what state it is in. Indeed it is well known that in Young's double slit experiment as soon as there is information about which path the particle took, the superposition is destroyed and no interference fringes are observed. This happens regardless of whether or not the path taken is actually known but depends only on whether it could be known. The NOON state is therefore extremely fragile to particle loss because as soon as the environment 'knows' which mode a particle is in it also knows which mode the remaining $N-1$ particles are in, thereby completely destroying the superposition. The loss of only a single particle therefore prevents the readout of any phase information. This is in vast contrast to classical states where the loss of a single particle only informs the environment to the whereabouts of that particle and therefore results in the destruction of just one single particle superposition. The system still has another $N-1$ single particle superpositions from

which ϕ can be determined with precision $1/\sqrt{N-1}$.

The main point, however, is that while in idealised, theoretical schemes NOON states allow for extremely precise parameter estimation, the difficulties associated with their production and their lack of robustness to decoherence effects means they are unlikely to ever offer a realistic way to improve the precision of phase measurements. Nevertheless there are other quantum states that allow for more precise phase measurements than classical initial states but that are easier to produce and that are more robust to particle losses than NOON states. One such state is described in the next section.

3.3.4 Bat states

Bat states, so named because a plot of their amplitudes in the number basis resemble the ears of a bat (see figure 3.4), do not allow for quite as precise phase measurements as NOON states in an idealised system in which no particles are lost [60, 61]. However, they are easier to produce in a laboratory and, as will be discussed in more detail later in the thesis, are much more robust to particle losses.

To produce a bat state an equal number of particles are put into each input port of a 50:50 beam splitter [60, 62]. This results in the output

$$|N/2, N/2\rangle_{0,1} \xrightarrow{BS} \frac{1}{\sqrt{2^N}} \sum_{n=0}^{N/2} \frac{\sqrt{(2n)!(N-2n)!}}{n!(N/2-n)!} |2n, N-2n\rangle_{2,3} \tag{3.35}$$

from which we can determine the probability of detecting n particles in output mode 2 as shown in figure 3.4. As discussed in the previous section NOON states afford a Heisenberg limited precision scaling of $1/N$ since $\Delta N = N$. From figure 3.4 we see that for the bat state $\Delta N \sim N$ which suggests these states will allow for a similar precision scaling to the NOON state [60, 62]. In fact using equations 3.27 and 3.35 the F_Q of the bat state can be shown to be $N(N/2+1)$ which means that for large N the precision scaling is $\Delta\phi \approx \sqrt{2}/N$ [63] which is only a factor of $\sqrt{2}$ worse than the NOON state.

It is thought that bat states should prove considerably simpler to produce in a

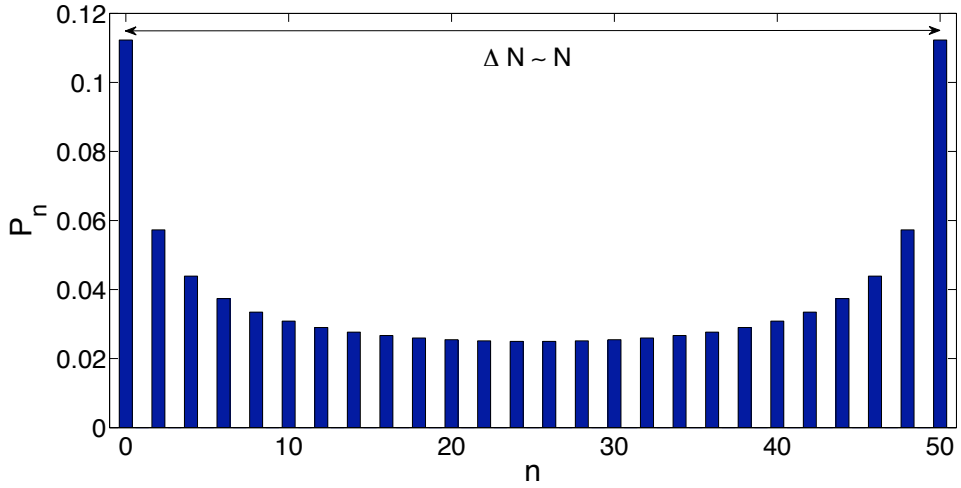

Figure 3.4: The probability distribution of a bat state for $N = 50$. We see that the particles are output from the beam splitter in pairs and that $\Delta N \sim N$.

laboratory than NOON states as all that is required is a state with equal numbers of particles in two modes, $|N/2, N/2\rangle$, incident on a 50:50 beam splitter. Producing the required dual Fock state is likely to prove the most problematic step towards the experimental demonstration of these states for large N. However, recent work has demonstrated a scalable route for producing heralded dual photonic Fock states [64] using parametric down conversion bringing the promised Heisenberg limited scaling one step closer. In contrast NOON state generation requires the use of complex linear networks [65] or large nonlinearities [66] making their experimental implementation difficult for any more than a few photons. Experimental advances have already been made towards producing the required dual Fock states for atoms too. Indeed in reference [67] approximate dual Fock states, with $N \sim 1000$, were created by loading a BEC into an optical lattice of two sites. Consequently it is beginning to look as though it may soon be experimentally possible to achieve Heisenberg limited precision.

Another major advantage of using bat states to make phase measurements over NOON states is that they soon outperform the precision capabilities of NOON states when particle losses are accounted for. This can been seen intuitively by considering what happens when one particle is lost from the system. As discussed in the previous

section the loss of only a single particle from a NOON state completely destroys the superposition thereby preventing the readout of any phase information. This is because as soon as one knows the location of a single particle they automatically know the location of the remaining $N-1$ particles. However, as can be seen from figure 3.4, there is a probability of particles being in other states besides $|N,0\rangle$ and $|0,N\rangle$ for the bat state which means that the loss of a particle to the environment does not automatically inform us of the location of the remaining particles. This robustness to loss will be shown rigorously in Chapter 6.

The fact that bat states afford approximately Heisenberg limited precision and that they are more robust to particle losses than NOON states makes them an ideal candidate for precision measurement schemes. In Chapter 6 we discuss a possible way to create an atomic bat state capable of precisely measuring small rotations and, as suggested here, show that it outperforms the precision capabilities of both classical initial states and NOON initial states in the presence of modest rates of particle loss. The loss model we use for these calculations will be introduced at the end of this chapter. First, however, we briefly mention some other techniques that have been suggested to improve measurement precision to below the SQL.

3.3.5 Multiple pass strategies

Motivated by the difficulties associated with producing NOON states and the extreme fragility of these states to particle losses, researchers, as well as searching for easier to produce and less fragile states, began to search for ways to reach the Heisenberg limit without the need for exotic quantum states. Instead they began to consider ways in which altering the interferometer itself may improve the precision scaling to $1/N$. One of the simplest techniques that resulted from this research is the multiple pass technique [68] where a classical beam of particles is allowed to pass through the phase shift q times thereby acquiring a multiple of the phase to be

measured as shown in figure 3.5. The general N particle classical initial state is

$$|\psi_{in}\rangle = \frac{1}{\sqrt{2^N}} \sum_{n=0}^{N} \binom{N}{n}^{1/2} |n, N-n\rangle \tag{3.36}$$

which upon passing through a phase shift q times becomes

$$|\psi(\phi)\rangle = \frac{1}{\sqrt{2^N}} \sum_{n=0}^{N} \binom{N}{n}^{1/2} e^{iqn\phi} |n, N-n\rangle. \tag{3.37}$$

Using equations 3.27 and 3.26, we determine the smallest possible uncertainty in our measurement of ϕ to be

$$\Delta\phi = \frac{1}{q\sqrt{N}}. \tag{3.38}$$

This implies we can achieve arbitrary precision simply by increasing the number of times the particles pass through the phase shift, thereby, violating the Heisenberg limit. However, each application of the phase shift is a resource. This is evident when we consider a sensitive sample (phase shift), such as a biological one, where the passage of particles through the sample leads to damage. The goal, therefore, is to make as few passages as possible through the sample and as such every passage of a particle through the phase shift must be accounted for.

Therefore, if we wish to fix the total number of resources employed in the scheme to N the intensity of the particles passing through the phase shift on each cycle must be reduced to N/q. This results in an uncertainty of $\Delta\phi = 1/\sqrt{qN}$ which is consistent with the Heisenberg limit since $q \leq N$ otherwise we would be passing less than one particle through the sample at a time which is obviously unphysical.

Despite the apparent success of this scheme at demonstrating Heisenberg limited phase measurements [68, 69] the technique is regarded by some as a change to the rules of precision measurement protocols and as such the Heisenberg limited nature of the measurements are still debated [70]. Recent work has since shown that the multiple pass technique performs significantly worse than optimal quantum states (these states will be discussed later in the thesis) in the presence of particle losses [70]. We note also that in principal every measurement scheme could employ a

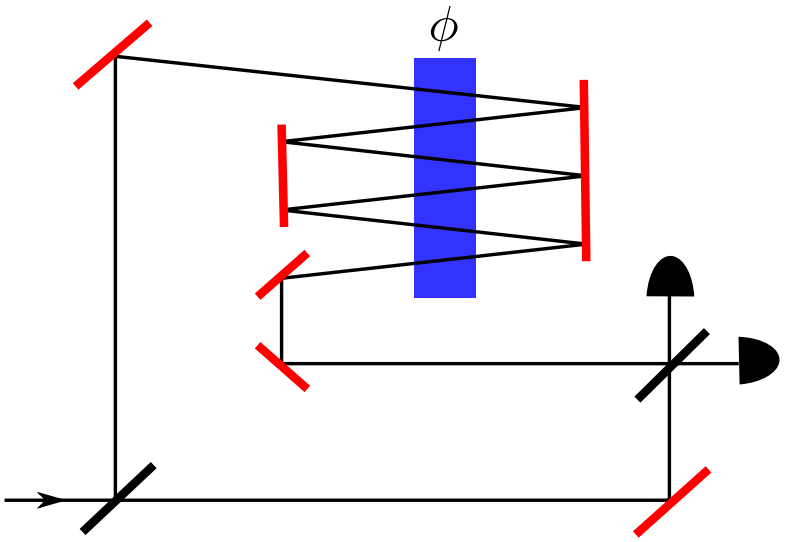

Figure 3.5: A multiple pass interferometer. The black bold lines represent beam splitters, the bold red lines represent mirrors and the blue shaded area is the phase shift. After the first beam splitter each particle is in a superposition of being in both paths. The upper path then acquires a phase shift, $q\phi$, and the paths are recombined at a final beam splitter. Here $q = 6$ whilst in a standard MZI $q = 1$.

multiple pass strategy. In order to compare performances fairly we therefore need to consider their precision capabilities after just a single pass. As such the focus of this thesis is finding ways to improve measurement precision using quantum states.

3.3.6 Nonlinearities

The final technique we mention that has been proposed to improve measurement precision beyond the SQL uses nonlinear couplings between the parameter to be measured and the probe. Reference [71], for example, developed a parameter estimation scheme, which through the use of two-body interactions was capable of a precision scaling of $1/N^{3/2}$. Other work has demonstrated the potential to achieve precision scalings of $1/N^y$ (where y is an integer and $y \geq 0$) [72] and 2^{-N} [73] through the use of nonlinearities. Bose-Einstein condensates with their particle interactions naturally lend themselves to these schemes. The challenge, however, is finding ways to couple the parameter we wish to measure with the particle interactions. Consequently, in this thesis, we focus on improving measurement precision in linear systems.

We also note that whilst these scalings appear to violate the Heisenberg limit it is now thought that these schemes misinterpret the resources required and so the Heisenberg limit is indeed fundamental [12].

Now that we have introduced ways to improve measurement precision beyond what is possible classically we begin to consider the effects of particle losses on these schemes. We introduce the loss model that will be used throughout this thesis below.

3.4 Particle loss model

Particle loss is the most detrimental form of decoherence in precision measurement schemes and attempting to reduce its effect will form the basis of a large section of this thesis. The most common way to model the loss of particles to the environment is to introduce imaginary beam splitters to the system whose transmissivity, η, is directly related to the rate of loss as shown in figure 3.6. This loss model has been used in much work that studies the effects of particle loss on the precision of phase measurements [1, 2, 74, 75] and is the model that will be used throughout this thesis.

3.4.1 Imaginary beam splitter model

Using this model it is easy to determine the effect of losses on any general pure two-mode initial state $|\psi_{in}\rangle = \sum_{n=0}^{N} \beta_n |n, N-n\rangle$ [1, 2]. To do this we begin by considering how $|n, N-n\rangle$ is transformed by the imaginary beam splitters. Writing this general initial state in terms of creation and annihilations operators

$$\sum_{n=0}^{N} \beta_n |n, N-n\rangle = \sum_{n=0}^{N} \frac{\beta_n}{\sqrt{n!(N-n)!}} (a_0^\dagger)^n (a_1^\dagger)^{N-n} |0,0\rangle \tag{3.39}$$

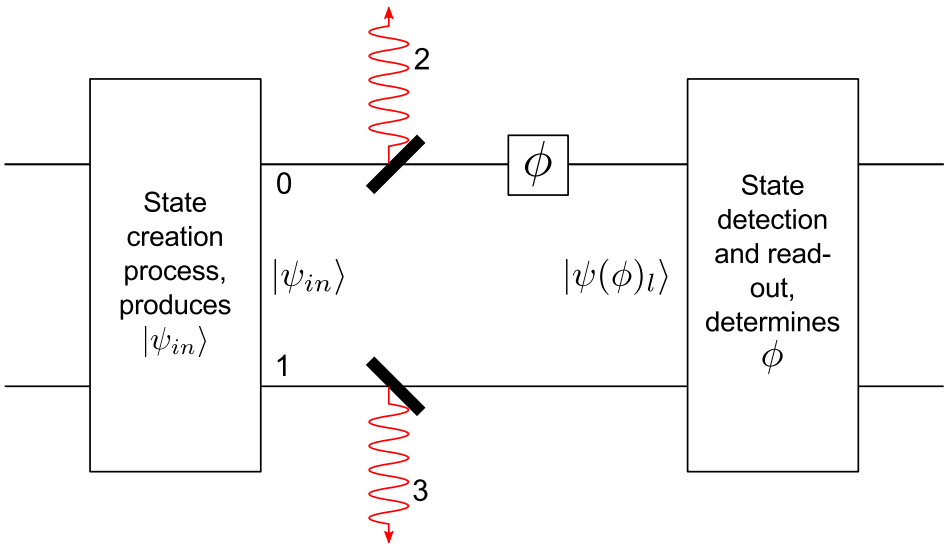

Figure 3.6: The first box represents the state creation process and the second box represents the phase read-out procedure. The bold diagonal lines in the two modes are imaginary beam splitters with transmissivities $\eta_{0,1}$. When $\eta_{0(1)} = 1$ no particles are lost from mode 0(1). However for all $\eta_{0,1} < 1$ particles are lost, with the amount of loss increasing with decreasing $\eta_{0,1}$. The loss of particles to the environment is shown by the red lines.

we can see that the imaginary beam splitters transform it to

$$\begin{aligned}\sum_{n=0}^{N}\beta_n|n,N-n\rangle \quad &\xrightarrow{IBS} \quad \sum_{n=0}^{N}\frac{\beta_n}{\sqrt{n!(N-n)!}}(\sqrt{\eta_0}a_0^\dagger+\sqrt{1-\eta_0}a_2^\dagger)^n \\ &\times \quad (\sqrt{\eta_1}a_1^\dagger+\sqrt{1-\eta_1}a_3^\dagger)^{N-n}|0,0\rangle_{0,1}\otimes|0,0\rangle_{2,3} \\ &= \quad \sum_{n=0}^{N}\beta_n\sum_{l_0=0}^{n}\sum_{l_1=0}^{N-n}\sqrt{B^n_{l_0l_1}}|n-l_0,N-n-l_1\rangle_{0,1}\otimes|l_0,l_1\rangle_{2,3}\end{aligned} \tag{3.40}$$

where l_0 and l_1 are the number of particles lost from modes 0 and 1 respectively and

$$B^n_{l_0l_1}=\binom{n}{l_0}\binom{N-n}{l_1}\eta_0^n(\eta_0^{-1}-1)^{l_0}\eta_1^{N-n}(\eta_1^{-1}-1)^{l_1}. \tag{3.41}$$

Applying the phase shift, ϕ, gives

$$|\psi(\phi)_l\rangle=\sum_{n=0}^{N}\beta_n\sum_{l_0=0}^{n}\sum_{l_1=0}^{N-n}\sqrt{B^n_{l_0l_1}}e^{i(n-l_0)\phi}|n-l_0,N-n-l_1\rangle_{0,1}\otimes|l_0,l_1\rangle_{2,3}. \tag{3.42}$$

We could equally well have applied the phase shift before, or at the same time as, the imaginary beam splitter transformations. In all cases the expression we obtain for the F_Q is the same meaning it is irrelevant whether the particles are lost before, during, or after the phase shift is applied.

When particles are lost from the system to the environment the system loses all information about them and as such any calculation of F_Q should not involve modes 2 and 3. We therefore trace out these modes and find the state of the system before the read-out procedure is given by

$$\rho(\phi) = \sum_{l_0=0}^{N} \sum_{l_1=0}^{N-l_0} p_{l_0,l_1} |\xi_{l_0,l_1}(\phi)\rangle\langle\xi_{l_0,l_1}(\phi)| \tag{3.43}$$

where

$$|\xi_{l_0,l_1}(\phi)\rangle = \frac{1}{\sqrt{p_{l_0,l_1}}} \sum_{n=l_0}^{N-l_1} \beta_n e^{in\phi} \sqrt{B^n_{l_0,l_1}} |n-l_0, N-n-l_1\rangle_{0,1}. \tag{3.44}$$

and p_{l_0,l_1} is the probability l_0 and l_1 particles are lost from modes 0 and 1 respectively. We can then determine the F_Q of the system using the relation of equation 3.28 since states with a different total number of lost photons, $l = l_0 + l_1$, are orthogonal. This gives the total F_Q of the system

$$F_Q = \sum_{l=0}^{N} F_Q \left[\sum_{l_0=0}^{l} p_{l_0,l-l_0} |\xi_{l_0,l-l_0}(\phi)\rangle\langle\xi_{l_0,l-l_0}(\phi)| \right] \tag{3.45}$$

where $F_Q[\cdot]$ is once again the F_Q of the state in brackets. Using this result we will now rigorously demonstrate the extreme fragility of NOON states to particle loss and we will compare this fragility to that of an unentangled initial state. This is intended as an introduction to the loss calculations that will appear in several of the latter chapters of this thesis.

In general calculating F_Q from equation 3.45 requires solving a complicated eigenvalue problem which makes analytical determination of F_Q difficult. However, for the specific case of a NOON state the problem can be simplified as we will now

demonstrate.

As already mentioned in section 3.3 the loss of only a single particle from a NOON state completely destroys the superposition since the environment 'knows' which mode all the particles are occupying. Consequently the only $|\xi_{l_0,l-l_0}(\phi)\rangle$ that will contribute to F_Q is $|\xi_{0,0}(\phi)\rangle$ and we can write

$$F_Q = p_{0,0} F_Q \left[|\xi_{0,0}(\phi)\rangle\langle\xi_{0,0}(\phi)| \right]. \tag{3.46}$$

For a NOON initial state,

$$\beta_n = \begin{cases} 1/\sqrt{2} & \text{for } n = 0, N \\ 0 & \text{for } n \neq 0, N \end{cases}$$

meaning

$$|\xi_{0,0}(\phi)\rangle = \frac{1}{\sqrt{2p_{0,0}}}(e^{iN\phi}\sqrt{\eta_0^N}|N,0\rangle_{0,1} + \sqrt{\eta_1^N}|0,N\rangle_{0,1}). \tag{3.47}$$

Using equation 3.27

$$F_Q[\xi_{0,0}] = 4\left(\frac{1}{2p_{0,0}}N^2\eta_0^N - \left|\frac{1}{2p_{0,0}}iN\eta_0^N\right|^2\right) \tag{3.48}$$

and the requirement that $\langle\xi_{0,0}|\xi_{0,0}\rangle = 1$ means $p_{0,0} = (\eta_0^N + \eta_1^N)/2$. Substituting into equation 3.46 gives,

$$F_{Q_{NOON}} = \frac{2N^2\eta_0^N\eta_1^N}{\eta_0^N + \eta_1^N} \tag{3.49}$$

from which it is possible to determine the precision of a system employing a NOON initial state for any rate of loss on either path. Realising that an unentangled initial state is equivalent to N single particle NOON states the F_Q of a system employing an unentangled initial state (i.e. the state resulting from inputting N atoms into one port of a 50:50 beam splitter) follows naturally as

$$F_{Q_U} = \frac{2N\eta_0\eta_1}{\eta_0 + \eta_1}. \tag{3.50}$$

Figure 3.7 shows the precision of the NOON state and the unentangled state for two different scenarios, the case of loss in just one mode and the case of equal amounts of loss in both modes for $N = 10$. In both cases the NOON state offers the best precision in the idealised case where there is no loss. However, as the rate of loss increases the unentangled state soon outperforms the NOON state. It is also important to note that as N increases the NOON state loses its precision more rapidly as can be seen from equation 3.49. This means that for large numbers of particles, as are required in precision measurement schemes, the NOON state outperforms the unentangled state for a smaller range of values of η.

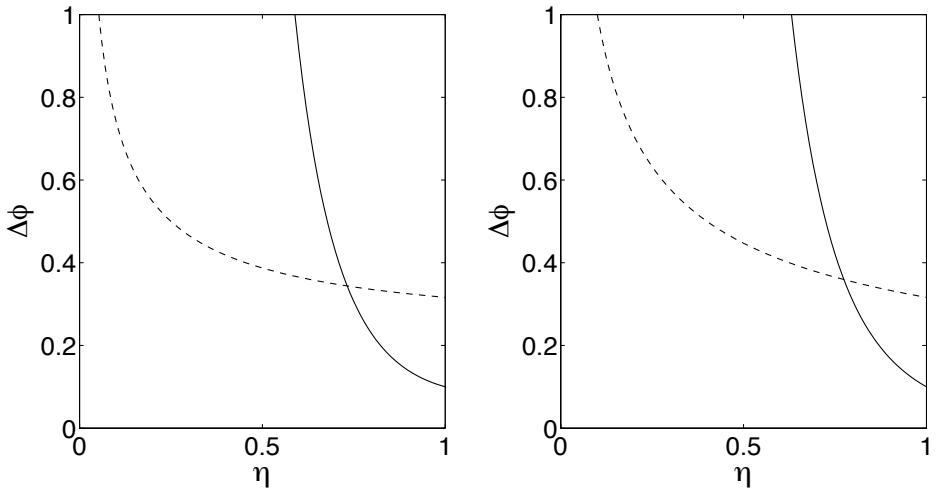

Figure 3.7: Left: The precision of a NOON initial state (solid line) and an unentangled initial state (dashed line) for loss in just one mode, i.e. $\eta_0 = \eta$ and $\eta_1 = 1$ for $N = 10$. Right: The same but for the case of equal loss in both modes, that is $\eta_0 = \eta_1 = \eta$. In both cases the NOON state offers the most precise measurements in the idealised case, however it is soon outperformed by the unentangled state.

Consequently there is an ongoing search to find initial states that find a balance between the need for precision and the need for robustness to particle loss, i.e. a state that is both precise and robust. Any state that outperforms an unentangled initial state for experimentally realistic loss rates is of fundamental interest to the metrology community.

3.4.2 Master equation approach

At this point we note that particle loss from a two-mode interferometer can equivalently be described by a master equation of the form,

$$\dot{\rho} = \frac{\Gamma_0}{2}\left(2a_0\rho a_0^\dagger - \rho a_0^\dagger a_0 - a_0^\dagger a_0\rho\right) + \frac{\Gamma_1}{2}\left(2a_1\rho a_1^\dagger - \rho a_1^\dagger a_1 - a_1^\dagger a_1\rho\right) \tag{3.51}$$

where ρ is the density matrix of the system, $\dot{\rho} = \partial\rho/\partial t$ and $\Gamma_{0,1} = |\ln\eta_{0,1}|/t$. We prove this equivalence below noting that we need only consider one mode since the master equation above treats each mode independently.

The interaction of interferometric mode 0 with the environment via a beam splitter is given by

$$I = \theta_0(a_0^\dagger b + b^\dagger a_0) \tag{3.52}$$

where b ($b^\dagger$) annihilates (creates) a particle in the environment and $\cos^2(\theta_0) = \eta_0$. We treat the environment as a mixed state and make the assumption that it and the interferometric mode are initially uncorrelated, that is, the density matrix describing the path and the environment at time $t = 0$ is

$$\rho_T(0) = \rho(0) \otimes \rho_e(0) \tag{3.53}$$

where $\rho(0)$ is the density matrix of the interferometric mode at $t = 0$ and $\rho_e(0)$ is the density matrix describing the environment at the same time. As in the standard master equation derivation we also assume that the environment is large and is therefore little changed by this interaction meaning $\rho_T(t) = \rho(t) \otimes \rho_e(0)$. Evolving the system under the interaction for a short time dt gives

$$\rho_T(t + dt) = e^{i\theta_0 dt(a_0^\dagger b + b^\dagger a_0)}\rho_T(t)e^{-i\theta_0 dt(a_0^\dagger b + b^\dagger a_0)}. \tag{3.54}$$

If we then expand the exponentials, retaining terms up to second order in dt only (in accordance with typical master equation derivations), and trace out the environment

we get

$$\begin{aligned}\rho(t+dt) = \rho(t) + i\theta_0 dt(a_0^\dagger \rho(t)\langle b\rangle + a_0\rho(t)\langle b^\dagger\rangle) - i\theta_0 dt(\rho(t)a_0^\dagger\langle b\rangle + \rho(t)a_0\langle b^\dagger\rangle) \\ +\theta_0^2(dt)^2(a_0^\dagger\rho(t)a_0^\dagger\langle b^2\rangle + a_0^\dagger\rho(t)a_0\langle b^\dagger b\rangle + a_0\rho(t)a_0^\dagger\langle bb^\dagger\rangle + a_0\rho(t)a_0\langle(b^\dagger)^2\rangle) \\ -\frac{\theta_0^2}{2}(dt)^2((a_0^\dagger)^2\rho(t)\langle b^2\rangle + a_0^\dagger a_0\rho(t)\langle bb^\dagger\rangle + a_0a_0^\dagger\rho(t)\langle b^\dagger b\rangle + a_0^2\rho(t)\langle(b^\dagger)^2\rangle) \\ -\frac{\theta_0^2}{2}(dt)^2(\rho(t)(a_0^\dagger)^2\langle b^2\rangle + \rho(t)a_0^\dagger a_0\langle bb^\dagger\rangle + \rho(t)a_0a_0^\dagger\langle b^\dagger b\rangle + \rho(t)a_0^2\langle(b^\dagger)^2\rangle).\end{aligned} \tag{3.55}$$

However, since we are treating the environment as a mixed state we have

$$\langle b\rangle = \langle b^\dagger\rangle = \langle b^2\rangle = \langle(b^\dagger)^2\rangle = 0 \tag{3.56}$$

and taking the mean number of particles in the environment to be zero means

$$\langle b^\dagger b\rangle = 0 \ \text{ and } \ \langle bb^\dagger\rangle = 1. \tag{3.57}$$

Substituting these values into equation 3.56 gives

$$\rho(t+dt) = \rho(t) + \frac{\theta_0^2}{2}(dt)^2(2a_0\rho(t)a_0^\dagger - a_0^\dagger a_0\rho(t) - \rho(t)a_0^\dagger a_0) \tag{3.58}$$

and consequently

$$\dot\rho(t) = \frac{\theta_0^2}{2}dt(2a_0\rho(t)a_0^\dagger - a_0^\dagger a_0\rho(t) - \rho(t)a_0^\dagger a_0). \tag{3.59}$$

The fraction of the total number of particles left in interferometric mode 0 after a time dt is given by $\cos^2(\theta_0 dt)$ which is equivalent to $e^{-\Gamma_0 dt}$ where Γ_0 is the rate of damping. Expanding the cosine and the exponential it can be shown that $\theta_0^2 dt = \Gamma_0$. Substituting this into equation 3.59 gives

$$\dot\rho = \frac{\Gamma_0}{2}\left(2a_0\rho a_0^\dagger - \rho a_0^\dagger a_0 - a_0^\dagger a_0\rho\right) \tag{3.60}$$

which is the master equation for a damped harmonic oscillator. Similarly loss on the

second interferometric path can be equivalently described by a master equation as above or by the imaginary beam splitter approach in the previous subsection. The master equation loss formula will prove useful in Chapter 7 where it is necessary to model loss in many different modes which, as we have seen here, can be treated independently.

3.5 Uses of precision measurements in quantum technologies

As well as being a fundamental tool in the confirmation of scientific theories ultra-precise parameter estimation has found uses in more diverse fields. Here we give an overview of two uses of quantum-enhanced parameter estimation. There are, however, many other uses of quantum precision measurement protocols and this is intended merely to provide motivation for the current interest in quantum metrology.

3.5.1 Frequency standards

Precise time or frequency measurements are essential for telecommunications, broadcasting and navigation as well as in many scientific experiments. To measure time precisely we usually begin with N cold ions, most commonly caesium, in the ground state. A carefully chosen electromagnetic pulse is then used to send each ion into an equally weighted superposition of being in the ground and first excited state, $(|0\rangle + |1\rangle)/\sqrt{2}$. The system is now left to evolve freely for a time t, thereby introducing a phase factor between the $|0\rangle$ and $|1\rangle$ states. The acquired phase is given by $\phi = ft$ where f is the frequency of the ground to excited state transition. Finally a second, identical, electromagnetic pulse is applied to the system and the number of ions found in the state $|0\rangle$ is recorded. This procedure is almost equivalent to a MZI with the ground and excited states corresponding to the two interferometer modes, the only difference is the phase here has a time dependence. Since we know that for a MZI the precision of ϕ, when the N particles are unentangled, scales as $1/\sqrt{N}$ the same will be true here meaning $\Delta f = 1/(\sqrt{N}t)$.

We saw in section 3.3 that employing NOON states as the initial state improved the precision scaling of the MZI to $1/N$. Likewise employing a state of the form $(|0,0\ldots,0\rangle_{0,1,\ldots,N} + |1,1,\ldots,1\rangle_{0,1,\ldots,N})/\sqrt{2}$ in the set-up here gives $\Delta f = 1/(Nt)$ thus allowing for much more precise time or frequency measurements [76, 77].

3.5.2 Lithography

Closely related to precise phase measurements is the field of quantum lithography and in fact it employs many of the same techniques. Optical lithography is the process by which light is used to imprint a pattern on a substrate. It is a valuable tool in the semiconductor industry as it allows circuit images to be transferred onto chips on a vast scale. However, diffraction effects limit the minimum resolvable feature size on the chip to the Rayleigh diffraction limit of $\lambda/2$ where λ is the wavelength of the light used. Consequently, as smaller and smaller features are required it is necessary to use light with a shorter and shorter wavelength. However, it is not always practical to decrease λ. Fortunately, it has been shown that by exploiting quantum effects the minimum resolvable feature size can be decreased to $\lambda/(2N)$ where N is the number of photons employed in the procedure [78]. This $1/N$ improvement in resolution is achieved using a NOON state and arises for the same reasons as discussed in section 3.3. A proof of principal demonstration of this super-resolution was demonstrated for $N = 2$ in reference [79] and later for $N = 4$ in references [56, 57].

3.5.3 Gyroscopes

A further use of precision measurement schemes is in the navigation industry where ultra-precise gyroscopes are required for inertial navigation systems. These gyroscopes measure rates of rotation and at present, due to the difficulties associated with producing highly entangled quantum states and the extreme fragility of these states to particle loss, employ classical initial states as their resource. In this thesis we propose two experimentally realistic schemes that use quantum states to improve

gyroscopic precision even in the presence of particle loss. We introduce gyroscopes in the next chapter. We show how a MZI can be modified to measure rates of rotation and, using the techniques developed in this chapter, determine the precision afforded by different initial states in this modified set-up.

Chapter 4

An introduction to gyroscopes

Gyroscopes are devices that can measure rotations relative to a fixed frame of reference. They were first invented over 150 years ago and since then have been developed extensively. They have proved particularly useful in inertial navigation systems where the current position of an object is determined relative to some fixed starting point without the use of any external landmarks. This is achieved by continually monitoring the object's acceleration and angular orientation using accelerometers and gyroscopes. Both of these devices must allow for precise measurements as small measurement errors soon translate to large position errors. Other potential uses of gyroscopes include detections of fluctuations in the rotation of the earth and in tests for general relativity.

A considerable portion of this thesis will be devoted to gyroscope schemes that are designed to precisely measure rates of rotation, ω. Each of these schemes employs a BEC of N atoms as its resource and relies on the principles of Mach-Zehnder interferometry to measure the rate of rotation through the detection of a phase shift that is directly related to ω. Consequently the precisions of these measurements can be calculated using the quantum Fisher information and, as will be shown later in the chapter, very much depend on the initial states used. In this chapter we first discuss the different types of gyroscopes that exist, describe the Sagnac effect, provide motivation for the use of a BEC as our resource and compare the precision

capabilities of current gyroscopes.

4.1 Different types of gyroscopes

There are two main types of gyroscope each of which will be described in this section. The first one we consider is the mechanical gyroscope and the second is the Sagnac effect gyroscope. The gyroscope schemes described in the latter chapters of this thesis all rely on the Sagnac effect and as such more emphasis is given to this type of gyroscope here.

4.1.1 The mechanical gyroscope

A mechanical gyroscope is essentially a mass that spins rapidly around its axis of symmetry. Due to the conservation of angular momentum the orientation of the device remains fixed. By mounting the gyroscope on a platform, in a ship for example, the angular displacement of the ship can be determined by measuring the angle between the platform and the gyroscope since the platform orientation will change yet the gyroscope's orientation will not.

In this thesis, however, we are primarily concerned with measuring rates of rotation and whilst this is possible with a mechanical gyroscope it is most effectively achieved using a Sagnac effect gyroscope as will now be explained.

4.1.2 The Sagnac effect gyroscope

Devices that employ the Sagnac effect are interferometric gyroscopes that rely on the same principles as Mach-Zehnder interferometry. In particular, rotation rates are determined by comparing the interference pattern of the device when there is no rotation present with the interference pattern when the rate of rotation is ω. This is analogous to a MZI where a difference in path length, for example, translates to a phase shift between the two interferometric paths. The size of the phase shift is determined by recombining the paths at a beam splitter and comparing

the interference pattern to the same interference pattern when the path lengths are equal.

A Sagnac gyroscope is therefore essentially achieved by rearranging the paths of a MZI into a ring geometry (see figure 4.1). We now explain the theory behind the Sagnac effect by considering a circular ring of radius R, however, the same results are found for any enclosed area, regardless of its shape. We also note that whilst the Sagnac effect was originally conceived for light it is equally applicable to massive particles.

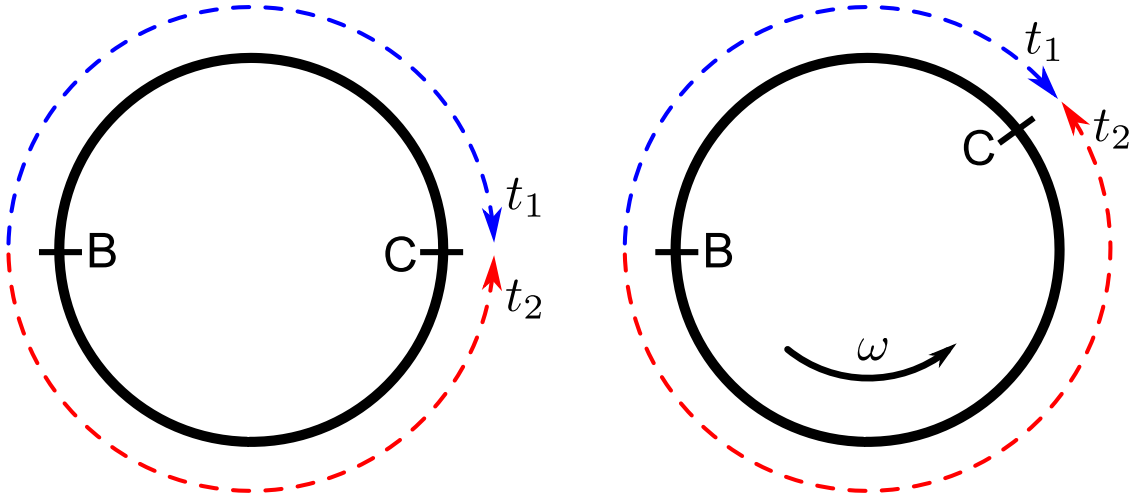

Figure 4.1: In a gyroscope a beam of particles is input to a 50:50 beam splitter at point B so the particles are put into a superposition of travelling in opposite directions around the ring. The paths are recombined at a second 50:50 beam splitter at point C and the resulting interference pattern is recorded. Left: The non-rotating case. Both paths are the same length and so particles on each path reach C at the same time, $t_1 = t_2$. Right: The gyroscope rotates at angular velocity ω meaning the particles on the lower path (particles moving in the same direction as the rotation) must travel further to reach C than in the non-rotating case whilst the particles on the upper path do not travel as far because C is moving towards them so $t_2 > t_1$.

To begin, particles are input to the gyroscope at point B (see figure 4.1) where they are split by a device such as a 50:50 beam splitter so that each particle is now in a superposition of moving in opposite directions around the ring. Particles exit the gyroscope at a second beam splitter (point C) placed exactly opposite the first beam splitter. If the gyroscope is not rotating the time required for a particle

travelling in either direction around the ring to reach point C will be the same due to symmetry. However, if the gyroscope is rotating with angular velocity ω about an axis that passes through the center of the ring and that is perpendicular to its plane, the time taken for the counter-propagating particles to reach point C will no longer be equal. Instead particles that are travelling in the opposite direction to the rotation will arrive at C in a shorter time than they did when the gyroscope was stationary. This is because point C is moving towards them, thereby shortening the distance they must travel. The time taken for these particles to reach C is

$$t_1 = \frac{\pi R}{v + \omega R} \tag{4.1}$$

where v is the velocity of the particles. For those particles moving in the same direction as the rotation the time taken to reach C is longer than in the stationary case since the distance the particles must travel to arrive at C is lengthened. In this case the time taken to reach point C is given by

$$t_2 = \frac{\pi R}{v - \omega R}. \tag{4.2}$$

This means particles travelling in opposite directions around the ring exit the gyroscope at different times. The time difference is

$$\Delta t = t_2 - t_1 = \frac{2\omega A}{v^2 - \omega^2 R^2} \tag{4.3}$$

where $A = \pi R^2$ is the area enclosed by the ring. Considering small rotation rates $\omega R \ll v$ and using the relationship between phase and time, $\phi = f_\omega t$ (where f_ω is the angular frequency of the particles), the phase difference established between the counter-rotating paths is

$$\phi = \frac{4\pi\omega A}{\lambda v} \tag{4.4}$$

where λ is the wavelength of the particles. From this equation we see that by measuring the size of the phase shift ω can be determined directly. We note that

for massive particles $\lambda_{\mathrm{dB}} = h/(mv)$ (here h is Planck's constant and m the particle mass) meaning equation 4.4 is more commonly written as

$$\phi = \frac{2m\omega A}{\hbar}. \tag{4.5}$$

4.2 Atoms versus light

We now compare the size of the phase shift induced in light-based and atom-based gyroscopes. To allow a fair comparison we set ω and A to be the same for each system. The ratio of the two phase shifts is therefore

$$\frac{\phi_a}{\phi_l} = \frac{\lambda_l c}{\lambda_a v_a} = \frac{mc^2}{\hbar f_{\omega_l}} \tag{4.6}$$

where the subscripts a and l refer to the atomic and light systems respectively and c is the speed of light. We note also that this comparison is for equal particle fluxes. Immediately it is clear that, under these assumptions, the phase shift in the atom-based gyroscope is considerably larger than the phase shift induced in the light-based gyroscope and is therefore much easier to detect and measure. For example, the phase shift in a ceasium atom device is 6×10^{10} greater than the phase shift in a HeNe laser device [80].

Nevertheless, we note that the apparent advantage of atomic systems is often diminished by the much larger areas and particle fluxes that can currently be achieved in light-based devices. Eventually, however, these problems are likely to be overcome as experimental advances are made. It is therefore important to start developing atom-based gyroscopes now.

4.3 Why use a BEC?

For atom-based gyroscopes to be a viable alternative to the usual light-based devices we require strategies to manipulate the atoms in a similar way to which light is manipulated in optical gyroscopes, for example, we need to create superpositions of

particles travelling in opposite directions around an enclosed area. Furthermore, in order for the precision capabilities of atomic gyroscopes to beat those of their optical equivalents, we also require relatively large particle fluxes. For these reasons BECs are a promising candidate for atom gyroscopy. In particular, BECs in an optical lattice are ideal because, as previously mentioned, the dynamics of the system can be controlled to a high degree of accuracy simply by altering the intensity of the trapping light, something that is readily achievable in the laboratory. The high level of coherence present in BECs will also mean the interference pattern will have a high level of contrast thereby increasing fringe visibility.

BECs with 10^8 atoms can be produced in the laboratory and therefore provide the large particle fluxes required to achieve high levels of sensitivity. Loading the condensate into an optical lattice can give the required geometry and enclosed area necessary for the Sagnac effect. The first atomic gyroscope system we develop in this thesis uses a BEC loaded into an optical ring lattice. We consider the simplest case of a ring of three sites but the possibility of using more sites is discussed in the future work section of the thesis. The required superposition of particles travelling in opposite directions around the ring is created using beam splitting operations developed in Chapter 5. The interference pattern, from which the phase shift and hence rotation is determined, is created by recombining the two paths with inverse beam splitting operations, turning off the trapping potential and imaging the condensate.

The second scheme we present uses a continuous optical ring potential loaded with a BEC. In this case the required superposition is created by 'stirring' the atoms with an optical barrier which is produced using a blue detuned laser. This scheme has the added advantage that the atoms can occupy multiple momentum modes unlike in the first scheme where the number of momentum modes is limited to three since there are only three lattice sites. We show the effect of the multiple momentum modes is to increase the robustness of the system to the effects of particle loss.

4.4 Units of measurement

Rates of rotation are usually given in units of radians per second, rads^{-1}, yet gyroscope sensitivity most often has units of $\text{rads}^{-1}/\sqrt{\text{Hz}}$. This is the short term sensitivity of the gyroscope, that is, its ability to detect small rotations over a time interval of 1 second.

The usual units of rotation are divided by $\sqrt{\text{Hz}}$ because, as mentioned in Chapter 3, repeating an experiment ν times improves the sensitivity as $1/\sqrt{\nu}$. Since $\nu \propto \tau$, where τ is the total integration time, the sensitivity improves by a factor of $\sqrt{\tau}$ as τ increases. Dividing by $\sqrt{\text{Hz}}$ therefore normalises the result to give the sensitivity of the device in a 1 second integration time. This allows for easy comparison of the precision of devices that employ different mechanisms.

4.5 Progress to date

Since the Sagnac effect was first proposed to measure rates of rotation in 1913 [14] much progress has been made. In 1925, for example, Michelson successfully used the Sagnac effect to measure the rotation of the earth using a large optical interferometer [81]. Since then the sensitivity of optical gyroscopes has been drastically improved largely due to the larger enclosed areas that can be achieved using long optical fibers wound around a spool. These photonic devices are now widely used in inertial navigation systems on ships and planes.

It was not until 1988, however, that the first atom-based gyroscope was proposed [82] and not until 1991 that the first atomic device was built [83]. Since this first demonstration of an atom-based gyroscope much theoretical and experimental research has been undertaken to improve the sensitivity of these devices (for a selection of recent results see [84–87]). Now despite their smaller particle fluxes and enclosed areas, their sensitivities are comparable to those of their optical equivalents. To date the best recorded short term sensitivity of an atomic gyroscope is $6 \times 10^{-10}\text{rads}^{-1}/\sqrt{\text{Hz}}$ [80].

All these gyroscopic devices, however, employ unentangled initial states as their resource (they all input particles into just one of the two possible input ports of the interferometer scheme) and as a result their precisions cannot surpass the SQL. In the previous chapter we saw how by using quantum correlations between the particles the precision of a MZI could be dramatically improved. The same is true for the Sagnac interferometry schemes employed in gyroscopic devices [88]. From equation 4.5 we can write the uncertainty in the rotation measurement as

$$\Delta\omega = \frac{\hbar}{2mA}\Delta\phi. \tag{4.7}$$

As shown in Chapter 3 $\Delta\phi = 1/\sqrt{N}$ when the initial state is unentangled thereby giving an uncertainty in ω of

$$\Delta\omega = \frac{\hbar}{2mA\sqrt{N}}. \tag{4.8}$$

This is the precision scaling achieved by the gyroscope schemes mentioned thus far. There is, however, the potential to dramatically improve this scaling to

$$\Delta\omega = \frac{\hbar}{2mAN} \tag{4.9}$$

through the use of entangled initial states such as the NOON state. As in a linear MZI this is Heisenberg limited and is the ultimate precision that can be achieved by a Sagnac based gyroscope.

A detailed comparison of light-based and atom-based gyroscopes employing entangled and unentangled initial states has been given in reference [88]. Taking the typical particle flux of a light-based gyroscope to be 10^{16} photons/second and that of an atom-based device to be 10^{12} atoms/second the precision of the light-based device can be improved by a factor of 10^8 using entangled photons and in the same way that of the atom-based device can be improved by a factor of 10^6. Importantly using entangled atoms the precision of current light-based gyroscopes can be improved by

a factor of 10^{10}.

We see, therefore, that there is real motivation to develop gyroscopes that use entangled atomic states as their input. Two such schemes are proposed in this thesis, both of which employ a BEC as their resource. We extend our analysis to include the effects of particle loss from the gyroscopes.

We have now introduced almost all the tools necessary to develop these gyroscope schemes: we have looked at BEC theory and discussed what happens when a condensate is rotated, discussed the general precision capabilities of different initial states in a MZI and extended these precision scalings to a Sagnac gyroscope scheme. We must first, however, introduce one final tool that will be used to create the necessary superposition of BEC atoms flowing in opposite directions around a ring of lattice sites, that is, a multiport atomic beam splitter.

Chapter 5

Multiport atomic beam splitters

Beam splitters allow quantum states to be manipulated and, as we have shown, are a key component of precision measurement schemes such as the MZI and the Sagnac gyroscope. Their uses, however, extend well beyond precision measurement schemes as any device that can manipulate the entanglement of quantum states could prove invaluable in various quantum information processing schemes. Beam splitters are most often thought of as having two input and two output ports, however, their multiport equivalents have been studied extensively. Indeed, in recent years, much progress has been made towards their experimental implementation and now devices with up to 32 input and output ports are readily available in optical fibre set-ups [50]. The potential of these multiport devices are extensive with the improved precision of phase measurements proving to be one of their most promising applications [89, 90].

Here we propose an experimentally accessible scheme to create multiport atomic beam splitters. We use a BEC loaded into an optical ring lattice and each lattice site corresponds to an input port. Consequently our multiport splitting devices should prove extremely useful in ultra-precise rotation measurement schemes where the entangled states need to be in a ring geometry.

5.1 Introduction

Considerable progress has been made over the past decade towards implementing and understanding multiport devices. Theoretical work has devised schemes to create multiport devices with any number of input and output ports [91] and has analysed some of their useful properties [50, 89, 90, 92–94]. Experimental work using photons has demonstrated the operation of beam splitters with three inputs and outputs ('tritters') as well as four inputs and outputs ('quarters') by clever arrangements of ordinary two-port beam splitters and phase plates [95]. Similar devices have also been proposed [50] and implemented [96] in systems of bundled optical fibres.

These devices become more powerful as the number of input and output ports is increased. However, for larger systems, the experimental configuration required rapidly becomes labyrinthine. In general, for a device with S inputs and S outputs, $S(S-1)/2$ two-port beam splitters and $S(S+1)/2$ phase shifts would be required, i.e. a total of S^2 optical elements [91]. The complexity of implementation is perhaps even more problematic for atomic systems where beam splitting is a dynamic process typically involving the raising and lowering of potential barriers. In this case, a multiport beam splitter would involve a complex sequence of operations and the experimenter would need to be able to address lattice sites individually – an issue that has caused considerable problems when trying to use optical lattices for quantum information processing.

In this chapter, we demonstrate a scheme for implementing atomic multiport devices that goes someway towards overcoming these problems. In particular, it requires no additional equipment or steps than a standard two-port atomic beam splitter. We begin by developing the theoretical scheme for an atomic tritter and follow with its extension to a device with a general number of ports. An interesting asymmetry is found in the behaviour of devices with an odd or even number of input ports. Finally, we take into account various practical considerations and see that our scheme is likely to be limited to splitters with about five input (and output) ports.

5.2 The scheme

The physical system we consider consists of an optical lattice of S sites arranged in a 'ring' configuration with atoms trapped at the potential minima (see figure 5.1). As shown in Chapter 2 such a system can be described by the Bose-Hubbard model with Hamiltonian

$$\frac{H}{\hbar} = \sum_{j=0}^{S-1} \epsilon_j a_j^\dagger a_j - J \sum_{j=0}^{S-1} \left(a_j^\dagger a_{j+1} + a_{j+1}^\dagger a_j \right) + V \sum_{j=0}^{S-1} a_j^{\dagger 2} a_j^2 \tag{5.1}$$

where a_j is the annihilation operator for an atom at site j and the ring geometry means that $a_S = a_0$. The parameters J and V are the tunnelling and interaction strengths respectively (note here we have used $V = U/2$), and ϵ_j accounts for the energy off-set of site j. Throughout this chapter we take the zero point energy to be the same for each site and so can ignore these energy off-set terms. Here we have divided by $\hbar$ to convert the units of J, V and ϵ into frequencies which will allow for easy comparison with existing experiments later in the chapter. Each of the lattice sites corresponds to an input port of our multiport beam splitter.

In order to implement the beam splitting procedure we begin with large potential barriers between the sites so we can ignore tunnelling. The first step is to rapidly reduce the potential barriers between the sites in such a way that the sites still remain separate but are strongly coupled due to tunnelling. We want to do this rapidly with respect to the tunnelling time, but slowly with respect to the energies associated with excited states to ensure our system remains in the ground state. Experiments have already successfully demonstrated this separation of timescales by ramping the optical intensity on a timescale of about 20ms [97].

The tunnelling between wells now dominates over the interactions and the Hamiltonian of equation 5.1 can be written in the simple form,

$$\frac{H}{\hbar} = -J \sum_{j=0}^{S-1} \left(a_j^\dagger a_{j+1} + a_{j+1}^\dagger a_j \right). \tag{5.2}$$

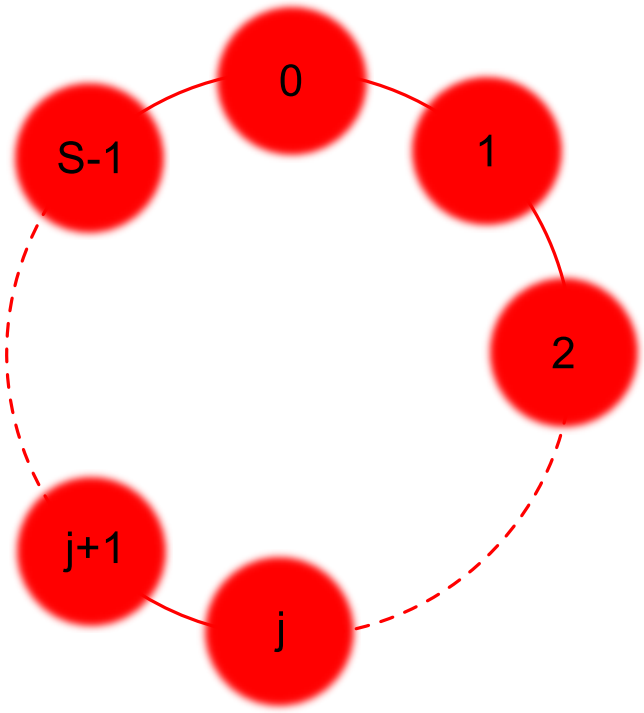

Figure 5.1: Ring configuration of S sites in an optical lattice. The lines denote tunnelling between sites.

Of course this makes the approximation that the interaction energy will be negligible compared with the tunnelling energy. In practice, the interactions will not be strictly zero. However, they can be made very small with respect to J by, for example, making use of Feshbach resonances to tune the scattering lengths [98]. For now, it is helpful to consider the case where we can ignore V. We consider the effects of this assumption in section 5.5.

5.2.1 Example: The Tritter

To introduce the exact workings of the scheme we describe in detail the case of $S = 3$. A similar configuration has been achieved experimentally by trapping atomic Bose-Einstein condensates (BECs) in the optical potential created by the diffraction of a laser beam by a liquid crystal spatial light modulator [36]. This modulator allows arbitrary three-dimensional trapping potentials to be achieved, which have the added advantage of being able to be varied smoothly with time. Another promis-

ing possibility for creating the ring potential, is to interfere a Laguerre-Gaussian (LG) laser beam with a plane wave co-propagating along the z-direction [99]. By retro-reflecting this combined beam, a standing wave can be formed that consists of a stacked array of disk shaped traps along the z-direction. By controlling the tunnelling between the disks and making it much smaller than the corresponding tunnelling within each ring, one can implement an array of effective 1D ring lattices. In both these cases, the rate of tunnelling between the sites in a ring can be controlled simply by adjusting the intensity of the trapping laser light.

The Hamiltonian describing this three site system is

$$\frac{H}{\hbar} = -J\left(a_0^\dagger a_1 + a_1^\dagger a_2 + a_2^\dagger a_0\right) + \text{h.c.}. \tag{5.3}$$

As was shown in Chapter 2 this Hamiltonian is diagonalised in the flow basis

$$\begin{pmatrix} \alpha_0 \\ \alpha_1 \\ \alpha_2 \end{pmatrix} = \frac{1}{\sqrt{3}} \begin{pmatrix} 1 & 1 & 1 \\ 1 & e^{i2\pi/3} & e^{-i2\pi/3} \\ 1 & e^{-i2\pi/3} & e^{i2\pi/3} \end{pmatrix} \begin{pmatrix} a_0 \\ a_1 \\ a_2 \end{pmatrix} \equiv U \begin{pmatrix} a_0 \\ a_1 \\ a_2 \end{pmatrix} \tag{5.4}$$

to give

$$\frac{H}{\hbar} = -J\left[2\alpha_0^\dagger\alpha_0 - \alpha_1^\dagger\alpha_1 - \alpha_2^\dagger\alpha_2\right] \tag{5.5}$$

where α_0 destroys an atom with zero flow, α_1 destroys an atom with one unit of clockwise flow and α_2 destroys an atom with one unit of anticlockwise flow. If the system is allowed to evolve for time, t, the α_0 mode acquires a phase of $-2Jt$, while the α_1 and α_2 modes each acquire a phase of Jt. If the barriers are then raised on a similar timescale to their lowering (i.e. quickly with respect to the tunnelling time, but slowly with respect to the energies associated with excited states), the atoms are 'frozen' in the lattice sites a_0, a_1, and a_2. The overall output operators $\{A_0, A_1, A_2\}$

are given by

$$\begin{pmatrix} A_0 \\ A_1 \\ A_2 \end{pmatrix} = U^{-1} \begin{pmatrix} e^{i2Jt} & 0 & 0 \\ 0 & e^{-iJt} & 0 \\ 0 & 0 & e^{-iJt} \end{pmatrix} U \begin{pmatrix} a_0 \\ a_1 \\ a_2 \end{pmatrix} \tag{5.6}$$

$$= \frac{1}{3} \begin{pmatrix} \Omega_0 & \Omega_1 & \Omega_1 \\ \Omega_1 & \Omega_0 & \Omega_1 \\ \Omega_1 & \Omega_1 & \Omega_0 \end{pmatrix} \begin{pmatrix} a_0 \\ a_1 \\ a_2 \end{pmatrix} \equiv R_3 \begin{pmatrix} a_0 \\ a_1 \\ a_2 \end{pmatrix} \tag{5.7}$$

where $\Omega_0 = e^{i2Jt} + 2e^{-iJt}$, $\Omega_1 = e^{i2Jt} - e^{-iJt}$, and for later reference, we have defined the overall operation as R_3. We see that the output modes are identical to the input modes when $t = 0$, as we would expect. For a balanced tritter, we need the output modes to be an equal superposition of the input modes, i.e. $|\Omega_0| = |\Omega_1|$. This occurs when $t = 2\pi/(9J)$, for which value we have (ignoring an irrelevant overall phase),

$$R_3 = \frac{1}{\sqrt{3}} \begin{pmatrix} 1 & e^{i2\pi/3} & e^{i2\pi/3} \\ e^{i2\pi/3} & 1 & e^{i2\pi/3} \\ e^{i2\pi/3} & e^{i2\pi/3} & 1 \end{pmatrix}. \tag{5.8}$$

To summarise, the steps in implementing a balanced tritter are,

1. Rapidly reduce the potential barriers separating the lattice sites.

2. Allow the system to evolve for time $t = 2\pi/(9J)$.

3. Rapidly raise the potential barriers.

Each output is an equally-weighted superposition of all the inputs. One may notice, however, that the phases between terms in these outputs are different from those commonly quoted for a tritter in the literature (e.g. in [93, 95]). For many purposes, this does not matter. For example, we can take the output modes of a 50:50 beam splitter to be either $\{(a_0+a_1)/\sqrt{2}, (a_0-a_1)\sqrt{2}\}$ or $\{(a_0+ia_1)/\sqrt{2}, (ia_0+a_1)\sqrt{2}\}$ without fundamentally changing the results. If, however, we do require a particular

form of the phases for the output modes, this can always be achieved by imprinting phases on individual lattice sites before and after the lowering and raising of the barrier. In practice this could be achieved by applying energy off-sets, ϵ_j, to the lattice sites for some fixed time. Indeed, in Chapter 6 the phases of our tritter operation are modified using this method.

This procedure not only achieves the goal of a multiport beam splitter for atoms, but is much simpler than schemes that combine phase shifts with a complicated network of two-port beam splitters. Our scheme only requires a lowering and raising of the lattice potential and, importantly, requires no more operational effort than an ordinary two-port beam splitter for atoms [100]. This bodes well for the possibility of scaling the scheme up to larger systems.

5.3 Larger devices

We now extend this scheme to the general case of a lattice ring with an arbitrary number of sites (in section 5.5 we will determine up to what values of S this scheme is valid experimentally). Following the same procedure as for the tritter we lower the potential barriers so that tunnelling between the wells dominates over the interactions and the Hamiltonian describing the system is given by equation 5.2. As for the three site case this can be written in the diagonalised basis as

$$\frac{H}{\hbar} = -2J \sum_{k=0}^{S-1} \cos\left(\frac{2\pi k}{S}\right) \alpha_k^\dagger \alpha_k \tag{5.9}$$

where

$$\alpha_k = \frac{1}{\sqrt{S}} \sum_{j=0}^{S-1} e^{i2\pi jk/S} a_j. \tag{5.10}$$

The system is now allowed to evolve for time t during which the S modes each acquire a phase of $-2\cos\left(\frac{2\pi k}{S}\right) Jt$. The potential barriers are then quickly raised

and the output is given by,

$$\begin{pmatrix} A_0 \\ A_1 \\ \vdots \\ A_{S-1} \end{pmatrix} = U^{-1} \begin{pmatrix} e^{i2Jt} & 0 & 0\dots & 0 \\ 0 & e^{i2\cos\left(\frac{2\pi}{S}\right)Jt} & 0\dots & 0 \\ \vdots & \vdots & \ddots & \vdots \\ 0 & 0 & \dots & e^{i2\cos\left(\frac{2\pi(S-1)}{S}\right)Jt} \end{pmatrix} U \begin{pmatrix} a_0 \\ a_1 \\ \vdots \\ a_{S-1} \end{pmatrix}$$

$$= \begin{pmatrix} \Omega_0 & \Omega_1 & \dots & \Omega_{S-1} \\ \Omega_{S-1} & \Omega_0 & \dots & \Omega_{S-2} \\ \vdots & \vdots & \ddots & \vdots \\ \Omega_1 & \Omega_2 & \dots & \Omega_0 \end{pmatrix} \begin{pmatrix} a_0 \\ a_1 \\ \vdots \\ a_{S-1} \end{pmatrix} \equiv R_S \begin{pmatrix} a_0 \\ a_1 \\ \vdots \\ a_{S-1} \end{pmatrix} \tag{5.11}$$

where the unitary matrix is given by $U_{kj} = \frac{1}{\sqrt{S}} e^{i2\pi jk/S}$ and

$$\Omega_x = S^{-1} \sum_{n=0}^{S-1} \exp(i2Jt\cos(2\pi n/S) + i2\pi nx/S). \tag{5.12}$$

As before, the condition for a balanced multiport splitter is that each output is an equally weighted superposition of all the inputs, i.e. $|\Omega_0| = |\Omega_1| = \ldots = |\Omega_{S-1}|$. We now wish to see if our procedure can achieve this for a general S ignoring, for now, factors that may limit its experimental feasibility.

5.3.1 Producing a balanced splitter

We can determine if a balanced splitter can be achieved for a device with S sites by plotting the elements of R_S as a function of Jt and checking whether there are times for which $|\Omega_0| = |\Omega_1| = \ldots = |\Omega_{S-1}|$. Figure 5.2 shows these plots for $S = 3, 4, 5$ and 6 in the time range $t = 0$ to $2\pi/J$. We see that all the Ω intersect at $t = 2\pi/(9J)$ for $S = 3$ and at $t = \pi/(4J)$ for $S = 4$, but there is no exact crossing for $S = 5$ and 6 in this range (or indeed for larger values of S). However, looking in the time range $t = 0$ to $1000/J$ we find for systems with odd values of S, up to $S = 9$, there is an intersection of all the Ω to within an error of 1%. It is convenient to define a

measure, χ, of how good the intersection is, as

$$\chi = \sum_{x=0}^{S-1} \left(|\Omega_x| - \frac{1}{\sqrt{S}} \right)^2 . \tag{5.13}$$

This is simply the sum of the squares of the deviation of each value of $|\Omega|$ from its ideal value (i.e $1/\sqrt{S}$) – as discussed above, we are not concerned by the phase of the Ω values. If, on average, each value of $|\Omega|$ differs from $1/\sqrt{S}$ by 1%, χ has a value of 10^{-4}. We will use this value (i.e. $\chi \lesssim 10^{-4}$) as a useful criterion for when a balanced splitter has been achieved.

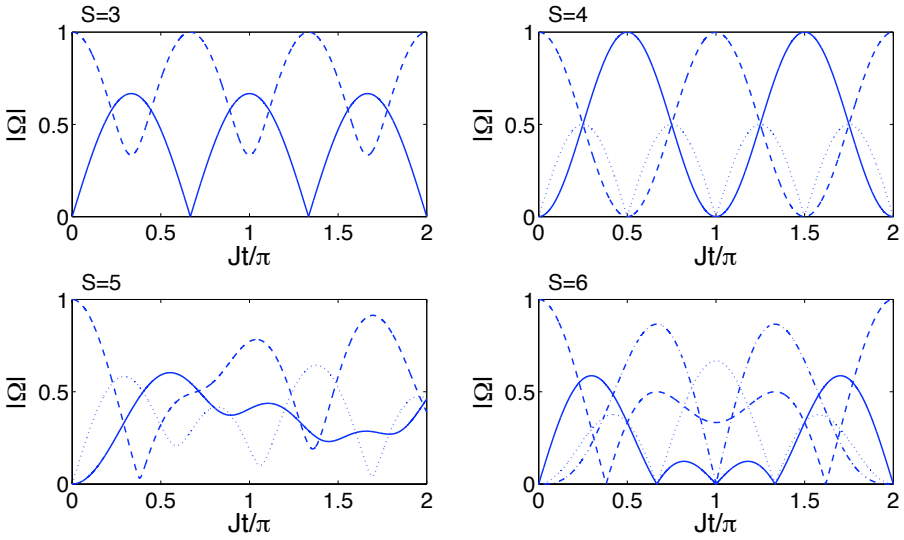

Figure 5.2: These plots show how the $|\Omega|$ vary with time for multiport devices with $S = 3, 4, 5$ and 6 from top left to bottom right respectively. We see that for $S = 3$ the $|\Omega|$ intersect at $t = 2\pi/(9J)$ and for $S = 4$ they intersect at $t = \pi/(4J)$. For $S = 5$ and 6 there is no intersection of all the $|\Omega|$ in the time range shown here ($t = 0$ to $2\pi/J$).

Using this criterion, we find balanced splitters for $S = 5, 7$ and 9 at evolution times $t \approx 5.2\pi/J$, $88\pi/J$ and $177\pi/J$ respectively. The intersection of the Ω values for $S = 5$ at $t \approx 5.2\pi/J$ is shown in figure 5.3. The time required to achieve a balanced splitting device increases with increasing S as there are more values of Ω to match. Interestingly, no intersections for which $\chi \lesssim 10^{-4}$ are achieved for even values of S in this time range. We will discuss possible reasons for this in the next

section. We should note that while we do not see intersections that satisfy $\chi \lesssim 10^{-4}$ for even values of S in the time range used (or for S odd greater than 9), this does not rule out the possibility at a later time. One exception is $S = 6$ because all the values of $|\Omega|$ in this case repeat with a period of 2π and, since there is no intersection during this period, there will never be one. The same may be true for some other, larger S. However, so long as χ for a given S is not periodic in time, if we wait long enough the balanced splitting criterion should be able to be achieved. Of course, this may not always be experimentally expedient and could be longer than the coherence time of the system.

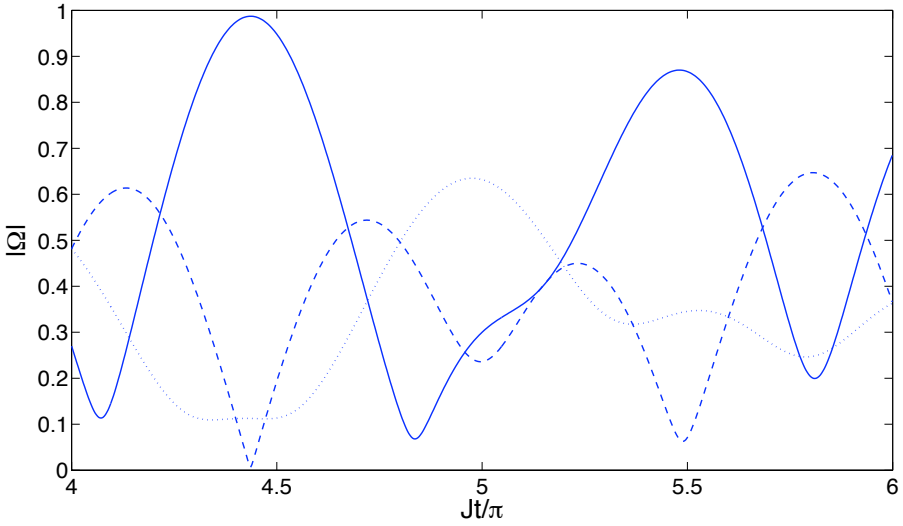

Figure 5.3: Using $\chi \lesssim 10^{-4}$ as our defining criterion for when a balanced splitter is achieved we find a five site splitter is produced at $t \approx 5.2\pi/J$. The near intersection of all the $|\Omega|$ at this time can be seen here.

To summarise, devices with even and odd numbers of sites are potentially both capable of producing balanced multiport devices. However, the even cases usually require a much longer evolution time than the odd ones. We now investigate the reasons for this difference in behaviour.

5.3.2 The difference between S even and S odd

In order to understand the difference in behaviour between systems with odd and even numbers of lattice sites we compare the Ω_x of both systems. It is possible to show that for the case of even values of S

$$\Omega_x = e^{i\pi x/2}\Lambda(S, J, t, x) \tag{5.14}$$

where $\Lambda(S, J, t, x)$ is some real-valued function that depends on S, J, t and x. A proof of equation 5.14 is given in Appendix A. We see that the phase difference between Ω_x and $\Omega_{x\pm1}$ is always $\pm\pi/2$ which, in turn, means the phase difference between adjacent sites is always $\pm\pi/2$. In Chapter 2 we showed that the rate at which atoms flow is given by $v = (\hbar/m)\nabla\theta$ where $\nabla\theta$ is the phase gradient. Since the phase varies by a fixed amount between sites we therefore see that the atoms must flow at a fixed speed.

In contrast for odd values of S the Ω_x cannot be written as in equation 5.14 as the phase of each Ω_x varies continuously with time. The phase difference between sites, and hence the velocity of flow, are therefore not constrained in the same way as for even S. The additional constraint imposed by the symmetry of the even case on the allowed flow rates is one reason why it is more difficult for devices with an even number of sites to achieve a state where their outputs are in an equal superposition of their input modes [1].

Another difference between the cases of even and odd numbers of sites is seen when we look at the number of distinct elements required to compose the operators R_S. Instead of the number of different Ω equalling the number of sites, S, there are $(S+1)/2$ different Ωs for odd S and $(S+2)/2$ different Ωs for even S (see Appendix A for a proof of this). This is due to the symmetry of the system and it means for even S there are more values of Ω to match to make a balanced splitter. Again, this

[1] This argument suggests that it should be difficult to achieve a balanced splitter for $S = 4$, but we have seen that this is not the case. This is because the constraint that adjacent sites have a phase difference of $\pm\pi/2$ happens to be precisely the phase difference required for the $S = 4$ case to work.

difference supports our observation that it is more difficult for systems with an even number of sites to produce a balanced splitter.

5.4 Inverse transforms and unbalanced splitters

Now that we have explained the basic operation of multiport beam splitters, we would like to consider how they can be combined to create useful quantum devices. One simple, yet important, such device that has, and will be used throughout the thesis, is an interferometer such as the Mach-Zehnder interferometer introduced in Chapter 3. In general, an interferometer consists of a beam splitter, a phase shift, and then an inverse beam splitter. However, for two-path interferometry, the inverse beam splitter is most often replaced with a normal beam splitter (see figure 3.1). The reason this works is that a 50:50 beam splitter can be thought of as a $\sqrt{\text{NOT}}$ operation. We can see this because a Mach-Zehnder interferometer with no phase difference between the two paths (i.e. two 50:50 beam splitters in succession) gives an output state that is the same as the input but with the ports swapped, i.e. a NOT operation. So two beam splitters in succession will return us to the original state so long as we make a trivial swap of the labels of the output ports. For multipath interferometers, however, the same is not true: we cannot simply replace the inverse splitter with an ordinary splitter and relabel the modes. So, to be able to implement a multipath interferometer, we need to be able to implement inverse multiport devices.

It turns out that *three* successive applications of a tritter, R_3^3 is equivalent to the identity and leaves the original input state unchanged. This can easily be verified using equation 5.8. This means that the inverse operation of a tritter is simply R_3^2 or, equivalently, a tritter operation where the state is allowed to evolve for twice as long with the barriers lowered (i.e. $t = 4\pi/(9J)$ rather than $t = 2\pi/(9J)$). The inverse operation can, therefore, be implemented just as easily as the original transform.

More generally, the inverse operation of a device with S sites is simply $R_S^{(S-1)}$.

We have numerically checked this for $S = 4, 5, 7$, and 9 [2] by calculating how close $R_S R_S^{(S-1)} = R_S^S$ is to the identity operator. We do this by summing up the modulus squares of the leading diagonal of R_S^S and dividing by S as this effectively gives the fidelity of the output state relative to the input (averaged over all input ports). The values we found for this measure for $S = 4, 5, 7$ and 9 were $1, 0.96, 0.91$ and 0.75 respectively. We see that the inverse splitter is degraded as S is increased. This is not surprising because, if our timing does not give an exactly balanced splitter, when we multiply this time by $(S - 1)$ to give the time of the inverse splitter the imperfection is multiplied. Of course, there may be earlier times that give a good approximation to the inverse splitters and this is possible area for future research.

So far, we have only discussed splitters that have balanced outputs and are therefore the multiport generalisations of 50:50 two-port beam splitters. For many applications we may not want the outputs to be balanced. For example, we may want a device that coherently skims off only a small fraction of an input state and redistributes it between the output modes. Our scheme holds great potential for producing such devices simply by changing the value of the evolution time. Since the coherent amplitude in each output mode depends on t, this allows us to obtain multiport splitters with different 'reflectivities'. All this can be achieved without changing the experimental set-up – only the timings of the steps. It is important to note, however, that not all unbalanced outputs can be achieved by this method as not all the values of Ω are independent.

Multiport splitters promise a broad range of future applications. One such application is in the field of quantum metrology where spreading particles over many paths rather than just two may prove to allow for more precise and/or more robust phase measurements. The potential of multipath interferometers for making ultra-precise measurements is introduced in Chapter 8 and again in the future work section of the thesis. A further use is demonstrated in Chapter 6 where the tritter developed in this chapter is used in an atomic gyroscope scheme.

[2] $S = 6$ and $S = 8$ were not considered due to the difficulty in obtaining a splitter in these cases, as discussed above.

5.5 Practical limitations to the number of ports

So far in discussing the general scheme for implementing an atomic multiport device we have neglected a number of important physical processes. This has allowed us to treat an idealised case and has been useful for understanding its key features. However, in reality, these processes must be accounted for and will limit the applicability of the scheme. In this section we highlight the key practical limitations to this scheme and assess their impact.

5.5.1 Intensity fluctuations

Since the time for which the barriers must be lowered depends on the tunnelling rate, any uncertainty in J will introduce imperfections into the scheme. This may concern some readers since it is well known that J depends exponentially on the intensity of the trapping light which is subject to fluctuations. However, just because J depends exponentially on the intensity does not mean that small fluctuations in the intensity will result in large fluctuations in the tunnelling rate. Indeed the exponential function varies only linearly for exponents close to zero, and this is the regime in which this scheme operates. We can check this using an approximation for J found in [101],

$$\hbar J \approx \frac{E_R}{2} \exp\left(\frac{-\pi^2}{4}\sqrt{\frac{V_0}{E_R}}\right)\left[\sqrt{\frac{V_0}{E_R}} + \left(\sqrt{\frac{V_0}{E_R}}\right)^3\right] \tag{5.15}$$

where E_R is the atomic recoil energy, V_0 is the potential depth and $\hbar = 1$ in [101]. To ensure we are in the strong coupling regime we take $V_0 = 2E_R$, a configuration that has been achieved experimentally [102]. For a small fractional fluctuation, δ in the exponent due, for example, to intensity fluctuations in the trapping laser, this can be rewritten as

$$\tilde{J} \approx \frac{3E_R}{\hbar\sqrt{2}} \exp\left(\frac{-\pi^2}{2\sqrt{2}}(1+\delta)\right) = J \exp\left(\frac{-\pi^2}{2\sqrt{2}}\delta\right). \tag{5.16}$$

Intensity fluctuations can be stabilised to around 0.1% [103], i.e. $\delta = 0.001$, which gives $\tilde{J} \approx 0.9965J$. So the uncertainty in the tunnelling rate due to intensity fluctuations is modest and unlikely to be the major limitation to this scheme.

5.5.2 Condensate lifetime

Another potential limiting factor is how long the system must be allowed to evolve to produce the balanced splitters since this may be longer than the lifetime of the condensate. In section 5.3 we showed that the evolution times increased with S as expected since as S increases there are more different Ω to match. Figure 5.4 shows the value of Jt required to produce balanced splitters for $S = 3, 4, 5, 7$ and 9 and we see that in this range Jt scales as approximately the seventh power of S. This is quite a prohibitive scaling and in order to determine what values of S are feasible, we need to compare the evolution time with the lifetime of the condensate.

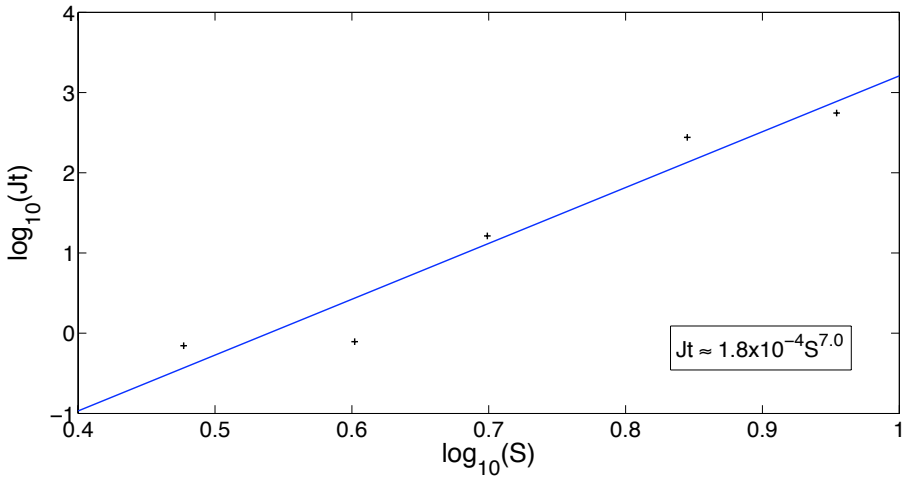

Figure 5.4: The crosses represent the Jt required to produce a balanced splitter for different S. The line is intended to find an approximate scaling of Jt with S. We find Jt roughly scales with S as $1.8 \times 10^{-4} S^{7.0}$.

Condensate lifetimes of about 10s have been measured [67] and oscillation periods of 40ms have been observed between wells in bosonic Josephson junctions [104], giving $J \sim 80\text{s}^{-1}$. Together these give an estimate of a typical maximum value of $Jt \approx 800$. For $S = 3, 4, 5, 7$ and 9 the largest value of Jt is 177π which is comfortably

below 800. Therefore, the times required to produce balanced splitters with up to nine sites should all be experimentally achievable. Using the scaling of Jt with S above, for $S = 11$, $Jt > 800$ suggesting $S = 9$ is the maximum number of sites the evolution times allow.

We note, however, that it is most likely that the splitters will be used in conjunction with their inverses to form devices such as Mach-Zehnder interferometers. The total Jt required is therefore S times as long as those shown in figure 5.4. For $S = 3, 4$ and 5 the total Jt still lies comfortably below 800. For $S = 7$ and 9, however, the total Jt required to produce a device consisting of the splitter and its inverse exceeds the maximum allowed value of 800. Consequently we find, for most practical purposes, our splitting devices will be limited to $S = 5$ sites.

5.5.3 Interactions

Up until now we have neglected the interactions between atoms by setting $V = 0$. We shall now consider how non-zero interactions limit our scheme. Taking them into account the Hamiltonian describing the system is

$$\frac{H}{\hbar} = -J \sum_{j=0}^{S-1} \left(a_j^\dagger a_{j+1} + a_{j+1}^\dagger a_j \right) + V \sum_{j=0}^{S-1} a_j^{\dagger 2} a_j^2. \tag{5.17}$$

First, we shall consider the effect of these interactions on our tritter for different numbers of atoms. We will then determine the effect of interactions for different values of S.

We measure the effect of interactions on the three site system by comparing the outputs of an interferometer, composed of a tritter and an inverse tritter, with and without the interactions taken into account. We chose to include the inverse tritter because, as previously mentioned, one of the greatest uses of these splitting devices is in an interferometer set-up which requires the application of a splitter followed by its inverse. For the purposes of our numerical calculations, we will consider the specific initial state $|N, 0, 0\rangle$ where the terms in the kets correspond to the number of atoms on sites 0, 1 and 2 respectively. Figure 5.5 shows how the fidelity between the

output states with and without the interactions varies as a function of interaction strength for different numbers of particles, N. As we would expect, the fidelity is unity when there are no interactions regardless of the value of N and the effects of the interactions become more significant as N is increased.

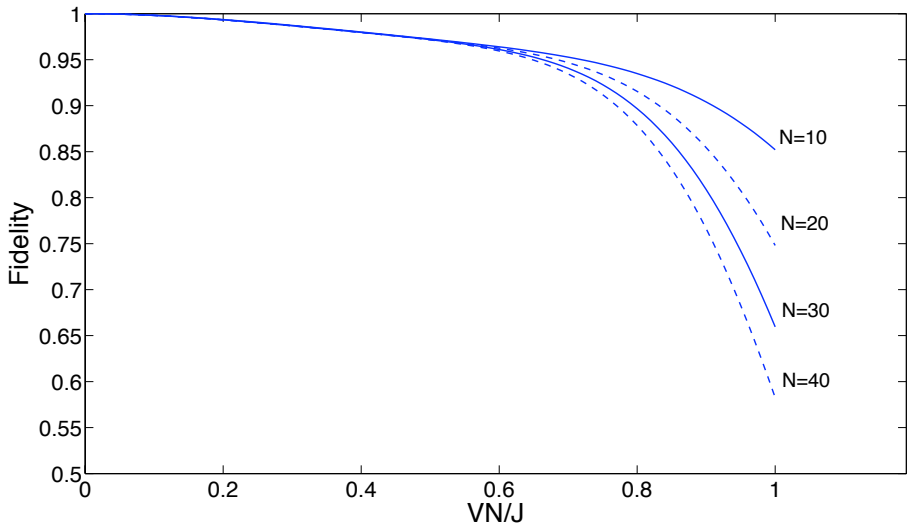

Figure 5.5: The fidelity of the output state of a three site interferometer with interactions, calculated from the overlap with the output when there are no interactions, plotted over the range $VN/J = 0$ to 1 for different numbers of atoms.

To determine an approximate scaling of the interactions with N we find the value of VN/J required to give a fidelity of 0.95 for different values of N. From this we determine the relationship between the number of input atoms and VN/J at this critical fidelity to be

$$\left(\frac{VN}{J}\right)_{F=0.95} \approx 0.85\ N^{-0.07} \tag{5.18}$$

which is shown in figure 5.6. This relationship means the effect of the interactions, V/J, on the system scales with N as $0.85N^{-1.07}$. This is an approximately linear scaling and so the effects of interactions in the system are not too destructive. It means we require VN/J to be of the order of 0.85 to achieve a fidelity of 0.95. To determine an experimental order of magnitude for V/J we use the approximations

of reference [101],

$$V \approx \frac{2a_s V_0^{\frac{3}{4}} E_R^{\frac{1}{4}}}{\hbar(\sqrt{\lambda D})} \tag{5.19}$$

$$J \approx \frac{E_R}{2\hbar} \exp\left(-\left(\frac{\pi^2}{4}\right)\sqrt{\frac{V_0}{E_R}}\right)\left(\sqrt{\frac{V_0}{E_R}} + \left(\sqrt{\frac{V_0}{E_R}}\right)^3\right) \tag{5.20}$$

where a_s is the scattering length, V_0 the barrier height, E_R the recoil energy, λ the wavelength of the lattice light and D the transverse width of the lattice sites. Feshbach resonances can tune a_s to values smaller than the Bohr radius for some BECs [105] and in the high coupling regime barrier heights of order $V_0 = 2E_R$ have been demonstrated [102]. Using light of wavelength $\lambda = D = 10\mu$m and ^{87}Rb atoms, interactions can therefore be tuned to $V \sim 10^{-3}$Hz and $J \sim 10$Hz in this regime giving $V/J \sim 10^{-4}$. This system is therefore limited to $N \sim 10^4$.

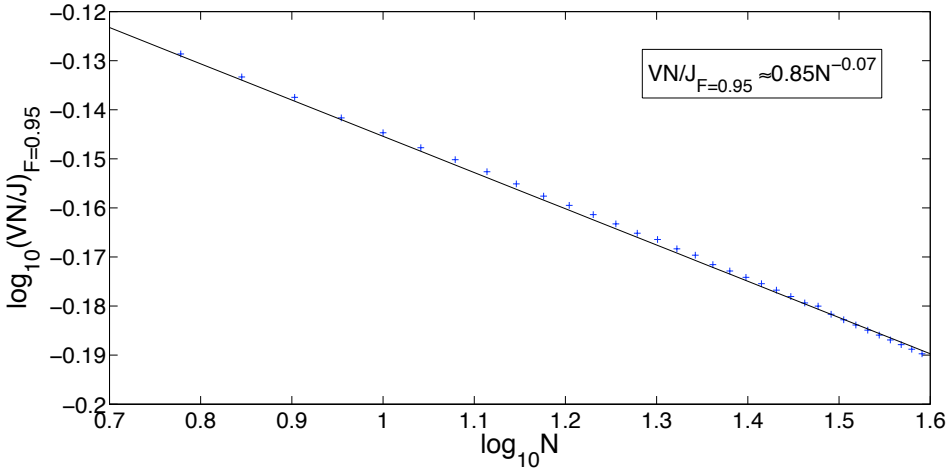

Figure 5.6: The correlation between VN/J at a critical fidelity of $F = 0.95$ and the number of atoms for a three site interferometer. The crosses are numerically calculated data points for values of N up to $N = 40$. The solid curve is a line of best fit intended to find the scaling. The approximate scaling is, $(VN/J)_{F=0.95} \sim 0.85N^{-0.07}$.

Things are less promising, however, when we consider the effects of interactions in interferometers with more sites. Determining V/J at the critical fidelity of 0.95 for a fixed number of atoms ($N = 5$) for $S = 3, 4, 5, 7$ and 9 allows us to see how interaction effects scale in this range of S. The results are shown in figure 5.7. We see that the V/J that allows us to achieve a fidelity of at least 0.95 decreases rapidly with S.

For $S = 7$, we require $V/J \sim 10^{-4}$, which is at the limit of what is experimentally achievable. Interactions therefore appear to limit the current applicability of our scheme to about five sites.

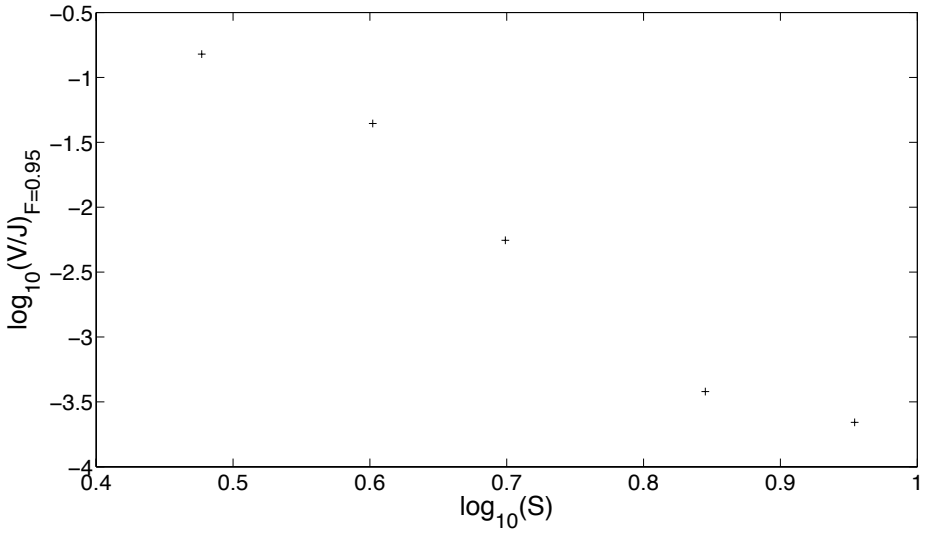

Figure 5.7: Plot of V/J at a critical fidelity of 0.95 as a function of S for $N = 5$. We see V/J decreases rapidly as S increases. For $S = 7$ the interaction strength required to achieve a fidelity of at least 0.95 is $V/J \sim 10^{-4}$. Such a value is likely to be experimentally challenging and so we take $S = 5$ as the maximum number of sites allowed when interactions are accounted for.

Since both the condensate lifetime and the atomic interactions have been shown to limit the experimental feasibility of our multisite interferometer schemes to five sites, in the remainder of this section we only consider the effects of the practical limitations on systems with $S = 3, 4$ and 5.

5.5.4 Timing errors

So far we have made the simplifying assumption that we can exactly measure the time the barriers are lowered for. We will now investigate how sensitive the scheme is to inaccuracies in this timing for different numbers of atoms for $S = 3, 4$ and 5. We first consider a three site system and as before we determine the effects of errors on the interferometer set-up, i.e. a tritter followed by its inverse. To determine the effect of an absolute time error, ϵ, we calculate the fidelity between the outputs of

the interferometer when $Jt = S\tau$ and when $Jt = S\tau + \epsilon$, where τ is the Jt required to produce the balanced splitter quoted in section 5.3, for the particular input state $|N, 0, 0\rangle$. As with the interactions, we determine how the fidelity scales with N by measuring ϵ at a critical fidelity of 0.95 for different values of N. These results are shown in figure 5.8 and we see that the relationship between ϵ at the critical fidelity and the number of atoms is given by,

$$\epsilon_{F=0.95} \approx 0.16 N^{-0.50}. \tag{5.21}$$

The maximum time error that still allows us to achieve a fidelity of at least 0.95 decreases relatively slowly as N increases. The same scaling of the absolute time error with N was also numerically found for $S = 4$ and 5 and is due to the fact that the particles behave independently of one another. Indeed this same scaling would be found for any S because in this system the particles are always independent since $V \approx 0$.

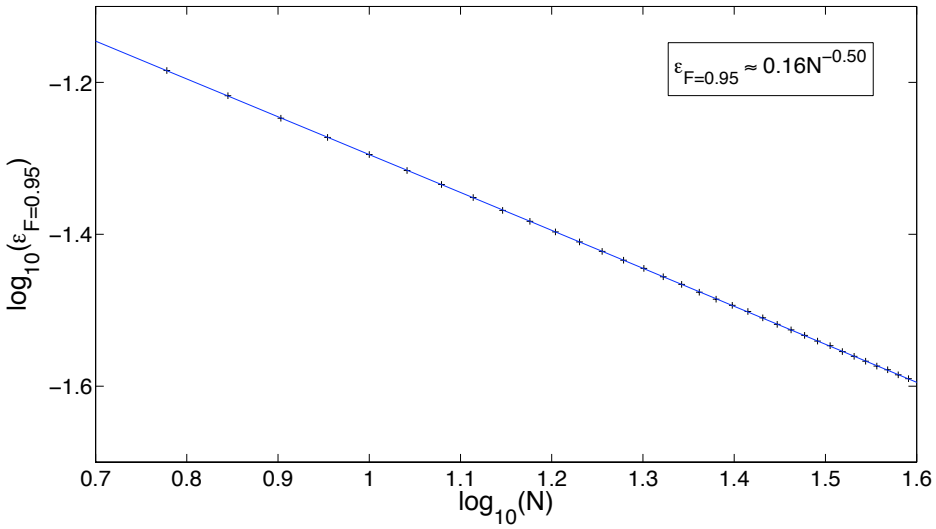

Figure 5.8: The relationship between the absolute time error at a critical fidelity of $F = 0.95$ and the number of atoms, N, for a three site interferometer. The solid curve is a line of best fit and has the form $\epsilon_{F=0.95} \approx 0.16 N^{-0.50}$. We see that as the number of atoms increases, the timing error that can be tolerated decreases.

For $N = 5$ the maximum absolute error that can be tolerated in Jt is $\epsilon \approx 0.07$

for all S where $\epsilon = J\Delta t$ and Δt is the time error in seconds. This means we require that we can control t to at least a precision given by $\Delta t = 0.07/J \approx 1$ms. Therefore, we need a refresh frequency of about a few kilohertz which can be achieved using a ferroelectric liquid crystal spatial light modulator [106] and so we conclude that absolute timing errors do not limit the experimental feasibility of our scheme.

We must also consider the fractional time error that can be tolerated as clocks generate fractional errors. An absolute time error of ϵ corresponds to a fractional time error of $\epsilon/(S\tau)$. We know for $N = 5$ the maximum absolute time error that can be tolerated for all S is approximately 0.07. For $S = 3$ this corresponds to a fractional time error of approximately 0.33 i.e. we can tolerate a fractional time error of one part in 10^1. For $S = 4$ the fractional time error is 0.11 and for $S = 5$ it is 0.01. Accuracies of one part in 10^4 are easily achievable with many readily available pulse pattern generators suggesting the timings required for the scheme are within reach of current experimental technologies for up to five sites.

5.5.5 Loss of particles

The final limiting factor we consider is spontaneous emission which we show to have little effect on the system. In fact, when we ignore interactions, the loss of a particle during the splitting process has no effect on the remaining particles. When N particles are inputted into a tritter and one particle is lost from a particular site halfway through the splitting procedure, we have numerically shown that the fidelity between this output and the output of a tritter into which $N-1$ particles are inputted (and none are lost) is 1 when the interactions are ignored ($V = 0$). Even when interactions are included the loss of fidelity is very small and so spontaneous emissions will not be the limiting factor in this scheme. The robustness of the tritter to particle loss is due to the fact that the particles are independent meaning the loss of one particle has no affect on the remaining $N - 1$ particles.

Taking all these practical limitations into account we have found the limit for S

is five. All that is required to produce these devices is a raising and lowering of the potential barriers and so far fewer components are used than in optical schemes to produce devices with the same number of ports.

5.6 Conclusions

We have proposed a straightforward experimentally accessible scheme for implementing atomic beam splitters (and their inverses) with up to five input and output ports. It requires modulation of the intensity of the optical lattice in which the atoms are trapped – something that is readily achievable in the laboratory. Importantly, in this scheme, the multiport devices require no more operational complexity than an ordinary beam splitter for atoms.

The versatility of these devices means that they are likely to have intriguing prospects for creating interesting entangled states that have uses in quantum technologies such as precision measurement schemes. In particular, the ring lattice means these devices have great potential for use in ultra-precise gyroscopes. With this in mind we develop a gyroscope scheme that uses this system and the multiport splitting operations discussed to make Heisenberg limited rotation measurements in the next chapter.

Chapter 6

A scheme to implement a two-mode atomic gyroscope

As was demonstrated in Chapter 4 the precision of rotation measurements can be improved from the classical scaling of $1/\sqrt{N}$ to the Heisenberg limit of $1/N$ by using highly entangled states. However, these states as well as being difficult to produce, are extremely fragile to particle loss, making unentangled states a more practical choice. Combined with the development of the laser and fibre optics this means that, at present, the most widely used gyroscopes in the navigation industry employ unentangled photons as their probe.

Nevertheless, it has been shown that the precision of gyroscope schemes that employ unentangled particles can be improved by as much as a factor of 10^{10} simply by using atoms rather than light. With this in mind much research has focused on developing matter-wave gyroscopes [80, 107–109]. However, these schemes all use unentangled atoms as their resource and therefore cannot surpass the standard quantum limit. Here we want to develop an atomic scheme to measure rotations with Heisenberg limited sensitivity thereby allowing for precisions far superior to those of current optical gyroscopic devices. Whilst this requires the use of entangled particles that are notoriously fragile we rigorously determine the effects of particle loss and show that for a certain entangled state the standard quantum limit is beaten

for most experimentally realistic loss rates.

The system we consider consists of a BEC trapped in a one-dimensional three site optical ring lattice. We describe ways to produce different initial states, including both classical and highly entangled states, and show how, using two and three mode beam splitting operations (as discussed in the previous chapter) the rate of rotation of the lattice ring can be determined. We find that whilst both the NOON state and the previously introduced bat state achieve similar precisions in the idealised setting, the bat state is far more robust to the effects of particle loss, making it the experimentally preferred state.

6.1 The system

The system consists of a N atom BEC that is trapped by the dipole force in an optical ring lattice of three sites (see figures 2.1 and 2.2). This set-up was discussed in the previous chapter where it was shown how, by carefully evolving the trapping potential, balanced beam splitting operations could be achieved and, in fact, the measurement scheme described in this chapter uses such splitting procedures. As previously shown this system is described by the Bose-Hubbard Hamiltonian

$$\frac{H}{\hbar} = \sum_{j=0}^{2} \epsilon_j a_j^\dagger a_j - \sum_{j=0}^{2} J_j \left(a_j^\dagger a_{j+1} + a_{j+1}^\dagger a_j \right) + \sum_{j=0}^{2} V_j a_j^{\dagger 2} a_j^2. \tag{6.1}$$

Note that until now we have always assumed the tunnelling strength between, and the interactions on, all sites to be equal. Here, however, we have allowed the tunnelling strength between sites to be different which is achieved by having different barrier heights between sites. Similarly, the onsite interactions can be varied between sites using Feshbach resonances. The ability to vary tunnelling between, and interactions on, sites will prove useful in the initial state creation procedure. However, once the initial state has been created we set all J_j and all V_j to be equal.

For the purposes of this work it will be convenient to describe the system in

terms of the flow basis, which (to recap) is related to the site basis by

$$\alpha_k = \frac{1}{\sqrt{3}} \sum_{j=0}^{2} e^{i2\pi jk/3} a_j, \tag{6.2}$$

where α_k corresponds to the annihilation of an atom with angular momentum $\hbar k$. Due to the fact that we are considering a ring of three sites we are limited to the three flow states

$$\begin{aligned} \alpha_0 &= (a_0 + a_1 + a_2)/\sqrt{3} \\ \alpha_1 &= (a_0 + e^{i2\pi/3} a_1 + e^{i4\pi/3} a_2)/\sqrt{3} \\ \alpha_2 &= \alpha_{-1} = (a_0 + e^{-i2\pi/3} a_1 + e^{-i4\pi/3} a_2)/\sqrt{3}. \end{aligned} \tag{6.3}$$

When there are no on-site interactions and all J_j are equal (as will be the case once we have created our initial momentum states) the system is described, in this basis, by the Hamiltonian

$$\frac{H_k}{\hbar} = -2J \sum_{k=-1}^{1} \cos\left(\theta/3 - 2\pi k/3\right) \alpha_k^\dagger \alpha_k \tag{6.4}$$

where θ is a phase induced around the ring due to a rotation $\delta\omega$.

6.2 Scheme 1: Unentangled particles

Here we describe the rotation measurement scheme. This includes a description of how to create the initial state and, then, how to use this state to make precision measurements. As previously mentioned we will not concern ourselves too much with the phase readout procedure as we are primarily interested in ways to improve precision simply by optimising the initial state. We do, however, briefly suggest a possible way to readout the phase for each initial state we consider, but all our precision calculations are independent of this procedure.

For simplicity we begin by considering an unentangled initial state. This is

intended to introduce the scheme which will be similar to the schemes used for all the other initial states we consider. It also provides a benchmark to which we can compare the precision of these other states, as any state that outperforms classical precision capabilities is of fundamental interest to the metrology community.

To begin with, the potential barriers between the three sites are high and N atoms are contained within one site, say site zero. The initial state of the system is therefore $|\psi_{U0}\rangle = |N,0,0\rangle_{a_0,a_1,a_2}$ where the terms in the ket represent the number of atoms in sites zero, one and two respectively.

The first step in the scheme is to apply a balanced two-mode beam splitting operation to this state. The exact procedure to achieve this for a BEC in an optical lattice was first described in [51] and is implemented in a very similar manner to the multimode beam splitting operations introduced in the previous chapter. Here the potential barrier between just two sites, we choose sites zero and one, is rapidly reduced in such a way that the two sites remain separate but there is strong coupling between them. This must be done rapidly with respect to the tunnelling time, but slowly with respect to the energies associated with excited states in order to ensure the system remains in the ground state. In this regime the tunnelling between the two sites is much larger than their on-site interactions and the Hamiltonian describing the two sites is

$$\frac{H_{2J}}{\hbar} = -J(a_0^\dagger a_1 + a_1^\dagger a_0). \tag{6.5}$$

Importantly, the remaining two barriers are high ($V \gg J$) and so prevent tunnelling between sites one and two and sites two and zero. The system is then left to evolve for time $t = \pi/(4J)$ whilst this barrier is low. This is equivalent to applying a two port 50:50 beam splitter to our initial state and so transforms $|\psi_{U0}\rangle$ to

$$|\psi_{U1}\rangle = \frac{1}{\sqrt{2^N N!}}(a_0^\dagger + ia_1^\dagger)^N |0,0,0\rangle_{a_0,a_1,a_2}. \tag{6.6}$$

Each individual atom is now equally likely to be on site zero or one. In other words

the atoms are unentangled and we have N single-particle superpositions on the two sites. We now need to convert these site superpositions into superpositions of each atom flowing in opposite directions around the ring (just like the photons in a Sagnac gyroscope).

To do this we first apply a tritter to the system as described in Chapter 5. Essentially all we do is, immediately after $t = \pi/(4J)$, lower the two remaining potential barriers, on the same timescale as before, and allow the system to evolve for a further $t = 2\pi/(9J)$. This transforms $|\psi_{U1}\rangle$ to

$$|\psi_{U2}\rangle = \frac{1}{\sqrt{2^N 3^N N!}} \Big((a_0^\dagger + e^{i2\pi/3} a_1^\dagger + e^{i2\pi/3} a_2^\dagger) + i(e^{i2\pi/3} a_0^\dagger + a_1^\dagger + e^{i2\pi/3} a_2^\dagger) \Big)^N |0,0,0\rangle_{a_0,a_1,a_2}. \tag{6.7}$$

At this point we rapidly raise the potential barriers, freezing the atoms in the lattice sites. Comparing $|\psi_{U2}\rangle$ with equation 6.3 we see that applying a $2\pi/3$ phase to site two results in a superposition of the α_{-1} and α_1 flow states. This phase is achieved by applying an energy offset, ϵ_2, to site two, whilst the barriers are high, for time $t_\epsilon = 4\pi/(3\epsilon_2)$. This time assumes $J = 0$ and $V = 0$. Of course, this is not the case when the barriers are high. However, we assess the impact of non-zero values of J and V on the scheme as a whole in section 6.5.3. We note also that offset application times of 500ns have been demonstrated experimentally [110] and it is this time we shall use in section 6.5.3 when we assess the impact of non-zero interactions.

We then immediately lower the barriers again so the atoms can flow around the loop. The resulting superposition can be written as,

$$|\psi_{U3}\rangle = \frac{1}{\sqrt{2^N N!}} (\alpha_{-1}^\dagger + i\alpha_1^\dagger)^N |0,0,0\rangle_{\alpha_{-1},\alpha_0,\alpha_1} \tag{6.8}$$

where the terms in the ket now represent the number of atoms in each of the possible flow states, α_{-1}, α_0 and α_1 respectively. This is now the N single-particle flow superposition we required.

At this point the α_{-1} and α_1 states are degenerate, so $|\psi_{U3}\rangle$ does not evolve.

However, we now apply the rotation we wish to measure, $\delta\omega$, to the ring which causes a phase, θ, to be applied around it. The energies of the two flow states now change according to the Hamiltonian given in equation 6.4.

After a time t_ω, and ignoring global phases, the state has evolved to

$$|\psi_{U4}\rangle = \frac{1}{\sqrt{2^N N!}} \Big(e^{i2Jt_\omega \cos(\theta/3+2\pi/3)} (\alpha_{-1}^\dagger) + ie^{i2Jt_\omega \cos(\theta/3-2\pi/3)} (\alpha_1)^\dagger \Big)^N |0,0,0\rangle_{\alpha_{-1},\alpha_0,\alpha_1} \tag{6.9}$$

and so a phase difference of $\phi = 2\sqrt{3}Jt_\omega \sin(\theta/3)$ is established between the two flows.

We can now calculate the precision afforded by this scheme using the relation $\Delta\phi = 1/\sqrt{F_Q}$ since we have shown that the F_Q of a pure state, $|\psi(\phi)\rangle$, is given by

$$F_Q = 4\left[\langle\psi'(\phi)|\psi'(\phi)\rangle - \left|\langle\psi'(\phi)|\psi(\phi)\rangle\right|^2\right]. \tag{6.10}$$

Expanding and simplifying equation 6.9 gives

$$|\psi_{U4}\rangle = \frac{1}{\sqrt{2^N}} \sum_{n=0}^{N} \binom{N}{n}^{1/2} i^n e^{in\phi} |N-n,0,n\rangle_{\alpha_{-1},\alpha_0,\alpha_1} \tag{6.11}$$

from which we find $F_Q = N$ and hence $\Delta\phi = 1/\sqrt{N}$, or equivalently $\Delta\theta = \sqrt{3}/(2Jt_\omega \cos(\theta/3)\sqrt{N})$. Using the relation $\delta\omega = h\theta/(L^2 m)$ first introduced in Chapter 2 this translates to an uncertainty in $\delta\omega$ of

$$\Delta(\delta\omega) \sim \left(\frac{h}{L^2 m}\right) \frac{\sqrt{3}}{2Jt_\omega\sqrt{N}} \tag{6.12}$$

where we have made the approximation that $\theta/3 \ll 1$. This has the well-known $1/\sqrt{N}$ scaling that is a signature of the standard quantum limit.

We now suggest a possible procedure to read-out a value for ϕ. It involves sequentially undoing all the operations performed prior to the phase shift. This is analogous to standard Mach-Zehnder interferometry where an (inverse) beam

splitter is placed after the phase shift to undo the initial beam splitting operation.

The undoing process begins with the application of a $-2\pi/3$ phase to site two giving

$$|\psi_{U5}\rangle = \frac{1}{\sqrt{2^N 3^N N!}} \Big((a_0^\dagger + e^{i2\pi/3} a_1^\dagger + e^{i2\pi/3} a_2^\dagger) + ie^{i\phi}(e^{i2\pi/3} a_0^\dagger + a_1^\dagger + e^{i2\pi/3} a_2^\dagger) \Big)^N |0,0,0\rangle_{a_0,a_1,a_2} \tag{6.13}$$

where the terms in the kets now, once again, represent the number of atoms in sites zero, one and two. Next we undo the tritter by applying an inverse tritter. The procedure used to create an inverse tritter in this system was discussed in the previous chapter but is essentially achieved by lowering all three barriers and allowing the system to evolve for time $t = 4\pi/(9J)$ (i.e. twice as long as for a tritter) giving

$$|\psi_{U6}\rangle = \frac{1}{\sqrt{2^N N!}} \left(a_0^\dagger + ie^{i\phi} a_1^\dagger \right)^N |0,0,0\rangle_{a_0,a_1,a_2} \tag{6.14}$$

which is equivalent to $|\psi_{U1}\rangle$ but with a phase difference, ϕ.

Finally we apply an inverse two-port 50:50 beam splitter. This is achieved in just the same way as the two-port beam splitting operation described above, but with a hold time of $t = 3\pi/(4J)$ rather than $t = \pi/(4J)$. The resulting state is

$$|\psi_{U7}\rangle = \frac{1}{\sqrt{N!}} \left(\cos\left(\frac{\phi}{2}\right) (a_0^\dagger) - \sin\left(\frac{\phi}{2}\right) (a_1^\dagger) \right)^N |0,0,0\rangle_{a_0,a_1,a_2} \tag{6.15}$$

meaning the probabilities of detecting each atom at site zero and site one are

$$\begin{aligned} P_0 &= \cos^2\left(\frac{\phi}{2}\right) \\ P_1 &= \sin^2\left(\frac{\phi}{2}\right). \end{aligned} \tag{6.16}$$

Since the atoms are independent the total number detected in the two sites is given by a binomial distribution. The mean number of atoms detected at site zero is therefore $\langle n_0 \rangle = N\cos^2(\phi/2)$ and at site one it is $\langle n_1 \rangle = N\sin^2(\phi/2)$. By counting

the number of atoms detected at each site we can determine ϕ, and hence $\delta\omega$, just as in a typical Mach-Zehnder interferometer.

To summarise, we can measure rotations at the standard quantum limit as follows:

1. Apply a two-port 50:50 beam splitter to the first two modes of $|N,0,0\rangle_{a_0,a_1,a_2}$.
2. Then apply a tritter to the resulting state.
3. Apply a $2\pi/3$ phase to site two.
4. Leave the system to evolve for time t_ω under the rotation, $\delta\omega$.
5. Apply a $-2\pi/3$ phase to site two.
6. Perform an inverse tritter operation on the state.
7. Apply an inverse two-port 50:50 beam splitter to the first two modes.
8. Count the number of atoms in each site.

We will now show how two different entangled states can be created in this system, and how using a similar method to above, a small rotation, $\delta\omega$, can be measured. We compare the precision of these entangled states with that of the scheme above.

6.3 Scheme 2: The bat state

The first entangled state we create is the bat state. We begin with $N/2$ atoms on site zero and on site one, i.e. $|\psi_{B0}\rangle = |N/2, N/2, 0\rangle_{a_0,a_1,a_2}$. This number squeezed state could be achieved by slowly applying a double well trapping potential to a condensate so that a phase transition occurs to the Mott insulator state. States with approximately equal numbers of BEC atoms ($N \sim 1000$) on two lattice sites have indeed already been demonstrated in a one-dimensional optical lattice [67].

We assume we begin with $|\psi_{B0}\rangle$ and that the barriers between the three sites are high. As in scheme 1, a two-port beam splitter is applied to the first two modes of $|\psi_{B0}\rangle$ by lowering the potential barrier between sites zero and one for $t = \pi/(4J)$.

The resulting output is a bat state in the site basis which is given by

$$|\psi_{B1}\rangle = \frac{1}{\sqrt{2^N}(N/2)!}\left((a_0^\dagger)^2 + (a_1^\dagger)^2\right)^{N/2}|0,0,0\rangle_{a_0,a_1,a_2} \tag{6.17}$$

where a global phase has been ignored. As in the previous scheme we now need to convert this into a bat state in the flow basis so as to have a superposition of atoms flowing in opposite directions around the ring.

This is achieved by applying a tritter followed by a $2\pi/3$ phase to site two as before. We then let the system evolve under the influence of $\delta\omega$ for t_ω with the barriers low giving

$$|\psi_{B4}\rangle = \frac{1}{\sqrt{2^N}(N/2)!}\left((\alpha_{-1}^\dagger)^2 + e^{i2\phi}(\alpha_1^\dagger)^2\right)^{N/2}|0,0,0\rangle_{\alpha_{-1},\alpha_0,\alpha_1} \tag{6.18}$$

where ϕ is again given by $\phi = 2\sqrt{3}Jt_\omega \sin(\theta/3)$. The precision afforded by this scheme is determined using equation 6.10 and is found to be $\Delta\phi = 1/\sqrt{N(N/2+1)}$ meaning $\Delta\theta = \sqrt{3}/(2Jt_\omega\cos(\theta/3)\sqrt{N(N/2+1)})$. The uncertainty in $\delta\omega$ is therefore

$$\Delta(\delta\omega) = \left(\frac{h}{L^2m}\right)\frac{\sqrt{3}}{2Jt_\omega\cos(\theta/3)\sqrt{N(N/2+1)}} \sim \left(\frac{h}{L^2m}\right)\frac{\sqrt{3}}{\sqrt{2}Jt_\omega N}, \tag{6.19}$$

where we have made the approximations $N \gg 1$ and $\theta/3 \ll 1$. This has the same number scaling as the Heisenberg limit showing the bat state is a good candidate for precision measurements of rotations.

We now suggest a possible way to readout the phase information which, as before, begins by sequentially undoing all the steps prior to the application of $\delta\omega$, that is, we first apply a $-2\pi/3$ phase to site two followed by an inverse tritter and an inverse two-port 50:50 beam splitter operation. This results in the state

$$|\psi_{B7}\rangle = \frac{1}{2^N\,(N/2)!}\left(\left(a_0^\dagger - ia_1^\dagger\right)^2 + e^{i2\phi}\left(-ia_0^\dagger + a_1^\dagger\right)^2\right)^{N/2}|0,0,0\rangle_{a_0,a_1,a_2}. \tag{6.20}$$

This scheme is very similar to the scheme described in reference [100], where a bat state is used to measure a phase difference in a general Mach-Zehnder interferometer

set-up, and in fact results in the same output. The difference between the schemes is that ours has been adapted to measure a rotation around a ring of lattice sites rather than a general phase between two paths.

To determine ϕ we use the readout scheme described (in detail) in reference [100]. Essentially, after step 7 the system is left to evolve with the barriers high for $t = \pi/(16V)$ (note in the original paper $t = \pi/(8U)$ because $U = 2V$ here). The trapping potentials are then switched off and after some expansion time interference fringes are recorded. These two steps are the readout steps and are what we shall refer to as step 8. The scheme is repeated many times and the visibility of the fringes is calculated as in reference [100]. From these visibility measurements we determine ϕ directly.

The final scheme we describe creates and uses a NOON state to measure $\delta\omega$ and also allows for Heisenberg limited precision. We then compare the precision of the three schemes in the presence of loss so as to see which is the more experimentally viable.

6.4 Scheme 3: The NOON state

Again this scheme is very similar to scheme 1, the only difference is that the two-port 50:50 beam splitter (and its inverse) is replaced with a two-port quantum beam splitter (and an inverse two-port quantum beam splitter). A two-port quantum beam splitter (QBS) is defined as a device [90] that outputs a NOON state of the form $(|N,0\rangle + e^{i\xi}|0,N\rangle)/\sqrt{2}$ when $|N,0\rangle$ is inputted.

The scheme, as before, begins with the three potential barriers raised and N atoms on site zero, $|\psi_{N0}\rangle = |N,0,0\rangle_{a_0,a_1,a_2}$. The first step is to apply the QBS. This is done using a scheme proposed in reference [51].

The QBS begins with the application of a two-port 50:50 beam splitter between sites zero and one, as previously described. A $\pi/2$ phase is then applied to one of the two sites using an energy offset as above. At this stage $V \gg J$ and the interactions are tuned such that their strength on one site is an integer multiple of the strength

on the second site [1]. The system is left to evolve for $t = \pi/(2V)$ in this regime after which a second two-port beam splitter is applied. These steps output

$$|\psi_{N1}\rangle = \frac{1}{\sqrt{2N!}}\left((a_0^\dagger)^N + e^{i\xi}(a_1^\dagger)^N\right)|0,0,0\rangle_{a_0,a_1,a_2}. \tag{6.21}$$

where ξ is some relative phase established by the splitting procedure.

Here we have a superposition of all N atoms on site zero and all on site one. At the equivalent stage in scheme 1 we had N single-particle superpositions (see equation 6.6). It is this difference that will allow us to achieve Heisenberg limited precision but in order to measure $\delta\omega$ we must convert this site superposition into a flow superposition. The procedure to achieve this is exactly the same as in schemes 1 and 2. Therefore, after the application of $\delta\omega$ for time t_ω we have

$$|\psi_{N4}\rangle = \frac{1}{\sqrt{2N!}}\left((\alpha_{-1}^\dagger)^N + e^{i\xi}e^{iN\phi}(\alpha_1^\dagger)^N\right)|0,0,0\rangle_{a_0,a_1,a_2}. \tag{6.22}$$

Using the F_Q and the Cramér-Rao lower bound we find the maximum resolution of this scheme is $\Delta\theta = \sqrt{3}/(2Jt_\omega\cos(\theta/3)N)$ meaning, for $\theta/3 \ll 1$,

$$\Delta(\delta\omega) \sim \left(\frac{h}{L^2m}\right)\frac{\sqrt{3}}{2Jt_\omega N}. \tag{6.23}$$

So we see the NOON state offers a slight improvement in resolution over the bat state as although it has the same number scaling the numerical factor is $\sqrt{2}$ better. However, as we shall show in chapter 6.5.1 this slight improvement in resolution comes at a great experimental expense.

First, however, we suggest a possible readout method. It begins with the removal of the $2\pi/3$ phase followed by the application of an inverse tritter which results in the state

$$|\psi_{N6}\rangle = \frac{1}{\sqrt{2N!}}\left((a_0^\dagger)^N + e^{i\xi}e^{iN\phi}(a_1^\dagger)^N\right)|0,0,0\rangle_{a_0,a_1,a_2}. \tag{6.24}$$

The final step is to apply an inverse two-port quantum beam splitter to the system.

[1] This ensures that the required superposition is created independent of the total number of atoms.

This is achieved by sequentially undoing all the steps of the QBS. So,

1. Apply an inverse two-port beam splitter.
2. Raise the barriers and tune the interactions as before.
3. Leave the system to evolve for $t = \pi/(2V)$.
4. Apply a $-\pi/2$ phase to the same site as before.
5. Apply a second inverse two-port beam splitter.
6. Raise the barriers.

This results in all N atoms detected at site zero or all at site one with respective probabilities,

$$P_0 = \cos^2\left(\frac{N\phi}{2}\right) \qquad (6.25)$$
$$P_1 = \sin^2\left(\frac{N\phi}{2}\right).$$

By repeating the scheme many times, each time recording the site on which all N atoms are detected, ϕ, and hence $\delta\omega$, can be determined.

6.5 Comparisons and practical limitations

Both schemes 2 and 3 allow Heisenberg limited precision measurements of small rotations with the precision capabilities of scheme 3 being marginally favourable. Our descriptions thus far, however, have only considered the idealised case and we have neglected important physical processes that may limit the experimental feasibility of the schemes. We now reevaluate the schemes when these limitations are accounted for.

6.5.1 Particle loss

The first unwanted physical process we consider is the loss of atoms to the environment. It is well known that NOON states undergoing particle loss decohere quickly, and so soon lose their Heisenberg limited sensitivity. Here we wish to see how resistant the bat state is to particle loss in comparison to the NOON and unentangled

states by determining the precisions achievable by all three schemes in the presence of loss.

We investigate the effects of loss using the imaginary beam splitter model introduced in Chapter 3, that is, an imaginary beam splitter with transmissivity η_k is placed in momentum mode k. In this way the rate of loss can be varied in each mode by altering the value of η_k. By calculating the precision that can be achieved by each scheme for different values of η_k we can therefore determine which scheme affords the best precision for a particular loss rate.

In this model the imaginary beam splitters are placed between the two beam splitters of a MZI. This is equivalent to placing them in the momentum modes during time t_ω in our system. Since losses are equally likely from both modes we consider equal loss rates from each momentum mode i.e. $\eta_1 = \eta_{-1} = \eta$. As was shown in Chapter 3 the F_Q of the system can be calculated for different η using the equation

$$F_Q = \sum_{l=0}^{N} F_Q \left[\sum_{l_\alpha=0}^{l} p_{l_{\alpha_1},l-l_{\alpha_1}} |\xi_{l_{\alpha_1},l-l_{\alpha_1}}(\phi)\rangle\langle\xi_{l_{\alpha_1},l-l_{\alpha_1}}(\phi)|, \right], \tag{6.26}$$

where $F_Q[\cdot]$ denotes the F_Q of the state in brackets, l_{α_1} is the number of particles lost from mode α_1, $p_{l_{\alpha_1},l-l_{\alpha_1}}$ is the probability of each loss event and

$$|\xi_{l_{\alpha_1},l-l_{\alpha_1}}(\phi)\rangle = \frac{1}{\sqrt{p_{l_{\alpha_1},l-l_{\alpha_1}}}} \sum_{n=l_{\alpha_1}}^{N-(l-l_{\alpha_1})} \beta_n e^{in\phi} \sqrt{B^n_{l_{\alpha_1},l-l_{\alpha_1}}} |n-l_{\alpha_1}, N-n-(l-l_{\alpha_1})\rangle. \tag{6.27}$$

Here

$$B^n_{l_{\alpha_1},l-l_{\alpha_1}} = \binom{n}{l_{\alpha_1}} \binom{N-n}{l-l_{\alpha_1}} \eta^N (\eta^{-1}-1)^l \tag{6.28}$$

and β_n is

$$\beta_n = \frac{\sqrt{n!}\sqrt{(N-n)!}}{2^{N/2}(n/2)!(N/2-n/2)!} \times \frac{1+(-1)^n}{2} \tag{6.29}$$

for the bat state and

$$\beta_n = \begin{cases} 1/\sqrt{2} & \text{for } n = 0, N \\ 0 & \text{for } n \neq 0, N \end{cases}$$

for the NOON state. F_Q is found numerically using

$$F_Q = Tr[\rho(\phi)A^2] \tag{6.30}$$

where A is the symmetric logarithmic derivative defined in Chapter 3.

Figure 6.1 shows how $\Delta\phi$ varies with η for the three schemes when $N = 10$. As expected the NOON state achieves the best precision when $\eta = 1$ (when there are no losses). However, as η decreases the bat state soon becomes the favoured scheme. The lower bound of the shaded area is the Heisenberg limit and the upper bound is the precision achievable when an unentangled, or classical, initial state is used, as in scheme 1. We see the classical state soon outperforms the NOON state. However, the bat state outperforms the classical state for approximately half the loss rates shown. Since it is unlikely half the atoms would be lost in an experiment, the bat state, unlike the NOON state, appears to offer an experimentally feasible increase in precision over classical precision measurement experiments. In the remainder of the paper we therefore assess the impact of experimental limitations on just scheme 2.

6.5.2 Variations in N between experimental runs

Our scheme requires many repetitions of the gyroscope procedure in order to build up interference fringes from which ϕ can be determined. We have assumed thus far that each run involves exactly N atoms. However, in an experiment N is likely to fluctuate between runs. The effect of fluctuations of order $\sqrt{N}$ on the bat state are discussed in reference [100]. In that case, an ordinary two-path linear interferometer is used but the same results apply here. It was shown that while the interference fringe signal is degraded by these fluctuations, the approximate Heisenberg limited sensitivity of the scheme is not destroyed. As expected, the larger N, the smaller

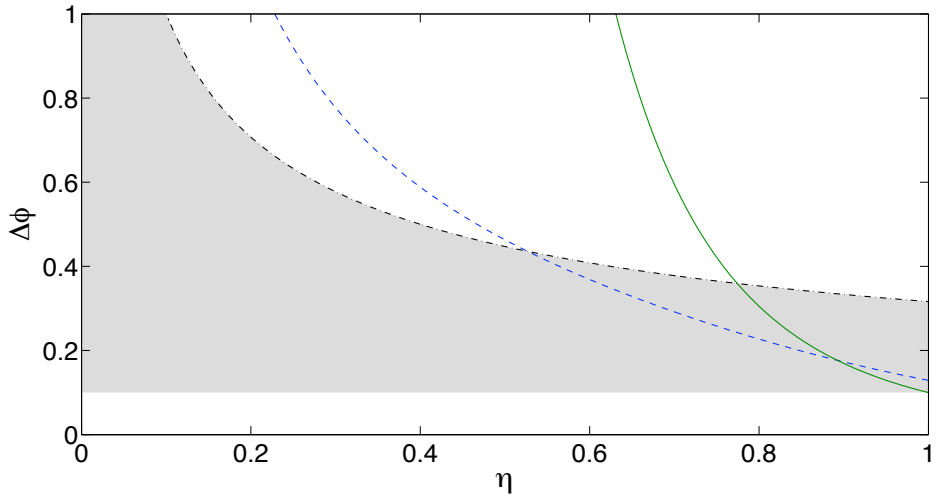

Figure 6.1: The uncertainty of ϕ for different rates of loss, η, for $N = 10$. The blue dashed line shows $\Delta\phi$ for scheme 2 and the green solid line shows $\Delta\phi$ for scheme 3. The upper bound of the shaded region is the precision afforded by scheme 1 (the standard quantum limit - black dashed-dotted line) and the lower bound shows the Heisenberg limit. Scheme 3 soon becomes less favourable than scheme 1, whilst scheme 2 is much more robust to losses.

the fluctuation effects, which is good since we would ideally work in the limit of large N since this gives the best improvement in precision.

6.5.3 Interactions

So far we have considered only the idealised system setting $V = 0$ (apart from in the detection step, step 8, where we require large interactions to minimise small tunnelling effects), and $J = 0$ in the low coupling regime. While interactions can be tuned to extremely small values using Feshbach resonances it is an unrealistic assumption to discount them altogether. Likewise it is unrealistic to completely neglect coupling effects in the low coupling regime. Here we consider the effect of non-zero interactions and non-zero coupling strengths in the low coupling regime on scheme 2. As in the previous chapter we determine experimental orders of magnitude for V and J using the approximations [101] given in equations 5.19 and 5.20. In the high coupling regime, where $V_0 = 2E_R$, we have previously shown $V \sim 10^{-3}$Hz and $J \sim 10$Hz. While in the low coupling regime, where $V_0 = 35E_R$ [97], we find

$V \sim 10^{-2}$Hz and $J \sim 10^{-2}$Hz. Note that in the detection process the system evolves for $t = \pi/(16V)$ with high potential barriers. Here we require large interactions to minimise small coupling effects. Taking $a_s = 9000a_0$ [98] gives $V \sim 100$Hz. Using these values we assess the impact of non-zero interactions and coupling strengths on the system as a whole.

As N increases the occupation number per site increases and as such the effect of non-zero interactions become more pronounced. We would therefore like to determine the maximum number of atoms our system can tolerate before these effects become too destructive. To do this we measure the fidelity between the output of the gyroscope in the idealised case in which $V = 0$ (except in step 8) and $J = 0$ in the low coupling regime with the same output when $V \sim 10^{-3}$ in the high coupling regime ($J = 10$Hz in this regime), $V \sim 10^{-2}$ in the low coupling regime and $J \sim 10^{-2}$ in the low coupling regime. The maximum N that can be tolerated is taken to be the first N for which this fidelity falls below 0.99. In this simulation we have taken $t_\omega = 1$s and $\theta = \pi/100$. Figure 6.2 shows how the fidelities decrease as N increases. We see that by our definition the maximum number of atoms the system can tolerate is approximately 60. Squeezed states with larger numbers of atoms have been demonstrated experimentally [67] and as such interactions are likely to be the main factor that limits N in, and hence the precision capabilities of, this scheme.

We note here that this simulation takes into account the effects of non-zero interactions (and non-zero coupling strengths in the low coupling regime) throughout the entire scheme. In section 6.2 we discussed how a $2\pi/3$ phase could be applied to site two using an energy off-set ϵ_2. The required phase was achieved by applying the off-set for time $t_\epsilon = 4\pi/(3\epsilon_2)$. This assumed both $J = 0$ and $V = 0$ which is obviously experimentally unrealistic. We have accounted for this in the simulation by setting $V = J = \sim 10^{-2}$ since the barriers were high during the application of ϵ_2.

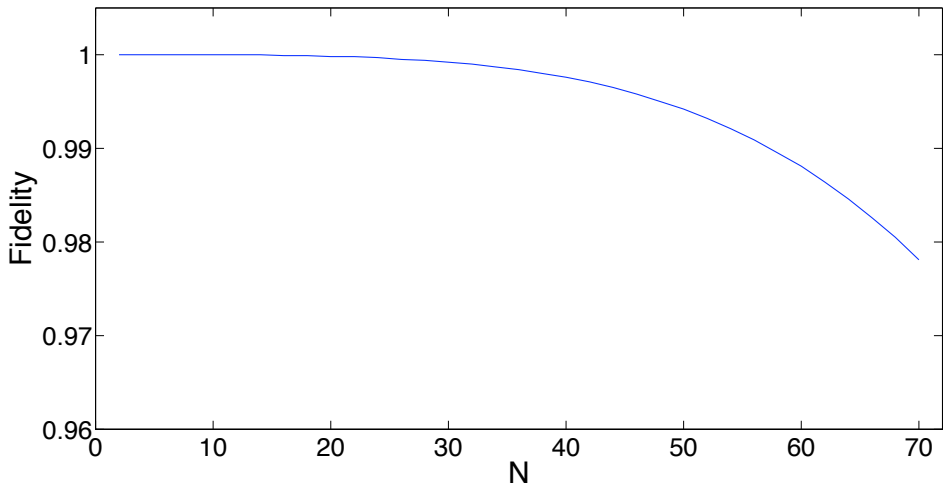

Figure 6.2: The fidelity between the output of scheme 2 in the idealised case (where $V = 0$, and $J = 0$ in the low coupling regime) with the output in the non-idealised case (where $V \sim 10^{-3}$ in the high coupling regime, $V \sim 10^{-2}$ in the low coupling regime and $J \sim 10^{-2}$ in the low coupling regime) for different numbers of input atoms. Here $\theta = \pi/100$ and $t_\omega = 1$s.

6.5.4 Comparison with other schemes

At this point we note that our precision analysis is for the case of a single shot, i.e. N atoms are loaded into the lattice and a single measurement is made over time t_ω. In reality, the results of many runs will be combined to give a measurement of the rotation. Suppose we repeat the measurement ν times to give a total integration time of $\tau = \nu t_\omega$. In this case, we get

$$\Delta(\delta\omega) \approx \left(\frac{h}{L^2 m}\right) \frac{\sqrt{3}}{\sqrt{2\nu} J t_\omega N} = \left(\frac{h}{L^2 m}\right) \frac{\sqrt{3}}{\sqrt{2 t_\omega \tau} J N} = \frac{S}{\sqrt{\tau}}, \tag{6.31}$$

where the short-term sensitivity is given by

$$S = \left(\frac{h}{L^2 m}\right) \frac{\sqrt{3}}{\sqrt{2 t_\omega} J N}. \tag{6.32}$$

Substituting in approximate values for our set-up in the strong coupling regime (i.e. $J \approx 10$Hz, $N \approx 60$, $t_\omega \approx 1$s and $L = 2\pi \times 20\mu$m [37]), we get $S \approx 10^{-3}$ rads$^{-1}/\sqrt{\text{Hz}}$. This compares unfavourably with other atom interferometry schemes

which can achieve sensitivities better than 10^{-8} rads$^{-1}/\sqrt{\text{Hz}}$ [107]. These other schemes achieve improved sensitivities by having much larger particle fluxes (e.g. 6×10^8 atoms/s) and much larger areas enclosed by their interferometer paths (e.g. 22 mm^2) [107].

The scheme presented here is therefore unlikely to challenge the overall precision offered by other techniques, except perhaps in specialised cases where the number of atoms available is restricted to a small number or the area of the interferometer must be very small. The main interest of this scheme, however, is that it proposes a means of creating macroscopic superpositions of flows and that these could show evidence of Heisenberg scaling of measurement precision. This in itself would be of fundamental interest. In order to improve its short-term sensitivity, however, it is likely to be difficult to create entangled states with very large numbers of particles, so a different configuration would need to be used to greatly enhance the enclosed area of the interferometer.

6.6 Conclusion

We have presented three schemes to measure small rotations applied to a ring of lattice sites by creating superpositions of ultra-cold atoms flowing in opposite directions around the ring. Two of these schemes are capable of Heisenberg limited precision measurements where the precision scales as $1/N$. The two schemes use different entangled states. While the scheme that uses a NOON state gives slightly better precision in the idealised case, after consideration of experimental limitations it was shown that the bat state is likely to be the preferred candidate largely due to its robustness to particle loss. Importantly the bat state outperformed the case of unentangled particles for modest loss rates. The effects of non-zero interactions were shown to limit the preferred scheme to approximately 60 atoms and as such this scheme is not capable of outperforming the precision of existing atomic gyroscopes at present. However, the interesting result is the Heisenberg scaling of the precision. All the steps in this scheme should be within reach of current technologies which is

promising for its experimental implementation.

Whilst the bat state was shown to beat the classical gyroscope for modest loss rates, for $\eta \lesssim 0.5$ the unentangled state offered better precision than the bat state. Ideally we would like to find a state that beats the precision capabilities of the classical gyroscope for all loss rates. In the next chapter we investigate the precision that can be attained with a different initial state which uses many momentum modes rather than just two. We find that using multiple momentum modes the precision capabilities of the uncorrelated initial state can indeed be beaten for all loss rates.

Chapter 7

A multimode gyroscope

In the previous chapter we presented a scheme designed to precisely measure rates of rotation. The precision capabilities of different initial states were investigated, both in the presence and absence of particle losses with the bat state proving the most promising overall. All the initial states, however, were two-mode states, that is, each atom had either +1 or -1 quantum of angular momentum. In this chapter we show that when the Hilbert space consists of many momentum modes, rather than just two, rotations can be measured with Heisenberg limited precision and can be even more robust to the effects of particle loss than the bat state.

7.1 The system

As before, the gyroscope scheme uses a BEC of N atoms. However, we now confine the atoms to a continuous one-dimensional optical ring potential rather than a ring of lattice sites. Again, we take the circumference of the ring to be $L = 2\pi R$ and describe the position of an atom in the ring by the single variable $x = \varphi R$ (see figure 7.1). The potential is intersected by a focused blue-detuned laser beam which acts as a barrier for the atoms. It is rotated around the circumference of the ring at angular velocity $\omega = h\theta/(mL^2)$. This set-up is shown in figure 7.1 and is described

in the co-rotating frame of reference by the Hamiltonian $H = H_K + H_B + H_I$ where,

$$\begin{aligned} H_K &= \sum_{k=-\infty}^{\infty} E_0 \left(k - \frac{\theta}{2\pi}\right)^2 a_k^\dagger a_k \\ H_B &= \frac{b}{L} \sum_{k_1,k_2=-\infty}^{\infty} a_{k_1}^\dagger a_{k_2} \\ H_I &= \frac{g}{2L} \sum_{k_1,k_2,q=-\infty}^{\infty} a_{k_1}^\dagger a_{k_2}^\dagger a_{k_1-q} a_{k_2+q}. \end{aligned} \tag{7.1}$$

Here, and throughout this chapter, $a_k^\dagger$ and a_k create and destroy an atom with angular momentum $k\hbar$ respectively, m is the mass of an atom, b is the strength of the barrier, g is the inter-atomic interaction strength and $E_0 = 2\pi^2\hbar^2/(mL^2)$ is the smallest non-zero kinetic energy of a single atom.

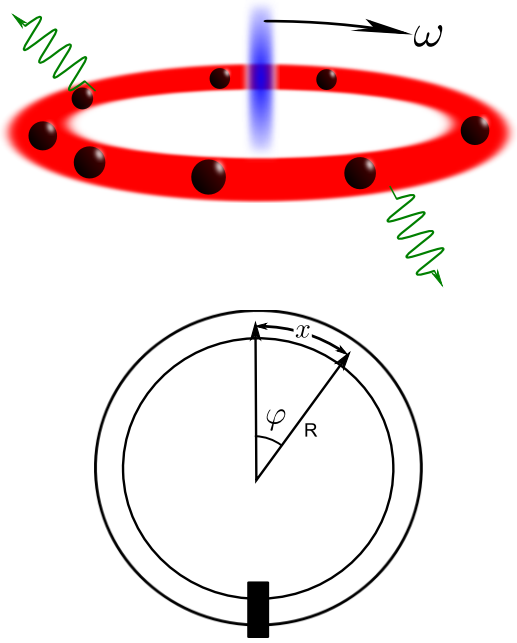

Figure 7.1: Top: A visual representation of the system. The N atoms of a BEC are trapped in an optical ring potential and are 'stirred' by a barrier which moves with angular velocity $\omega = h\theta/(mL^2)$. The green lines represent the loss of atoms to the environment which will be discussed later in the chapter. Bottom: An alternative view of the system. The black box represents the barrier. The position of an atom is given by $x = \varphi R$ where R is the radius of the ring.

7.2 Creating the initial state

The dynamics of this system, in particular the effects of changing the inter-particle interaction strength, were investigated in detail in reference [111]. It was shown in this work that it is possible to put the system into a superposition which has a total angular momentum difference of $N\hbar$ whilst spreading the momentum of the individual atoms over many momentum modes. This state is given by $|\psi_{\mathrm{TG}}\rangle = (|0\rangle + |N\rangle)/\sqrt{2}$ (the terms in the kets represent the total angular momentum of the system divided by $\hbar$) and shall be referred to as a TG cat state. Its structure is very different to a NOON state, $|\psi_{\mathrm{NOON}}\rangle = (|N,0\rangle + |0,N\rangle)/\sqrt{2}$ (here the terms in the kets represent the number of particles with 0 and $\hbar$ angular momentum respectively), which is also a superposition state that has a total angular momentum difference of $N\hbar$. As we shall show, this structural difference has huge consequences on the TG cat state's ability to make precise rotation measurements in the presence of particle loss. Here we briefly describe how to create both the NOON and the TG cat state following the work of references [111, 112]. The main focus of this chapter, however, is how this TG cat state can be used to make precise and robust rotation measurements.

To understand the state creation procedure we begin by considering the dynamics of a single atom in the system. The Hamiltonian describing this set-up in the co-rotating frame is

$$H = \frac{\hbar^2}{2m}\left(-i\frac{\partial}{\partial x} - \frac{\theta}{L}\right)^2 + b\delta(x). \tag{7.2}$$

Writing the wavefunction as

$$\psi(x) = u(x)e^{i\theta x/L} \tag{7.3}$$

and substituting this into the Schrödinger equation we find

$$-\frac{\hbar^2}{2m}\frac{\partial^2}{\partial x^2}u(x) + b\delta(x)u(x) = Eu(x) \tag{7.4}$$

where the boundary conditions mean $u(x) = u(x+L)e^{i\theta}$. To solve this Schrödinger equation we begin by integrating over the barrier which gives

$$\left.\frac{\partial u(x)}{\partial x}\right|_{x=0} - e^{i\theta}\left.\frac{\partial u(x)}{\partial x}\right|_{x=L} = \frac{2mbu(0)}{\hbar^2}. \tag{7.5}$$

Notice that the E term has disappeared because the barrier is described by a delta function and as such does not have a width meaning there is no energy across the it. Using the ansatz $u(x) = e^{i2\pi\xi x/L} + A_0 e^{-i2\pi\xi x/L}$ and the boundary condition above it is then easy to show $A_0 = e^{i2\pi\xi}S_0$ where $S_0 = \sin(\pi\xi + \theta/2)/\sin(\pi\xi - \theta/2)$. Substituting this equation for $u(x)$ into equation 7.5 we find

$$\frac{4\pi\xi\hbar^2}{mbL} = \cot(\pi\xi + \theta/2) + \cot(\pi\xi - \theta/2) \tag{7.6}$$

which must be solved for ξ in order to determine $\psi(x)$. The discrete solutions ξ_μ (where $\mu = 0, 1, 2, \ldots$) correspond to the different energy levels of the system which are given by $E_\mu = \xi_\mu^2 E_0$.

When $\theta = \pi$ (i.e. the barrier rotates around the circumference of the ring at angular velocity $\omega = h\pi/(mL^2)$) equation 7.6 becomes

$$\frac{2\pi\hbar^2\xi_\mu}{mLb} = -\tan(\pi\xi_\mu). \tag{7.7}$$

Here, however, one of the solutions has disappeared (it has been squeezed into the discontinuity of the tan function) meaning the above equation gives solutions for odd values of μ only. The lost solution is recovered by realising $\psi(x)$ of these lost solutions has a node at the barrier (i.e. at $x = 0$), meaning they are unaffected by the barrier. It was shown in reference [111] the ground state of the system is therefore given by $\psi(x) = e^{i2\pi x/L} - 1$ which is a sine function meaning we have the required node at $x = 0$. The energy of this state is $E = E_0/4$. The general solution for even values of μ was shown to be $\xi_\mu = \mu + 1/2$.

The $e^{i2\pi x/L}$ part of the ground state wavefunction has angular momentum $\hbar$

and the -1 part has angular momentum 0. We wish to create a superposition of these two momentum modes which means we require some coupling to exist between them. This coupling is achieved through the barrier. We have previously said states with nodes at $x = 0$ do not interact with the barrier. This is because the barrier is described by a delta function. In reality, however, all barriers have some width. Consequently the wavefunction will have some (small) amplitude across the barrier and as such there will be some slight interaction. As can be seen from equation 7.1 the barrier acts to couple states with different angular momentum. At $\theta = \pi$ the ground state of the system is in either the 0 or $\hbar$ angular momentum state and as such the barrier acts to couple these two momentum modes. So by adiabatically changing the barrier rotation rate from 0 to $h\pi/(mL^2)$ a 50:50 superposition of the two angular momentum states is therefore created.

We also note that in an experiment θ is likely to deviate slightly from π. These deviations will be small meaning $\psi(x) \approx e^{i2\pi x/L} - 1$. Nevertheless as θ moves away from π the two parts of the wavefunction will no longer have the same amplitude as the system begins to favour one momentum mode over the other. This means $\psi(x)$ will no longer be a sine function and as such it will have amplitude at $x = 0$ thereby allowing coupling between the two momentum modes. So whilst the ground state interacts only slightly with the barrier these interactions are possible both due to the fact that in reality all barriers have some width and the fact that θ cannot be exactly π in an experiment.

Whilst we are primarily interested in the ground state of the system we note that when $\theta = \pi$ the first excited state when $b = 0$ is given by $\psi(x) = e^{i2\pi x/L} + 1$. This is a cosine function meaning that under these conditions the first excited state has a peak at $x = 0$ indicating that it will interact strongly with a small barrier. The energy of this state is $E = E_0/4$ making it and the ground state degenerate at $\theta = \pi$ and $b = 0$. However as b is increased more energy is transferred to the excited state from the barrier than to the ground state since the excited state has a larger amplitude across the barrier. The degeneracy of the ground and first excited state

is therefore removed for $b > 0$.

So far we have only considered a single particle system. We have shown that in this experimental set-up the particle can be made to be in a superposition where its angular momentum is 0 and $\hbar$ by rotating a small barrier at $\omega = h\pi/(mL^2)$. For $N > 1$, however, things become more complicated as the ground state contains many different momentum configurations. In fact, it contains all $|n, N-n\rangle$ configurations (where the terms in the ket represent the number of atoms with 0 and $\hbar$ angular momentum respectively and n can take any value between 0 and N) at $\theta = \pi$. We will now see how this alters our ability to create superposition states.

Let us first consider how to create a multi-particle NOON state, that is, we want a superposition of all N atoms having 0 angular momentum and all having $\hbar$ angular momentum. In order to ensure the atoms in the ground state all have 0 or all have $\hbar$ angular momentum we must raise the energy of states where particles are distributed between the two momentum modes. This is achieved using the inter-particle interactions. From equation 7.1 we see H_I can be written as

$$H_I = \frac{g}{2L}\left(\hat{n}_0(\hat{n}_0 - 1) + \hat{n}_1(\hat{n}_1 - 1) + 4\hat{n}_0\hat{n}_1\right) \tag{7.8}$$

when only the $k = 0$ and $k = 1$ modes are occupied, as is the case in the ground state at $\theta \approx \pi$ when coupling to other angular momentum modes is weak i.e. when g is small (here $\hat{n}_k = a_k^\dagger a_k$). The interaction energy of the general $|n, N-n\rangle$ state is therefore given by $E_{n,N-n} = g(N(N-1) + 2n(N+n))/(2L)$ from which it is clear different values of n result in different energies. In particular, we see the energy is maximised when $n = N/2$ and minimised when $n = 0$ or N. Consequently by introducing small interactions, the degeneracy of the $|N, 0\rangle$ and $|0, N\rangle$ states with states where particles are distributed between the two momentum modes is lifted.

For a certain critical interaction strength it has been shown [111, 112] that the ground state is in a superposition of the form $(|N, 0\rangle + |0, N\rangle)/\sqrt{2}$ i.e. a NOON state. This critical interaction strength finds a balance between the need to increase g so as to lift the degeneracy with the need to keep g small so as to prevent couplings

to other momentum modes because, as can be seen from equation 7.1, interactions act to couple states with the same total angular momentum, thereby allowing the atoms to populate momentum modes other than $k = 0$ and $k = 1$. For example, the $|0, N, 0\rangle_{-1,0,1}$ is coupled to the $|1, N-2, 1\rangle_{-1,0,1}$ through the operation $a^\dagger_{-1}a^\dagger_1 a_0 a_0$ which is allowed by equation 7.1. Therefore as g is increased the NOON state structure is lost as states other than $|N, 0\rangle_{0,1}$ and $|0, N\rangle_{0,1}$ gain amplitude. The total angular momentum of the system, however, remains constant as interactions conserve angular momentum.

In the limit of infinite short range repulsive interactions the atoms can no longer pass one another and a Tonks-Girardeau (TG) gas is formed. In the TG regime it is said the atoms have undergone fermionisation as their energy spectrum is identical to that of non-interacting fermions [113]. The atoms can, however, have the same angular momentum. In a TG gas the single-particle momentum distribution spreads out over an infinite range [114]. These features of the TG gas have already been confirmed experimentally [115, 116].

It was shown in reference [111] that in this limit of infinite short range interactions a superposition of the form $|\psi_{\mathrm{TG}}\rangle = (|0\rangle + |N\rangle)/\sqrt{2}$ is created (where the terms in the ket represent the total angular momentum of the system divided by $\hbar$). This occurs, as although the momentum of the individual atoms can spread over an infinite number of momentum modes, the total momentum of the system must be conserved meaning the superposition of 0 and $N\hbar$ angular momentum remains from the NOON state. The structure of the state, however, is drastically altered as every $|K\rangle$ consists of different configurations of states with total angular momentum $K\hbar$. For example, $|0\rangle$ contains states of the form $|\ldots, n/2, N-n, n/2, \ldots\rangle_{-1,0,1}$ and $|\ldots, N, \ldots\rangle_0$ amongst many others. We therefore write $|K\rangle = \sum_{\vec{n}_K} C_{\vec{n}_K} |\vec{n}_K\rangle$ where $|\vec{n}_K\rangle = \prod_k (a^\dagger_k)^{n_k}/\sqrt{n_k!}|\mathrm{vac}\rangle$ and $\sum_k n_k k = K$. In contrast to the NOON state, the TG cat state can be created for large N [111, 112] which is promising for its use in precision measurement schemes.

We also note that, as one would expect, when there are no interactions ($g = 0$)

the particles behave completely independently of one another and the state of the system is therefore $|\psi_{\mathrm{U}}\rangle = (a_0^\dagger + a_1^\dagger)^N/\sqrt{2^N}|\mathrm{vac}\rangle$, or equivalently,

$$|\psi_{\mathrm{U}}\rangle = \frac{1}{\sqrt{2^N}} \sum_{n=0}^{N} \binom{N}{n}^{1/2} |n, N-n\rangle_{0,1}, \tag{7.9}$$

where the terms in the ket represent the number of atoms with 0 and $\hbar$ angular momentum respectively. Here each particle is in an individual superposition of having 0 and $\hbar$ angular momentum. As can be seen from the above equation, the total angular momentum of the system therefore has a binomial distribution.

During the course of this chapter we compare the precision of each of these three states both in the presence of and the absence of particle losses. We find that whilst the precision achieved by the NOON and TG cat state is equivalent in the idealised setting, the precision capabilities of the TG cat state drastically outperform those of the NOON state when particle losses are accounted for. In fact, the TG cat state allows for precisions better than the classical initial state for all loss rates. First, however, we describe how the system can be used to make rotation measurements.

7.3 Measuring the rotation

A schematic of the measurement scheme is given in figure 7.2. It shows the five different stages involved in the measurement procedure each of which we now describe.

Step 1 corresponds to the creation of the initial state (either the TG cat state, the NOON state or the unentangled state) and has already been described. Immediately after the creation of the initial state the states of the system are degenerate and therefore the system will not change until the barrier's rotation rate is altered as indicated by step 2. The additional rotation we wish to measure, $\delta\omega$, is then non-adiabatically applied to the loop (by quickly altering the rate of rotation of the barrier from $\pi h/(mL^2)$ to $(\delta\omega + \pi)h/(mL^2)$). The momentum states are then no

longer degenerate and the Hamiltonian describing the system becomes

$$H' = \sum_{k=-\infty}^{\infty} E_0 \left(k - \frac{1}{2} + \frac{\delta\theta}{2\pi}\right)^2 a_k^\dagger a_k \tag{7.10}$$

where for now we have ignored the H_I and H_B terms since the barrier height is small and interactions do not couple states of different total angular momentum or change $|K\rangle$ when the rotation rate is changed.[1] The additional rotation therefore changes the energy of different states according to $H'|\Psi\rangle = E|\Psi\rangle$ where

$$E = E_0 \sum_{k=-\infty}^{\infty} \left(k - \frac{1}{2} + \frac{\delta\theta}{2\pi}\right)^2 n_k \tag{7.11}$$

and n_k is the number of atoms with momentum $k\hbar$. If we let the system evolve under the influence of $\delta\omega$ for time t the NOON state becomes

$$|\psi(\delta\theta)_{\mathrm{NOON}}\rangle = \frac{1}{\sqrt{2}}\left(|N,0\rangle + e^{-iE_0\delta\theta Nt/(\pi\hbar)}|0,N\rangle\right) \tag{7.12}$$

where a global phase has been ignored. Using the previously introduced equation $F_Q = 4[\langle\psi'|\psi'\rangle - |\langle\psi'|\psi\rangle|^2]$ we find

$$F_{Q_{\mathrm{NOON}}} = \left(\frac{E_0 Nt}{\pi\hbar}\right)^2. \tag{7.13}$$

Similarly the additional rotation causes the unentangled state to acquire a phase transforming $|\psi_{\mathrm{U}}\rangle$ to

$$|\psi(\delta\theta)_{\mathrm{U}}\rangle = \frac{1}{\sqrt{2^N}} \sum_{n=0}^{N} \binom{N}{n}^{1/2} e^{iE_0\delta\theta nt/(\pi\hbar)}|n, N-n\rangle \tag{7.14}$$

resulting in $F_{Q_{\mathrm{U}}} = (E_0 t/(\pi\hbar))^2 N$. And so, as expected, the NOON state has $1/\sqrt{N}$ better precision than the unentangled state in the idealised system. We now wish to determine the precision of the TG cat state.

[1] We have confirmed the final result of this section holds when H_I and H_B are accounted for numerically.

Using the relation $H'|\vec{n}_K\rangle = E_{\vec{n}_K}|\vec{n}_K\rangle$ we find

$$\begin{aligned} E_{\vec{n}_K} &= \sum_k E_0 \left(k - \frac{1}{2} + \frac{\delta\theta}{2\pi}\right)^2 n_k \\ &= E_0 \left[\left(\frac{\delta\theta}{2\pi} + \frac{K}{N} - \frac{1}{2}\right)^2 N + \text{const.}\right] \end{aligned} \tag{7.15}$$

where const. $= \sum_k n_k k^2 - K^2/N$. This means every $|\vec{n}_K\rangle$ acquires a phase of the form $e^{-iE_{\vec{n}_K}t/\hbar}$ and consequently $|\psi_{\text{TG}}\rangle$ becomes

$$|\psi_{\text{TG}}(\delta\theta)\rangle = \frac{1}{\sqrt{2}}(|\tilde{0}\rangle + e^{-iE_0 N\delta\theta t/(\pi\hbar)}|\tilde{N}\rangle) \tag{7.16}$$

where a global phase has been ignored and the tildes account for the constant phase factors picked up by the $|\vec{n}_K\rangle$ terms. At this point we calculate the F_Q and find

$$F_Q = \left(\frac{E_0 N t}{\pi\hbar}\right)^2 \tag{7.17}$$

which is exactly the same as for the NOON state. This F_Q means the uncertainty in our measurement of $\delta\omega$ is

$$\Delta(\delta\omega) = \frac{h}{mL^2}\frac{\pi\hbar}{E_0 N t} = \frac{1}{Nt} \tag{7.18}$$

and so we see that, through the use of multiple momentum modes, the TG cat state can achieve the same measurement precision as the two-mode NOON state in the idealised set-up.

It should be noted that this scheme relies on the application of $\delta\omega$ being confined to time t. This could be achieved by creating the initial state with the system's rotation axis perpendicular to the rotation axis we wish to measure. The system could then be non-adiabatically evolved in such a way that its rotation axis became parallel to the rotation axis we wish to measure. It would then be left in this configuration for time t.

Although the primary concern of this thesis is to determine the best initial state

to make precision measurements and as such we are not generally concerned with read-out methods it is worth noting that a possible way to read-out the phase difference here is to non-adiabatically remove $\delta\omega$, leaving the barrier rotating at its original rate of $h\pi/(mL^2)$. The rotation rate would then be adiabatically reduced to a point where the ground and first excited states are $|0\rangle$ and $|N\rangle$ respectively. Finally the trapping potential would be removed and the condensate imaged. The final state of the system, which depends on $\delta\omega$, is then determined from the spread in the radial distribution of the condensate. By repeating the scheme many times, each time recording the final angular momentum of the system $\delta\omega$ can be determined. Figure 7.2 summarises the 5 steps of the scheme.

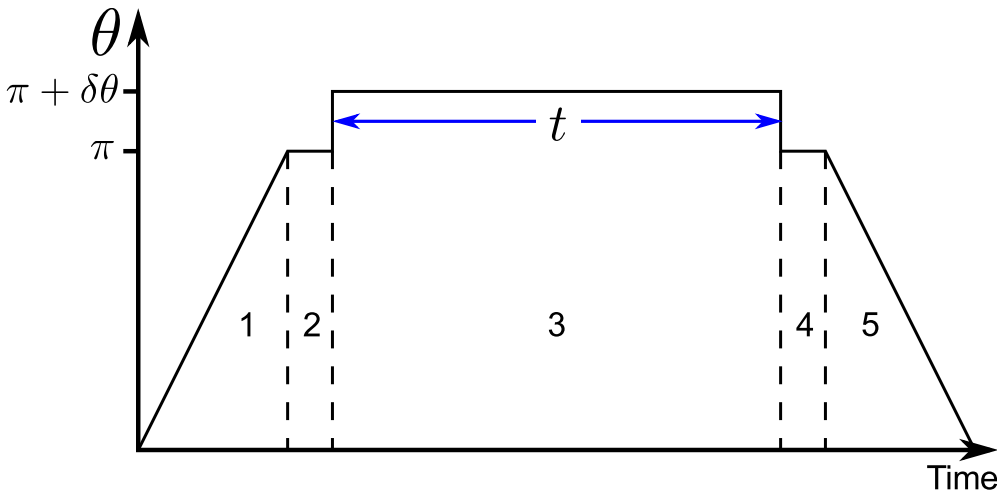

Figure 7.2: A step-by-step representation of the scheme. Step 1 is the state creation process, step 2 shows that the state of the system then remains unchanged until the barrier rotation rate is altered, step 3 shows the application of the additional rotation for time t. Steps 4 and 5 then undo steps 1 and 2 and are analogous to the second beamsplitter in a MZI.

7.4 Sensitivity

As in the previous chapter we wish to compare the sensitivity of this device with that of current atomic gyroscopes. Consequently we must take into account the number of runs, ν required to determine $\delta\omega$. With each run the precision improves as $1/\sqrt{\nu}$, yet the more runs the longer the total integration time $\tau = \nu t$. Therefore,

using equation 7.18, we find

$$\Delta(\delta\omega) = \frac{1}{Nt\sqrt{\nu}} = \frac{S}{\sqrt{\tau}} \tag{7.19}$$

where S, the short term sensitivity, is given by $S = 1/(N\sqrt{t})$. In order to match the sensitivities of current atomic gyroscopes [107] we therefore require $N \sim 10^8$ for $t = 1$s. This is still a relatively large particle flux. The sensitivity could, however, in theory be improved using superpositions that involve larger total angular momentum states.

7.5 Precision capabilities in the presence of particle loss

Whilst the NOON and TG cat state allow for the same measurement precision in the idealised system we will now show that the TG cat state is capable of much more precise measurements in the presence of particle loss. We consider the case of equal rates of loss from each momentum mode as there is no reason to presume the rate of loss from one mode is different from any other. We first describe the effects of loss on a general system with M modes and then apply the results to our rotating ring potential system.

As before, particle losses can be modelled by placing an imaginary beam splitter with transmissivity η_k, in each of the M modes. However, it was shown in Chapter 3 that this is equivalent to using a master equation of the form

$$\begin{aligned}\dot{\rho}(t) &= \frac{\Gamma_0}{2}(2a_0\rho(t)a_0^\dagger - a_0^\dagger a_0\rho(t) - \rho(t)a_0^\dagger a_0) \\ &+ \frac{\Gamma_1}{2}(2a_1\rho(t)a_1^\dagger - a_1^\dagger a_1\rho(t) - \rho(t)a_1^\dagger a_1) + \ldots \\ &+ \frac{\Gamma_{M-1}}{2}(2a_{M-1}\rho(t)a_{M-1}^\dagger - a_{M-1}^\dagger a_{M-1}\rho(t) - \rho(t)a_{M-1}^\dagger a_{M-1})\end{aligned} \tag{7.20}$$

which for equal rates of loss from each mode simplifies to

$$\dot{\rho}(t) = \Gamma\sum_k (a_k\rho(t)a_k^\dagger - \hat{n}_k\rho(t)) \tag{7.21}$$

where $\hat{n}_k = a_k^\dagger a_k$ is the number operator of mode k and the sum is over all possible modes. We now solve this model by separating ρ into $N+1$ sections where each section has the same particle number,

$$\rho(t) = \sum_{l=0}^{N} y^{(N-l)}(t)\rho^{(N-l)}. \tag{7.22}$$

Here $\rho^{(N-l)}$, which is constant in time, is a section of the whole density matrix with $N-l$ particles (i.e. l particles have been lost to the environment) and $y^{(N-l)}(t)$ is a time dependent coefficient. We can split the density matrix up in this manner as each $\rho^{(N-l)}$ is represented in an orthogonal subspace.

Differentiating equation 7.22 we see

$$\begin{aligned}\sum_{l=0}^{N} \dot{y}^{(N-l)}(t)\rho^{(N-l)} &= \Gamma \sum_k (a_k \rho(t) a_k^\dagger - \hat{n}_k \rho(t)) \\ &= \Gamma \sum_{l=0}^{N} (N-l) y^{(N-l)}(t) \left(\rho^{(N-l-1)} - \rho^{(N-l)}\right)\end{aligned} \tag{7.23}$$

where

$$\rho^{(N-l-1)} = \frac{1}{N-l} \sum_k a_k \rho^{(N-l)} a_k^\dagger. \tag{7.24}$$

In the latter of the two equations we have used the fact that $\mathrm{Tr}(\sum_k a_k \rho^{(N-l)} a_k^\dagger) = \sum_k \mathrm{Tr}(\hat{n}_k \rho^{(N-l)}) = N-l$ to normalise $\rho^{(N-l-1)}$ to 1. Equating coefficients of $\rho^{(N-l)}$ we find

$$\dot{y}^{(N-l)}(t) = \Gamma \left[(N-l+1)y^{(N-l+1)}(t) - (N-l)y^{(N-l)}(t)\right] \tag{7.25}$$

which has solution

$$y^{(N-l)}(t) = \binom{N}{l} \eta^{N-l}(1-\eta)^l \tag{7.26}$$

where $\eta = e^{-\Gamma t}$. The total density matrix of the system at time t is therefore

$$\rho(t) = \sum_{l=0}^{N} \binom{N}{l} \eta^{N-l}(1-\eta)^l \rho^{(N-l)}. \tag{7.27}$$

As mentioned in Chapter 3, for a system consisting of X orthogonal subspaces

the total F_Q of the system is the sum of the F_Q of each of the X individual subspaces. The total F_Q of this system for loss rate η is therefore

$$F_{Q_\eta} = \sum_{l=0}^{N} \binom{N}{l} \eta^{N-l}(1-\eta)^l F_Q^{N-l} \tag{7.28}$$

where F_Q^{N-l} is the F_Q of $\rho^{(N-l)}$ which is calculated using the relationship $F_Q^{N-l} = \mathrm{Tr}[\rho^{(N-l)}A^2]$. So F_{Q_η} is easily determined for all η providing the $N+1$ values of F_Q^{N-l} are known.

For an unentangled initial state we know $F_Q^N \propto N$. The loss of a single particle has no influence on the remaining $N-1$ particles and therefore $F_Q^{N-l} \propto (N-l)$. The total F_Q for a given rate of loss is therefore $F_{Q_\eta} \propto N\eta$. In contrast, however, the loss of a single particle from a NOON state completely destroys the superposition meaning $F_Q^{N-l} = 0$ for all l except $l = 0$ giving $F_{Q_\eta} \propto N^2\eta^N$. The effects of loss on the TG cat state are numerically compared with the NOON and unentangled initial states in figure 7.3. All numerical simulations use a truncated angular momentum basis of 18 modes. In order to account for this the interaction strength was rescaled as described in reference [111]. Here it was shown that, after rescaling, the error produced by using a truncated basis was, at worst, 3% which was a factor of 8 times smaller than without the rescaling.

We see, as expected, the NOON and the TG cat state offer the same precision when there is no loss, $\eta = 1$, and the precision of the unentangled state is much worse. As demonstrated previously, when η decreases the precision capabilities of the unentangled state soon outperform those of the NOON state. Importantly, however, the TG cat state outperforms the unentangled state for all loss rates and therefore could prove extremely valuable to the metrology community.

Recently there has been much interest in finding a balance between the need for quantum correlations to make precise measurements with the need for robustness to particle loss. With this goal in mind references [1, 2] found the theoretical optimal state for two-mode interferometry in the presence of particle loss, that is, the initial

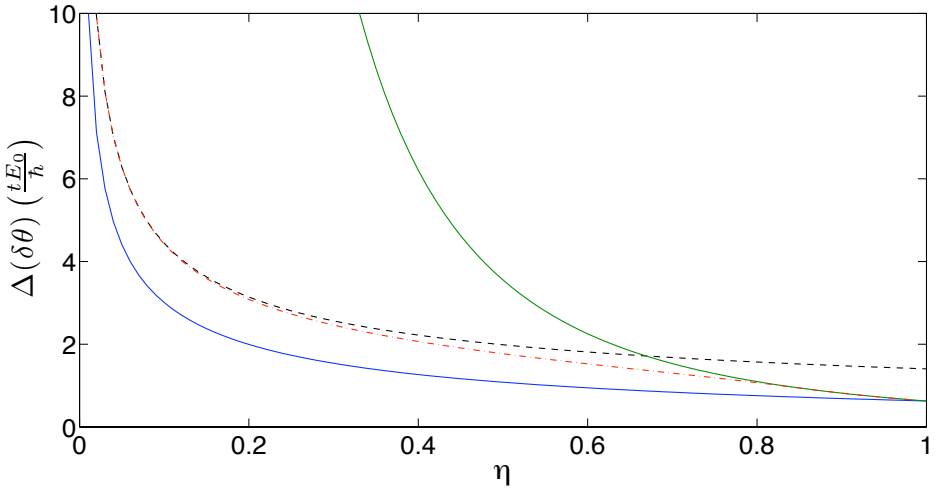

Figure 7.3: The uncertainty in $\delta\theta$ for equal rates of loss from all momentum modes for $N = 5$. The green solid line shows the precision of the NOON state, the black dashed line shows the unentangled initial state, the red dashed-dotted line shows the optimal two-mode state and the solid blue line shows the TG cat state. The TG plot is for $b/L = 0.008E_0$ (i.e. a small barrier) and $g/L = 1085/(2\pi)E_0$ (i.e. deep in the TG regime).

state that affords the best precision for a particular amount of loss. The precision of the optimal two-mode initial state is shown in figure 7.3 (red dashed-dotted line).[2] It is immediately clear that the TG cat state outperforms the precision capabilities of the two-mode optimal initial state for all loss rates. Not only this, the optimal two-mode initial state very much depends on the amount of loss as the structure of the state changes with η thereby making its experimental implementation difficult.

The TG cat state has therefore provided a clear demonstration of how, by spreading particle observables over many modes rather than just two, precise and robust phase measurements can be made. To our knowledge no state has yet matched the robustness of unentangled particles and as such unentangled states are the most practical choice for phase measurements in a laboratory. However, the TG cat state has demonstrated similar robustness to particle loss as the two-mode unentangled

[2]Note that the optimal state is calculated using an upper bound to the true F_Q and as such the true optimal two-mode state will have slightly worse precision. However, as discussed in [2] the difference between the precision of the upper bound optimal initial state and the true optimal initial state will be small. Also the fact that the optimal two-mode state is determined using an upper bound only strengthens our argument that the TG cat state far outperforms the two-mode optimum for all loss rates.

state whilst achieving Heisenberg limited precision in the idealised set-up. It therefore has the potential to alter the way precision measurements are made.

7.6 The effects of using an imperfect TG cat state

So far we have shown that the TG cat state acts as an ideal initial state for precision measurements. Its production, however, requires large interactions (g) and a small barrier height (b). We therefore wish to investigate what happens to the precision of our measurements if g and b are not exactly as required to create the TG cat state. We do this by determining the F_Q for different values of b and g as shown in figure 7.4. For now we consider only the idealised system in which no particles are lost, however an interesting avenue for future research would be to investigate the effects on F_Q of varying b and g for different rates of loss. As expected F_Q for small b and large g (TG cat regime) is given by $(NE_0t/(\pi\hbar))^2$. This value holds well for increasing barrier height and decreasing interaction strength. Eventually, however, there comes a point after which the barrier is too high and the interactions are too small to give Heisenberg limited measurements.

This is because as the interaction strength is decreased the quantum correlations between the atoms are reduced and they behave more independently of one another. When there are no interactions the atoms behave completely independently and the precision therefore scales as $1/\sqrt{N}$. As the barrier height increases the coupling between states of different total angular momentum is increased therefore preventing the creation of a TG cat state, again leading to less precise measurements. Importantly, however, we see that the scheme holds its Heisenberg limited precision well for moderate interaction strength and barrier height. Therefore, we conclude that as long as the initial state, $|\psi(0)\rangle$, is close in form to that of the TG cat state the precision of the system is not significantly altered.

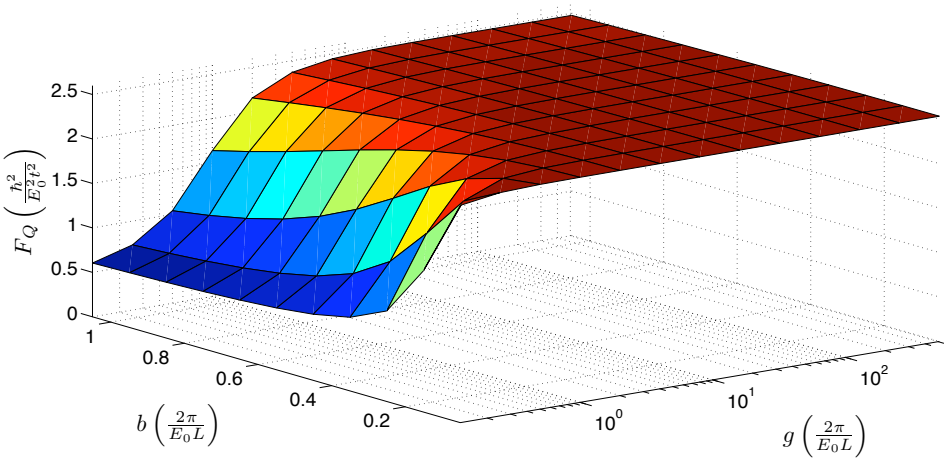

Figure 7.4: F_Q for different values of barrier height and interaction strength for $N = 5$ ($M = 18$). The optimum initial state is found when the barrier is small and the interactions are large. However, for moderate variations in b and g away from their optimum values, F_Q is not significantly altered. This means the system will hold its precision well in experiments where exact values of b and g cannot be assured.

7.7 Conclusion

To conclude we have shown how by spreading particle observables over many momentum modes, rather than just two, rates of rotation can be measured with the same precision as that achieved using a two-mode NOON state in an idealised set-up. The multimode TG cat state has been shown, however, to be much more robust to the effects of particle loss than the NOON state. In fact the TG cat state was shown to achieve precisions better than an unentangled two-mode state for all loss rates. Perhaps even more importantly, its precision capabilities outperform the two-mode theoretical optimum state for all η. This work is of fundamental importance because it has demonstrated an experimentally feasible way to make highly precise and robust rotation measurements.

Chapter 8

Optimising initial states in the presence of loss: The general case

The focus of this thesis thus far has been developing ways to improve the precision of rotation measurements by optimising the initial state of a lossy gyroscope scheme. In particular, the central theme has been finding states that allow for (close to) Heisenberg limited precision in an idealised setting yet that are robust to the effects of particle loss. As previously mentioned there has been a recent flurry of interest in finding a balance between the need for phase sensitivity and the need for robustness to loss of general measurement schemes [1, 2, 74, 75, 117, 118] as quantum correlations are required to push the precision of current measurement schemes any further. One particularly interesting result is the demonstration of a theoretical optimum initial state for a lossy two-mode general measurement scheme [1, 2] (first introduced in Chapter 7 - see figure 7.3).

In this chapter we turn our attention to general phase measurement schemes (i.e. the schemes we consider are no longer specific to rotations) and discuss, in detail, the origin of the theoretical optimum of references [1, 2]. We describe an experimentally accessible scheme we have developed that is capable of achieving precisions close

to that of this optimum state. We also discuss multipath interferometry and show how multipath devices can be used to improve measurement precision. This is still very much work in progress. Here we present just one advantage of multipath interferometers but it is expected that many more interesting advantages will be found as this work progresses.

8.1 A review of lossy two-mode interferometry

The effects of particle loss on different initial states was discussed in detail in references [1, 2]. They considered a general lossy two-mode measurement scheme that consisted of some state creation process, the application of a relative phase ϕ between the two modes (paths 0 and 1) followed by a state detection and readout procedure (see figure 3.6). Losses were modelled by placing imaginary beam splitters with transmissivities η_0 and η_1 on paths 0 and 1 respectively. The F_Q of different initial states for different loss rates (different values of $\eta_{0,1}$) was determined and the best state for a particular loss rate was taken to be the one with the largest F_Q since $\Delta\phi \geq 1/\sqrt{F_Q}$.

We have previously shown that the F_Q for the general initial state $|\psi_{in}\rangle = \sum_{n=0}^{N} \beta_n |n, N-n\rangle$ and a particular loss rate is given by

$$F_Q = \sum_{l=0}^{N} F_Q \left[\sum_{l_0=0}^{l} p_{l_0,l-l_0} |\xi_{l_0,l-l_0}(\phi)\rangle\langle\xi_{l_0,l-l_0}(\phi)| \right] \tag{8.1}$$

where

$$|\xi_{l_0,l-l_0}\rangle = \frac{1}{\sqrt{p_{l_0,l-l_0}}} \sum_{k=l_0}^{N-(l-l_0)} \beta_n e^{in\phi} \sqrt{B^n_{l_0,l-l_0}} |n-l_0, N-n-(l-l_0)\rangle \tag{8.2}$$

and

$$B^n_{l_0,l-l_0} = \binom{n}{l_0} \binom{N-n}{l-l_0} \eta_0^n (\eta_0^{-1}-1)^{l_0} \eta_1^{N-n} (\eta_1^{-1}-1)^{l-l_0}. \tag{8.3}$$

When the loss is limited to just one path (i.e. $\eta_1 = 1$), as is common in experiments since the phase shifter itself is often the greatest cause of particle loss, this equation

can be simplified to

$$F_Q = 4\left(\sum_{n=0}^{N} n^2 x_n - \sum_{l=0}^{N} \frac{\left(\sum_{n=l}^{N} x_n n B_{l0}^n\right)^2}{\sum_{n=l}^{N} x_n B_{l0}^n}\right) \tag{8.4}$$

where $x_n = |\beta_n|^2$. Here we have made use of the fact, that because the particles are only lost from one mode, we can write the state of the system after loss as

$$\rho(\phi) = \sum_{l=0}^{N} p_{l,0} |\xi_{l,0}(\phi)\rangle\langle\xi_{l,0}(\phi)|. \tag{8.5}$$

Since each of the $N+1$ $|\xi_{l,0}(\phi)\rangle$ states contain a different total number of particles they are orthogonal and the total F_Q of the system can therefore be found using the relation of equation 3.28. This says that the total F_Q of a system is the sum of the F_Q of all the orthogonal subsystems the total system is composed of multiplied by the probability of being in that subsystem. Determining the F_Q of each subsystem using the equation for the F_Q of a pure state (equation 3.27) results in equation 8.4.

The same simplification is not, however, possible for the case of loss on both paths since, for a given $l = l_0 + l_1$, the $|\xi_{l_0,l_1}(\phi)\rangle$ are not necessarily orthogonal. This is due to the fact that we cannot know how many particles were lost from which path. Nevertheless for NOON states this does not matter since the loss of only a single particle automatically destroys the superposition and prevents the readout of any phase information. Similarly for an unentangled initial state the origin of the lost particle is irrelevant because as soon as the particle is lost that single-particle superposition is destroyed.

As was shown in Chapter 3 it is therefore possible to determine a simple relationship between F_Q and $\eta_{0,1}$ for a NOON and unentangled initial state. To recap these relationships are

$$F_{Q_{NOON}} = \frac{2N^2 \eta_0^N \eta_1^N}{\eta_0^N + \eta_1^N} \tag{8.6}$$

and

$$F_{Q_U} = \frac{2N\eta_0\eta_1}{\eta_0 + \eta_1}. \tag{8.7}$$

For all other states, however, when particles are lost from both modes, the F_Q must be determined using equation 8.1 which involves solving a complicated eigenvalue problem that is not feasible analytically. Therefore these calculations must be completed numerically.

Equations 8.6 and 8.7 are for a balanced NOON state (i.e. $(|N,0\rangle + |0,N\rangle)/\sqrt{2}$) and a balanced unentangled state (i.e. the output of a 50:50 beam splitter into which $|N,0\rangle$ is inputted). However it was shown in reference [2] that the precision capability of the NOON state can be improved by optimising the coefficients of $|N,0\rangle$ and $|0,N\rangle$, that is, instead of setting both coefficients to $1/\sqrt{2}$ we instead have $\sqrt{x_N}|N,0\rangle + \sqrt{x_0}|0,N\rangle$ where x_0 and x_N change with $\eta_{0,1}$ and $x_0 + x_N = 1$.

We determine the F_Q of this unbalanced NOON state for different values of $\eta_{0,1}$ using the same procedure as used in Chapter 3 to determine the F_Q of the balanced NOON state. That is, since we know that the loss of a single particle completely destroys the NOON state the only $|\xi_{l_0,l_1}(\phi)\rangle$ that contributes to F_Q is $|\xi_{0,0}(\phi)\rangle$ meaning the total F_Q of the system is

$$F_Q = p_{0,0} F_Q \left[|\xi_{0,0}(\phi)\rangle\langle\xi_{0,0}(\phi)| \right]. \tag{8.8}$$

For $|\psi_{in}\rangle = \sqrt{x_N}|N,0\rangle + \sqrt{x_0}|0,N\rangle$ we have

$$|\xi_{0,0}(\phi)\rangle = \frac{1}{\sqrt{p_{0,0}}} \left(\sqrt{x_N}\sqrt{\eta_0^N} e^{iN\phi}|N,0\rangle + \sqrt{x_0}\sqrt{\eta_1^N}|0,N\rangle \right) \tag{8.9}$$

and F_Q is therefore

$$F_Q = \frac{4N^2 x_0 x_N \eta_0^N \eta_1^N}{x_N \eta_0^N + x_0 \eta_1^N}. \tag{8.10}$$

Maximising this equation with respect to x_0 and remembering that $x_N = 1 - x_0$ we find the optimum value of x_0 is

$$x_0 = \frac{\eta_0^{N/2}}{\eta_0^{N/2} + \eta_1^{N/2}} \tag{8.11}$$

and consequently the optimum F_Q for a given rate of loss is

$$F_{Q_{NOON,max}} = \frac{4N^2\eta_0^N\eta_1^N}{(\eta_0^{N/2} + \eta_1^{N/2})^2}. \tag{8.12}$$

We note that for the case of equal loss on both paths ($\eta_0 = \eta_1 = \eta$) this gives $x_0 = x_N = 1/2$ independent of the rate of loss and $F_Q = N^2\eta^N$.

Similarly, recognising that an unentangled initial state is simply N copies of a single-particle NOON state, the coefficients of the unentangled initial state can be altered depending on the value of $\eta_{0,1}$ to increase the F_Q to

$$F_{Q_{U,max}} = \frac{4N\eta_0\eta_1}{(\sqrt{\eta_0} + \sqrt{\eta_1})^2}. \tag{8.13}$$

Here the coefficients of the unentangled state are optimised by varying the transmissivity, T, of the beam splitter into which $|N, 0\rangle$ is inputted according to the rate of loss, that is, $T = \sqrt{\eta_1}/(\sqrt{\eta_0} + \sqrt{\eta_1})$. Using the Cramér-Rao bound we find the best possible precision that can be achieved using an unentangled initial state in a lossy measurement scheme is

$$\Delta\phi_{\text{SIL}} = \frac{\sqrt{\eta_0} + \sqrt{\eta_1}}{2\sqrt{N\eta_0\eta_1}}. \tag{8.14}$$

This bound was first introduced in [2] and is called the standard interferometric limit (SIL). It is the best possible precision that can be achieved using unentangled particles in a lossy two-mode system.

References [1, 2] then went on to discuss other ways to improve precision in the presence of particle losses using different initial states. Several strategies were suggested, for example, using chopped NOON states where instead of having just one N particle NOON state it is chopped into n smaller NOON states each with N/n particles. Optimising n it was shown that this strategy beat the SIL for much higher losses than the traditional N particle NOON state, even with its optimised amplitudes.

Most significantly of all the paper went on to show how by optimising the coefficients, β_n, of $|\psi_{in}\rangle = \sum_{n=0}^{N} \beta_n |n, N-n\rangle$ it is theoretically possible to beat the SIL for almost all rates of loss. Two specific situations were considered: the case of loss on just one path, which physically corresponds to systems where the sample to be measured is responsible for the loss, and the case of equal loss on both paths. The SIL, the NOON state precision and the precision of the theoretical optimum initial state is shown for $N = 10$ in figure 8.1 for the case of loss on just the phase path and the case of equal loss on both paths [1]. It is clear that when there is no loss the optimum state affords Heisenberg limited precision and physically corresponds to a balanced NOON state, that is $\beta_n = 1/\sqrt{2}$ for $n = 0, N$ and $\beta_n = 0$ otherwise. As the rate of loss increases the optimum state deviates from a NOON state structure as coefficients other than $\beta_{0,N}$ gain amplitude, eventually approaching a classical state structure where the β_n follow a binomial distribution.

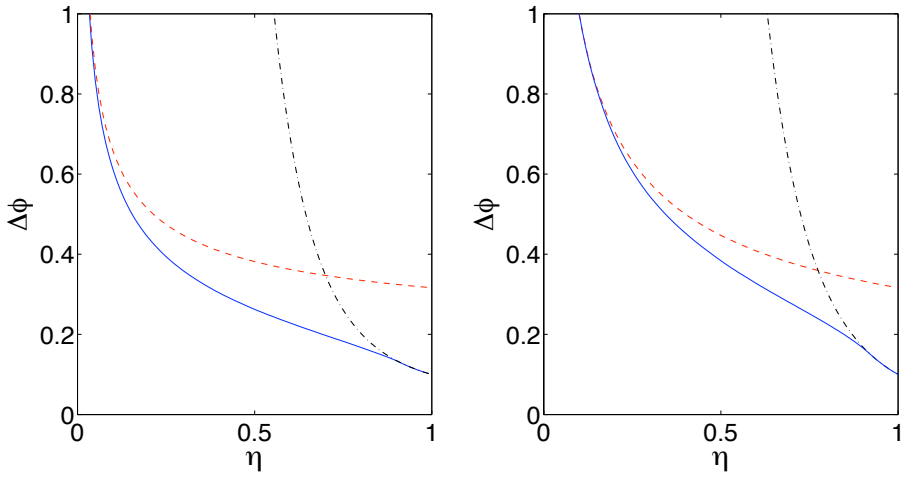

Figure 8.1: Left: Loss on just the phase path for N=10 ($\eta_0 = \eta$ and $\eta_1 = 1$). The solid blue line shows the precision of the theoretical optimum initial state, the dashed-dotted black line shows the precision of the optimised NOON state and the red dashed line is the SIL. Right: The same but for the case of equal losses on each path ($\eta_0 = \eta_1 = \eta$).

However, these optimum initial states are theoretical and are likely to prove

[1] For equal losses on both paths Dorner *et al.* determined the theoretical optimum using an upper bound on F_Q. However, the theoretical optimum initial state shown in figure 8.1 does not use this upper bound.

difficult to produce in a laboratory as their structure changes with η. A proof-of-principal demonstration of the technical feasibility of producing such states was given in reference [119] however this was for the specific case of $N = 2$ and any multiparticle implementation is likely to prove challenging. We will now demonstrate a simple way to produce states that allow for phase measurements with precisions close to that of these theoretical optimum initial states.

8.2 A scheme to improve precision in the presence of loss

8.2.1 Loss on just one path

We first consider the case of loss on just the phase path (i.e. $\eta_0 = \eta$ and $\eta_1 = 1$). As in references [1, 2] we wish to find a way to improve the precision of the lossy measurement scheme in figure 3.6 by producing an initial state $|\psi_{in}\rangle$ that allows for precise yet robust phase determination. However, we also want to find a simple way to produce $|\psi_{in}\rangle$. We find that using a beam splitter of variable transmissivity (as is required to achieve the SIL) as the state creation device and altering the number of particles incident on each of its input ports, precisions close to that of the theoretical optimum can be achieved. We shall refer to this technique as the optimising K and T method (or the KT method for short) where K refers to the number of particles incident on port one of the beam splitter and T is its transmissivity.

In the KT method the input to the state creation device is $|K, N-K\rangle$. This is then transformed by the device, which is a two-port beam splitter with transmissivity T, to

$$|\psi_{in}\rangle = \sum_{n=0}^{N} f(n)|n, N-n\rangle \tag{8.15}$$

where

$$f(n) = \sum_{y=max\{0,n-N+K\}}^{min\{K,n\}} \frac{\sqrt{K!(N-K)!n!(N-n)!}}{y!(K-y)!(n-y)!(N-K-n+y)!} \times \sqrt{T}^{N-K-n+2y}\sqrt{1-T}^{K+n-2y}(-1)^{N-K-n+y}. \tag{8.16}$$

The precision of this $|\psi_{in}\rangle$ for different loss rates, η, is determined using equation 8.4. By numerically optimising K and T for each η we find the best possible precision achievable by this method for different loss rates. The results are shown in figure 8.2 for N=10.

For the case of no loss the optimum K is $N/2$ and the optimum T is $1/2$. This results in a bat state and achieves a precision scaling of $\Delta\phi = 1/\sqrt{N(N/2+1)}$. This is Heisenberg limited and for large N is approximately only a factor of $\sqrt{2}$ worse than the NOON state [2]. For large amounts of loss, that is $\eta \approx 0$, the optimum K is N and the optimum T is $\sqrt{\eta_1}/(\sqrt{(}\eta_0) + \sqrt{(}\eta_1))$, i.e. the best possible precision is the SIL. However for the loss rates inbetween it is clear from figure 8.2 that the KT method allows for precisions better than the SIL and the bat state. In fact we see that the KT method allows for precisions very close to the theoretical optimum of references [1, 2].

Figure 8.3 shows how the KT method performs relative to the theoretical optimum for larger numbers of particles ($N = 10, 20, 30, 40$ and 50). For moderate loss rates we see that the larger N, the better the performance of the KT method relative to the theoretical optimum. For extremely high loss rates (i.e. $\eta \approx 0$) the precision capabilities of the KT method and the theoretical optimum become equivalent for all N as they both approach the SIL. For some loss rates, however, the F_Q of the KT method relative to the F_Q of the theoretical optimum worsens with increasing N. Nevertheless, this is only for relatively large amounts of loss which suggests that for most experimentally realistic loss rates the larger N the better the KT method.

We briefly note that the bat state has previously been shown to find a good

[2] Bat states can only be produced for even N, however for odd N the KT method achieves only a slightly worse precision than $1/\sqrt{N(N/2+1)}$.

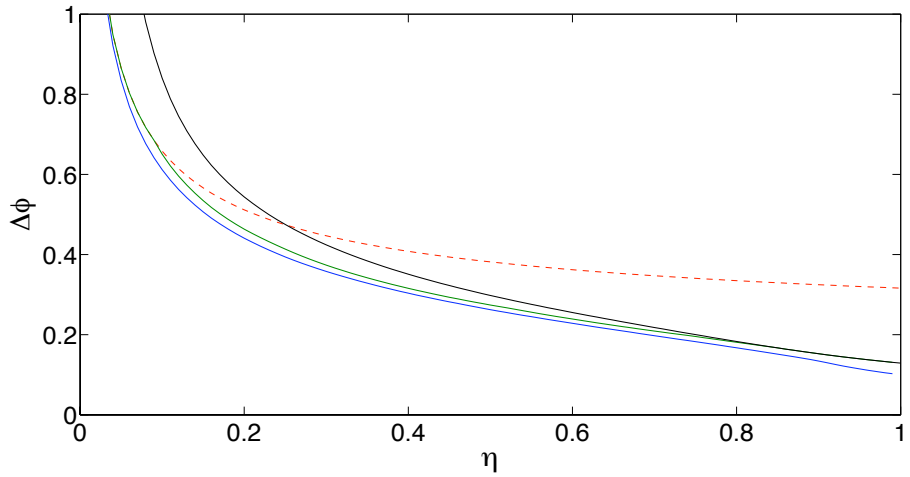

Figure 8.2: The precision of a general two-mode measurement scheme with losses on just the phase path for the theoretical optimum initial state (blue solid line), the KT method (green solid line), a bat state (black solid line) and the SIL (red dashed line). Here N=10.

balance between the need for precision and the need for robustness (see Chapter 6). We therefore wish to compare the precision of a bat state with that of the KT method for all loss rates. Figure 8.4 shows the F_Q of the KT method and that of the bat state relative to the theoretical optimum for $N = 10$. When $\eta = 1$ the F_Q of the KT method and the bat state are equivalent. However, it is clear from figure 8.4 that as the rate of loss increases the bat state rapidly begins to lose precision in comparison to the theoretical optimum. The precision of the KT method, however, steadily improves relative to that of the theoretical optimum as loss increases. Both the bat state method and the KT method use the same devices and so we see that simply by changing K and T, the phase precision can be dramatically improved.

8.2.2 Loss on both paths

Equal loss

We now want to investigate whether the KT method also achieves precisions close to that of the theoretical optimum for the case of equal amounts of loss on both paths i.e. $\eta_0 = \eta_1 = \eta$. As before the best precision achieved by the KT method is found using equations 8.1 and 8.15 and then numerically optimising K and T for

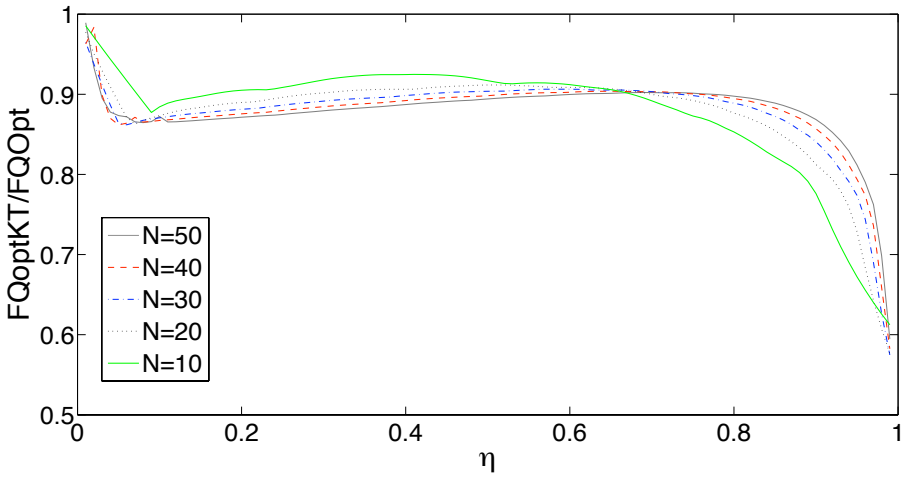

Figure 8.3: The F_Q of the KT method compared to the F_Q of the theoretical optimum initial state for the case of loss on just the phase path.

every η. The results are shown in figure 8.5. It is immediately clear that under the condition $\eta_0 = \eta_1$ the KT method is less advantageous than for the case of loss on just one path. In fact, the precision of the KT method provides almost no advantage over using a standard bat state for $\eta > 0.5$, i.e. setting $K = N/2$ and $T = 1/2$. This is because the condition that $\eta_0 = \eta_1$ means the problem is symmetric and consequently $|\beta_n| = |\beta_{N-n}|$. To satisfy this need for symmetry the optimum T is always $1/2$ meaning only K can be varied. The fact that K is a discrete quantity gives rise to the sharp kink seen in figure 8.5.

Nevertheless in a typical interferometric set-up we would expect the rate of loss on the phase path to be greater than the rate of loss on the phase free path as the phase plate itself often induces scattering effects that lead to particles being lost to the environment. As such the case of loss on just the phase path is the more experimentally realistic of the two situations considered thus far. However, it is unrealistic to discount loss on the phase free path altogether. We therefore wish to determine what happens when there is a fixed, small amount of loss on path 1.

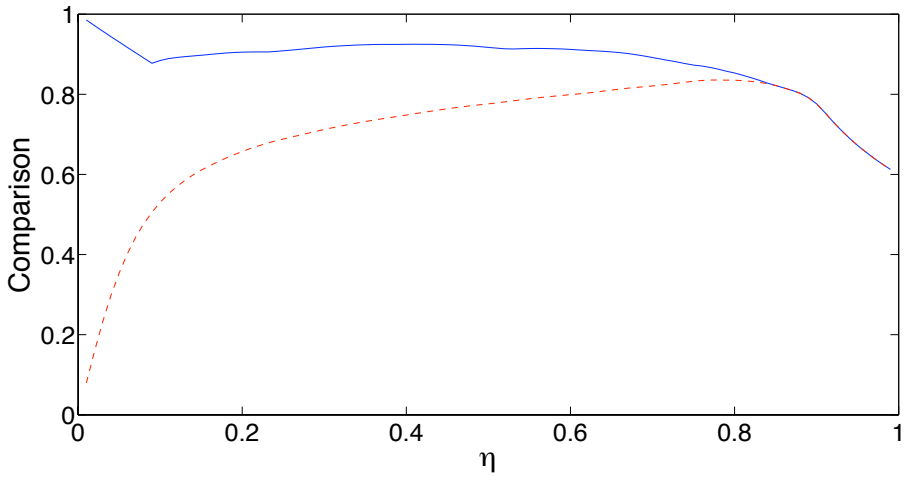

Figure 8.4: The blue solid line is F_QKT/F_QOpt for N=10. The red dashed line is F_QBat/F_QOpt for the same N. Whilst the precision capabilities of the bat state and the KT method are equivalent for small amounts of loss it is clear that as loss increases the KT method provides a significant increase in precision over the bat state.

Unequal loss

In this section we turn our attention to the experimentally realistic situation where most loss occurs on the phase path and there is a small amount of loss on the phase free path. In particular we fix the amount of loss on the phase free path and determine what happens to the precision of our phase measurements as loss on the phase path increases.

We would expect the rate of loss on the phase free path to be small, say $\eta_1 \approx 0.9$. Figure 8.6 shows the precision afforded by the KT method, a bat state and an unentangled initial state in this situation for different rates of loss on the phase path i.e. different values of $\eta_0 = \eta$ [3]. We see that in this case the precision of the KT method is, as expected, equivalent to that of the bat state for small rates of loss. However, unlike the case of equal amounts of loss on the two paths, the precision of the KT method outperforms that of the bat state for $\eta \lesssim 0.6$ and that of the unentangled state for all $\eta \gtrsim 0.2$. The KT method therefore provides a realistic way to improve the precision of current experimental schemes for η in the range 0.2 to

[3]Here we have not included the theoretical optimum initial state precision due to the numerical complexity associated with finding this state.

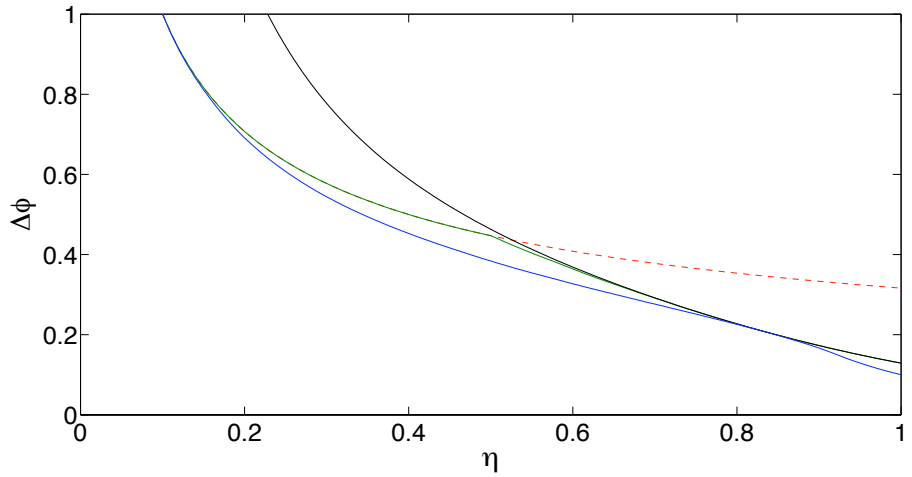

Figure 8.5: Here N=10 and $\eta_0 = \eta_1 = \eta$. The blue solid line is the precision of the theoretical optimum initial state, the green solid line is the precision of the KT method, the black solid line is the precision of the bat state and the red dashed line is the SIL.

0.6.

Figure 8.6 also shows what happens to the precisions of the various states for $\eta_1 = 0.8$ and $\eta_1 = 0.7$. Experimentally, however, we would not expect the rate of loss on path 1 to be so high. These plots have been included for completeness and to allow a rough pattern to be seen, namely, that as the rate of loss on the second path increases the advantage of the KT method over other states, such as the bat state, is reduced. This is clearly evident from figure 8.6 as the kink where the KT method and the SIL meet moves towards larger values of η (smaller loss rates) as loss on path 1 is increased.

We therefore conclude that the KT method is most advantageous when particle losses are limited to one path. As the rate of loss on the second path increases the advantage is gradually lost. However, as figure 8.6 shows, for the experimentally realistic case of small amounts of loss on the phase free path, the precision achieved by the KT method is significantly better than that of other states, such as the bat state which has previously been shown to be a good initial state for making precise and robust phase measurements. All that the KT method requires is a beam splitter of variable reflectivity and the ability to control the number of particles incident on

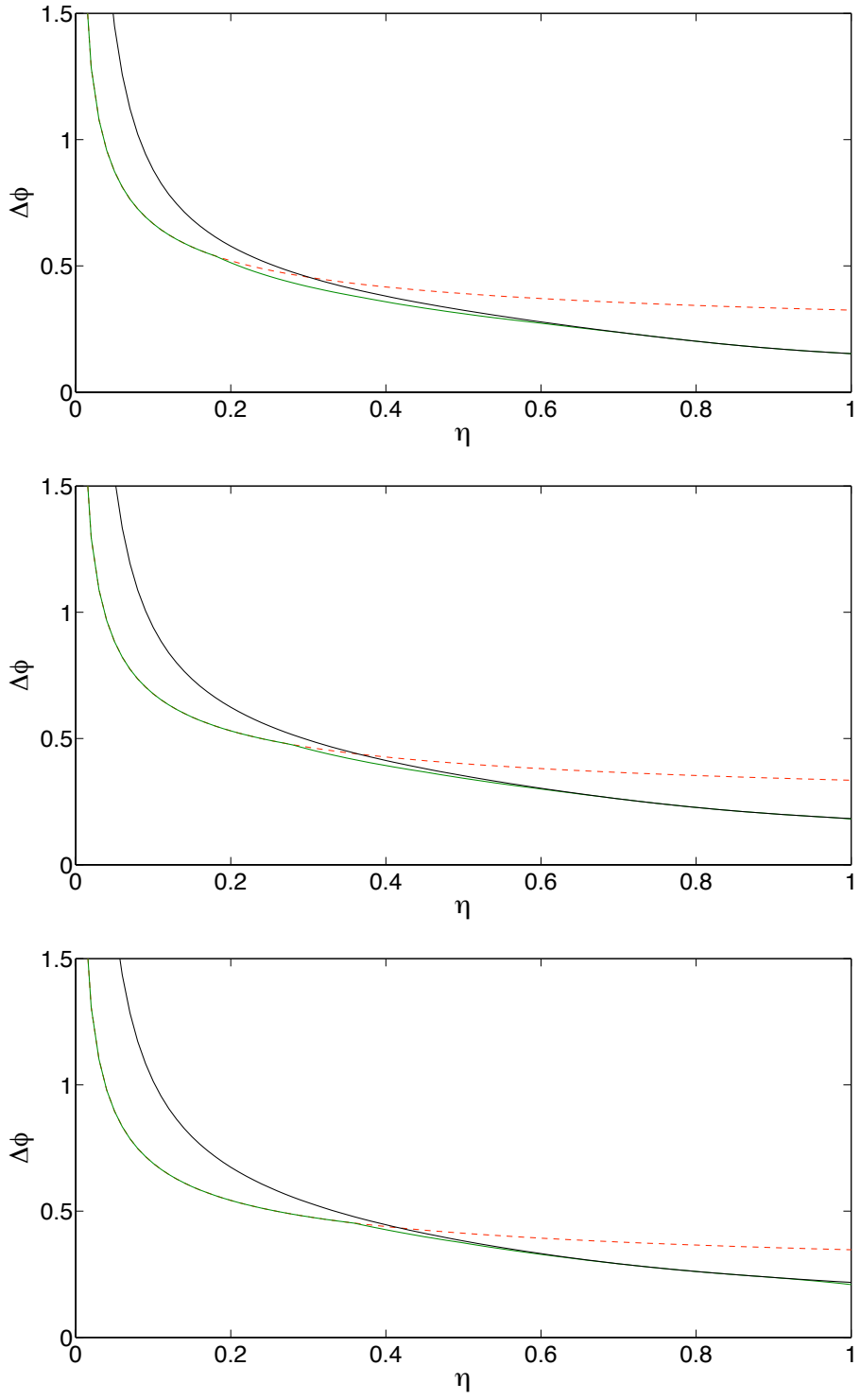

Figure 8.6: The precision of an unentangled initial state (red dashed line), a bat state (black solid line) and the KT method (green solid line) for $N = 10$. Here η is the loss on the phase path. In the top figure the loss on the phase free path (path 1) is $\eta_1 = 0.9$, in the middle figure it is $\eta_1 = 0.8$ and in the bottom figure it is $\eta_1 = 0.7$. It is clear that as the loss on path 1 increases the KT method outperforms the SIL for fewer loss rates.

each of its input ports.

8.3 Multipath interferometry

We now begin to discuss the potentials of lossy multipath interferometry for making ultra-precise and robust phase measurements. This is motivated, in part, by the fact that in Chapter 7 we saw that spreading particle observables over multiple momentum modes, rather than just two, allowed for extremely precise measurements in the presence of particle loss. Here, however, we stick to a typical interferometer set-up rather than looking at rotation measurements, as with the realisation of multiport beam splitters [91, 120], there has been a growing interest in the precision of the multipath interferometers of figure 8.7 [89, 121–123]. D'Ariano and Paris [89], for example, claimed the precision of these devices increases linearly with the number of paths M, therefore allowing for arbitrary precision for a given N. However, they considered interferometers whose phase shift increased by a constant phase, ϕ, between paths resulting in a total phase shift of $(M-1)\phi$. This meant the more paths the device had, the larger the total phase to be measured, naturally leading to better precisions for larger devices as was discussed in [123]. The fair comparison, however, seems to be between devices subjected to the same overall phase and this is the scenario that will be investigated here.

Firstly we note that, owing to the many possible configurations of a multipath interferometer, for example, the different ways ϕ can be applied, it is likely there are many more advantages to using these devices than the one discussed in this section and this will form the basis of future work. Here we restrict our discussion to the multipath interferometer configuration of figure 8.7 where the same phase, ϕ, has been applied to q paths. This physically corresponds to a placing of the phase plate across q paths rather than just one. We show that by varying q the SIL can be achieved in this multipath set-up without the need for beam splitters with variable transmissivity.

As previously discussed the SIL is the best possible precision attainable when

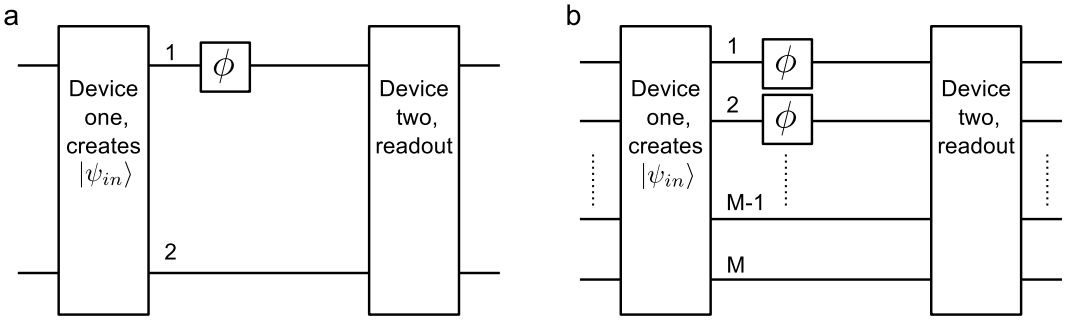

Figure 8.7: a) A two-path interferometer as before. b) A M-path interferometer with a total phase ϕ. As before the first device creates the initial state $|\psi_{in}\rangle$ and in a classical set-up would be a M-path balanced beam splitter. The second device would be a M-path balanced inverse beam splitter in the classical set-up. We choose to apply the phase to q paths.

$|\psi_{in}\rangle$ is a classical state and is achieved by inputting N particles in one port of a two-mode beam splitter of variable transmissivity. We now show how the exact same precision can be achieved using *balanced* multimode beam splitters. The operation of a M-mode balanced beam splitter is given by the unitary matrix

$$U_{jk} = \frac{1}{\sqrt{M}} \exp\left[\frac{i2\pi}{M}(j-1)(k-1)\right] \tag{8.17}$$

and for a general M-path interferometer the $1 \leq q \leq M-1$ paths each acquire a phase through the unitary transform $U_{\phi_m} = \exp(i\phi a_m^\dagger a_m)$. Exactly as for the two-path case losses are modelled by placing imaginary beam splitters with transmissivity η_m on each of the M paths. In an experiment it is likely that most of the particle losses will occur from the q paths containing a phase shift. As such we expect η_p to be less than η_f where η_p is the transmissivity of the imaginary beam splitters on the phase paths and η_f is the transmissivity of the imaginary beam splitters on the phase free paths. The F_Q can then be calculated in a similar way to the two-path case making use of the fact that a classical state is equivalent to N single-particle NOON states and that $F_{Q_{UM}} = Np_{00\ldots0}F_Q[\xi_{00\ldots0}(\phi)]$. Here

$$|\xi_{00\ldots0}(\phi)\rangle = \frac{1}{\sqrt{Mp_{00\ldots0}}}(\sqrt{\eta_p}e^{i\phi}|1,0,\ldots,0\rangle_{12\ldots M} + \sqrt{\eta_p}e^{i\phi}|0,\ldots,1,\ldots,0\rangle_{1\ldots q\ldots M} + \ldots + \sqrt{\eta_f}|0,\ldots,1,\ldots,0\rangle_{1\ldots q+1\ldots M} + \ldots + \sqrt{\eta_f}|0,0,\ldots 1\rangle_{12\ldots M}) \tag{8.18}$$

and

$$p_{00\ldots0} = \frac{1}{M}\left(q\eta_p + (M-q)\eta_f\right). \tag{8.19}$$

Using this model it can be shown that, for a particular η_p and η_f, F_Q is given by

$$F_{Q_{UM}} = 4N\left(\frac{(1-z)\,\eta_p\eta_f}{\eta_p + (z^{-1}-1)\,\eta_f}\right) \tag{8.20}$$

where $z = q/M$. We find the F_Q is maximised when

$$z_{optU} = 1/(1+\sqrt{\Gamma}) \tag{8.21}$$

where $\Gamma = \eta_p/\eta_f$. This tells us the optimum ratio of phase paths to total number of paths for a given η_p, η_f and N. Intuitively we see that, in general, the more paths the interferometer has the better as the larger M is the more likely we are able to reach the optimum q/M ratio. Substituting equation 8.21 into equation 8.20 gives the SIL (see equation 8.14) where $\eta_p = \eta_0$ and $\eta_f = \eta_1$.

Here we have presented an alternate way to optimise the precision of classical interferometry. Unlike the strategy introduced in reference [2] this method does not require a beam splitter of variable transmissivity. Instead the optimisation is achieved by varying the number of phase paths and M. However, in both cases the F_Q is improved by as much as a factor of 2 over an interferometer set-up employing only a two-mode 50:50 beam splitter. In both systems this improvement in precision is achieved by finding a balance between the need to increase the number of particles on the lossy path(s) so as to increase the number of superpositions that exist after loss with the desire to lose as few particles as possible. Whilst multipath interferometers may prove difficult to implement this is a nice demonstration of just some of their potential.

Reference [2] also discussed how NOON state precision can be optimised in a similar way by altering the amplitudes x_0 and x_N as shown earlier in this chapter. Again, this same F_Q can be achieved using a multipath interferometer. We define a

M-path NOON state as

$$|\psi_{in}\rangle = \frac{1}{\sqrt{M}}(|N,0,0,0\ldots\rangle + |0,N,0,0\ldots\rangle + \ldots + |\ldots 0,0,0,N\rangle) \tag{8.22}$$

where the terms in the kets represent the number of particles in each path. We find that for a M-path NOON state with phase ϕ on q paths

$$F_{Q_{MN}} = 4N^2 \left(\frac{(1-z)\,\eta_p^N \eta_f^N}{\eta_p^N + (z^{-1}-1)\,\eta_f^N} \right) \tag{8.23}$$

where η_p, η_f and z are as before. Maximising $F_{Q_{MN}}$ gives the optimum ratio of the number of phase paths to total number of paths as $z_{optN} = 1/(1+\sqrt{\Gamma^N})$. Substituting z_{optN} into equation 8.23 gives $F_{Q_{NOON,max}}$ (see equation 8.12).

This has been one demonstration of a potential increase in precision offered by multimode interferometry. With the numerous possible configurations of a multimode interferometer it is expected other gains may also be found and this will be the subject of future work.

8.4 Conclusion

This work is by no means complete and as such will be discussed again in the future work section of this thesis. We have, however, demonstrated an experimentally accessible way to improve the precision of two-mode interferometers to close to that of the theoretical optimum. All that is required is a two-port beam splitter of variable transmissivity and the ability to control the number of particles incident on each of its input ports. A potential use of multimode interferometers has also been introduced. We have shown that instead of varying the transmissivity of a two-mode beam splitter, the SIL can be achieved using a M-path interferometer and varying the number of phase paths. This is likely to be only one of many potential advantages of multimode interferometry.

Chapter 9

Conclusions

We now take a moment to review the main results of the thesis and discuss how these results have achieved our initial aim, namely, to improve the practical precision of phase measurements, in particular phase measurements corresponding to rotations, by creating initial states that allow for (close to) Heisenberg limited precision in an idealised setting, yet that are robust to the effects of particle loss meaning this precision is not destroyed in a realistic experimental set-up.

Interferometers offer unrivalled precision in the measurement of phase shifts. These phase shifts could correspond to any one of a number of different physical quantities such as a difference in field strength or a rotation rate, as is the case in this thesis. We reviewed the process of interferometry in Chapter 3 and introduced the quantum Fisher information which provided a simple way to quantify the precision with which an interferometer can measure a phase independent of the measurement procedure. This therefore allowed us to focus solely on the precision potential of different initial states without having to concern ourselves with ways to optimise the read-out procedure which would be another project in itself. In this same chapter we introduced two important precision bounds, the standard quantum limit where the precision scales as $1/\sqrt{N}$ and the Heisenberg limit where the precision scales as $1/N$, which is the best precision allowed by quantum mechanics. We also introduced the initial states responsible for these bounds; the classical initial state and the highly

entangled NOON state.

However, this was nothing new as it has long been known that the precision of phase measurements can be improved using highly entangled states. The problem, however, is how to create such entangled states with large numbers of particles and how to keep the Heisenberg limited precision in the presence of particle loss, because, as was demonstrated in Chapter 3 the NOON state rapidly loses its precision capabilities as the probability of particle loss is increased. As such, to date, practical precision schemes use classical initial states as their measurement resource. In the remainder of the thesis we therefore set about trying to find and create initial states that allowed for Heisenberg (or close to Heisenberg) limited precision and that were robust to the effects of particle loss. Two of the proposed schemes focussed on phase shifts corresponding to rotations and the final scheme considered the more general case of a linear interferometer.

9.1 Main results

In order to measure rates of rotation we first needed to develop a way to create superpositions of atoms flowing in opposite directions around a ring. As such we proposed a scheme to create multiport atomic beam splitters where the input and output ports were arranged in a ring geometry. In Chapter 6 we showed how the resulting three port beam splitter allowed for these superpositions to be created. We considered the ring of three sites as this is the fewest number of sites required to create a ring, however, the four and five port beam splitters should also be capable of achieving similar superpositions. This would be an interesting field for future research as the more sites the ring has, the more momentum states the system can occupy which may allow for more precise and/or more robust phase measurements.

We developed two schemes capable of measuring rotation rates. The first scheme used a ring of lattice sites and the multiport devices developed in Chapter 5. We showed how to create three different initial states in this system and determined the precision of each. We found a bat state, which is similar to a NOON state in that it

has a large number variance but dissimilar in that the detection of one of the atoms does not betray the whereabouts of the remaining atoms, allowed for approximately Heisenberg limited precision and was robust to the effects of particle loss. It beat the precision capabilities of both the NOON and classical initial states for modest loss rates making it a great candidate for the initial state of precision measurement schemes. Its success, however, was short lived as in the following chapter an initial state was created that allowed for exactly Heisenberg limited precision in an idealised setting and that demonstrated similar robustness to particle loss as the classical initial state. It therefore outperformed the precision capabilities of both the NOON and unentangled initial states for all loss rates. To our knowledge, no initial state, has ever been shown to be so precise and robust and consequently this state is of fundamental interest to the metrology community. The origin of the robustness is the spreading of particle observables over many momentum modes rather than just two. This motivated us to begin investigating the potential of multimode interferometers to make precise and robust phase measurements in the following chapter.

We considered a general multimode interferometer scheme and showed how, by balancing the number of paths with the number of phase shifts depending on the loss rate, a factor of two improvement in the quantum Fisher information over a standard two-path interferometer was possible. However, it is thought other advantages may soon be found as discussed in the future work section. Chapter 8 also looked at standard two-path interferometry in more detail and developed an experimentally accessible way to optimise the initial state depending on the rate of loss. The precisions achieved by this set-up were shown, under certain experimentally realistic conditions, to be comparable to those achieved by the theoretical optimum two-mode initial state proposed in references [1, 2].

So, to conclude, we have achieved our original aim: we have investigated the precision capabilities of different initial states and through these investigations found states, such as the bat and TG cat state, that allow for precise and robust phase measurements. We have also developed schemes capable of producing such states, mak-

ing their promised improvements in precision/robustness over the classical/NOON initial states experimentally realistic and of fundamental interest to the metrology community.

9.2 Proposals for future work

Whilst the work presented in this thesis has gone some way towards improving the precision of phase measurements in the presence of particle loss there is still much more to be investigated. The field of multipath interferometry in particular, holds a great deal of promise as was demonstrated in Chapters 7 and 8. However, due to the many possible phases that could be applied to the paths and the many possible ways particles could be lost, the results of these chapters by no means give a complete understanding of the precision capabilities of multipath interferometry. Here we discuss several ideas that could shine light on its true potential.

9.2.1 Theoretical optimum multimode initial state in a lossy environment

References [1, 2] recently calculated the optimum initial state for a two-mode interferometer in the presence of particle loss, as discussed in detail in Chapter 8. An interesting avenue of research would be to determine the optimum initial state, and the precision achieved by this state, for the equivalent multimode interferometer. Preliminary results suggest that when the phases on the multipath interferometer are arranged as in Chapter 8 (i.e. phase ϕ on q paths, where ϕ is the phase on one path of the two-mode interferometer) the optimum multimode initial state achieves the same precision as the optimum two-mode initial state for the case of equal loss on all paths. If, however, we were to let the phase increase linearly between paths, as may be the case in a potential field, the results of Chapter 7 suggest that the precision of a two-mode interferometer could be beaten for all loss rates. Not only this, the precision in the idealised setting in which no particles are lost has already been shown to scale as $1/(MN)$ (where M is the number of paths).

9.2.2 Multimode 'bat' states

After demonstrating the success of the two-mode bat state for precise and robust phase measurements in Chapter 6 it would be interesting to determine the precision capabilities of multimode bat states, that is the output of a balanced multiport beam splitter (described by the unitary matrix of equation 8.17) into which the state $|N/M, N/M, \ldots, N/M\rangle$ is input. A two and three mode bat state are shown in figure 9.1. As can be seen spreading the particle observables over many modes in this manner is likely to lead to a slight worsening of precision in the idealised case due to a decrease in the number variance, but it may lead to better robustness as the loss of a particle will give away even less information about the whereabouts of the remaining $N-1$ particles.

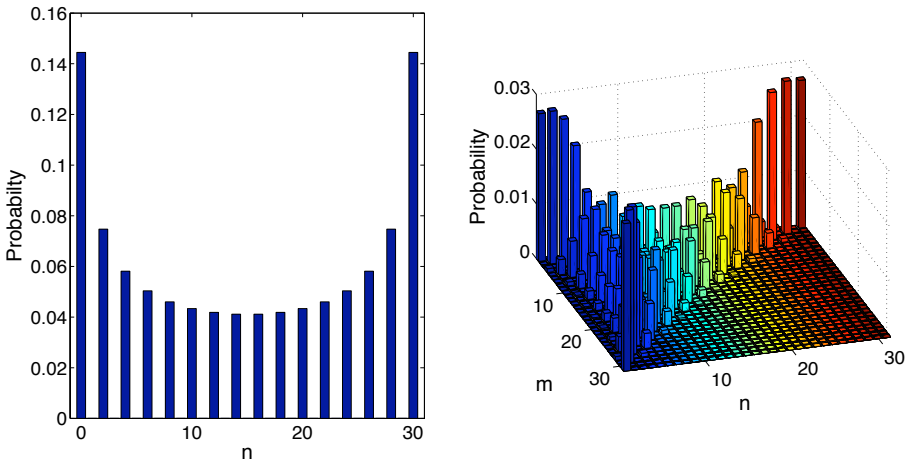

Figure 9.1: Left: A plot of the probability of having n particles in one of the output modes of a two-port 50:50 beam splitter into which $|N/2, N/2\rangle$ is input i.e. a two-mode bat state. Right: A plot of the probability of having n and m particles in two of the output modes of a balanced three-port beam splitter into which $|N/3, N/3, N/3\rangle$ is input i.e. a three-mode bat state. In both plots $N = 30$.

9.2.3 Read-out schemes

Another obvious area for future research would be to investigate ways to optimise the read-out of the phase shifts. Throughout this thesis we have focused solely on improving precision by optimising the initial state. We were able to do this by calcu-

lating the quantum Fisher information of the various interferometer schemes in their middle sections i.e. after the phase shift but before the read-out procedure. It is always theoretically possible to achieve the precisions calculated from the quantum Fisher information and as such we have not concerned ourselves with read-out procedures thus far. It may, however, sometimes prove difficult to find experimentally accessible read-out schemes that achieve these precisions. Consequently investigations will be required to find read-out schemes that allow ϕ to be determined with the precision calculated from the quantum Fisher information.

9.2.4 Extending the work on multiport beam splitters

A slightly different avenue of research would be to extend the work of Chapter 5 where a scheme to create balanced multiport splitting devices was developed. In this chapter we had a ring of S lattice sites which corresponded to the input (and output) ports of a S port beam splitter. We showed how, by a careful raising and lowering of the potential barriers between sites, it was possible to create a balanced splitting device. We were not, however, concerned with the phases generated by this splitting procedure and as such the matrix operators of these multiport devices are not those commonly quoted in the literature i.e. the matrix given by equation 8.17.

In Chapter 6 we demonstrated how it is possible to imprint phases on the individual lattice sites by applying energy off-sets to a particular site for a fixed time. It would therefore be interesting to see if, by imprinting phases on the sites both before and after the raising and lowering of the barriers, the overall phases of the device could be made to match those of equation 8.17. This could prove useful in an extension of the atomic gyroscope scheme of Chapter 6 as in the present scheme we only considered a superposition of two different flow states which meant we did not require the phases produced by the splitting device and the phase imprinting procedure to exactly match those of equation 8.17. If however, we wanted to create a superposition of three flows we would require an exact match. Similarly if we were to use more than three sites the phases would, once again, become more

important. Spreading particle observables over more flow states may allow for more robust phase measurements and as such this extension may prove useful.

9.3 To conclude

During the course of this thesis we have developed an understanding of the interplay between the precision and the robustness of initial states of an interferometer. We have demonstrated ways to create several different initial states that balance this interplay, allowing for precise yet robust phase measurements. Interestingly we have shown how by using a multimode Hilbert space unprecedented precision can be achieved in a lossy environment. This result is likely to have far reaching consequences. In particular, it is likely to motivate further research into the precision capabilities of multimode systems and may ultimately alter the way precision measurements are made.

Appendix A

Multiport devices: the differences between odd and even S

A.1 Proof of equation 5.14

In Chapter 5 section 5.3.2 we discussed differences between multiport atomic devices with an even and an odd number of lattice sites. One of the main differences we found was that the phase between adjacent sites varied by a fixed amount of $\pm\pi/2$ for systems with an even number of sites, whilst for systems with an odd number of sites it varied continuously in time. This, in turn, meant that particles moved with a fixed velocity in systems with an even S and a velocity that changed with time in systems with an odd S. The constraint of a fixed particle velocity meant it was harder for systems with an even number of sites to form a balanced splitter than for those with an odd number of sites.

Here we prove that the phase between sites for even values of S is always $\pm\pi/2$. We do this by considering the Ω_x terms of equation 5.11 as the phase of these terms directly corresponds to the phase of the sites. We begin by considering the general

Appendix A. Multiport devices: the differences between odd and even S

form of Ω_x

$$\Omega_x = \frac{1}{S}\sum_{n=0}^{S-1} e^{i2Jt\cos(2\pi n/S)+i2\pi nx/S}. \tag{A.1}$$

In order to show that the phase between adjacent sites varies by $\pm\pi/2$ for even values of S we need to show that we can rewrite the above equation for Ω_x as

$$\Omega_x = e^{i\pi x/2}\Lambda(S,J,t,x) \tag{A.2}$$

where $\Lambda(S,J,t,x)$ is some real valued function (i.e. equation 5.14). To do this we rewrite equation A.1 as

$$\begin{aligned}\Omega_x &= \frac{1}{S}\sum_{n=0}^{S/2-1}\left(e^{i2Jt\cos(2\pi n/S)+i2\pi nx/S} + e^{i2Jt\cos(2\pi(n+S/2)/S)+i2\pi(n+S/2)x/S}\right)\\ &= \frac{2e^{i\pi x/2}}{S}\sum_{n=0}^{S/2-1} e^{i2\pi nx/S}\cos\left(2Jt\cos\left(\frac{2\pi n}{s}\right)-\frac{\pi x}{2}\right).\end{aligned} \tag{A.3}$$

We must now show that

$$\lambda(S,J,t,x) = \sum_{n=0}^{S/2-1} e^{i2\pi nx/S}\cos\left(2Jt\cos\left(\frac{2\pi n}{S}\right)-\frac{\pi x}{2}\right) \tag{A.4}$$

is always real.

We first rewrite $\lambda(S,J,t,x)$ as

$$\begin{aligned}\lambda(S,J,t,x) &= \cos\left(2Jt-\frac{\pi x}{2}\right)+\sum_{n=1}^{S/2-1} e^{i2\pi nx/S}\cos\left(2Jt\cos\left(\frac{2\pi n}{s}\right)-\frac{\pi x}{2}\right)\\ &= \cos\left(2Jt-\frac{\pi x}{2}\right)+\sum_{n=1}^{S/2-1}\Pi(S,J,t,x,n).\end{aligned} \tag{A.5}$$

The $\cos(2Jt-\pi x/2)$ term is real for all x. In order to prove $\lambda(S,J,t,x)$ is real we must therefore show that the second term in the equation is also real. We do this by pairing terms in the sum, that is, we shall show that for $n=z$, $\Pi(S,J,t,x,z) = R_z e^{i2\pi xz/S}$ (where $1\le z\le S/4$ is an integer and R_z is some real number) whilst for $n=S/2-z$, $\Pi(S,J,t,x,S/2-z) = R_z e^{-i2\pi xz/S}$. Summing these two terms therefore results in

a real number. For $S = 4y - 2$ where y is an integer, $S/2 - 1$ is even meaning all the terms in the above summation pair in this manner. For $S = 4y$, $S/2 - 1$ is odd meaning all the terms except $n = S/4$ pair in this way. When $n = S/4$

$$\Pi(S, J, t, x, S/4) = e^{i\pi x/2} \cos\left(\frac{\pi x}{2}\right) \tag{A.6}$$

which is equal to 0 for odd x and 1 for even x. This term is therefore always real and so providing we can show that all the $n = z$ and $n = S/2 - z$ pairs sum to give a real number we will have shown that $\lambda(S, J, t, x)$ is real.

To prove the pairs sum to a real number we split the possible values of x into four groups: $4y$, $4y - 2$, $4y - 1$ and $4y - 3$. If we can prove that $\lambda(S, J, t, x)$ is real for each of these x values we will have shown it is real for all possible values of x. Let us first take the case of $x = 4y$. For $n = z$ we have

$$\Pi(S, J, t, 4y, z) = e^{i8\pi zy/S} \cos\left(2Jt \cos\left(\frac{2\pi z}{s}\right)\right) \tag{A.7}$$

and for $n = S/2 - z$ we have

$$\Pi(S, J, t, 4y, S/2 - z) = e^{-i8\pi zy/S} \cos\left(2Jt \cos\left(\frac{2\pi z}{s}\right)\right). \tag{A.8}$$

We therefore see that when these two terms are added together the result is a real number. Similarly for $x = 4y - 2$ we have

$$\Pi(S, J, t, 4y - 2, z) = -e^{i2\pi z(4y-2)/S} \cos\left(2Jt \cos\left(\frac{2\pi z}{s}\right)\right) \tag{A.9}$$

for $n = z$ and

$$\Pi(S, J, t, 4y - 2, S/2 - z = -e^{-i2\pi z(4y-2)/S} \cos\left(2Jt \cos\left(\frac{2\pi z}{s}\right)\right) \tag{A.10}$$

for $n = S/2 - z$. Once again the sum of these two terms is a real number. Repeating for $x = 4y - 1$ and $x = 4y - 3$ we find the sum of the $n = z$ and $n = S/2 - z$ pair

is always a real number. Since every pair is a real number the sum of all the pairs must therefore also be a real number. We have therefore shown that $\lambda(S, J, t, x)$ is a real number and consequently that the phase difference between Ω_x and Ω_{x+1} (and hence sites j and $j+1$) is $\pi/2$.

For the case of an odd number of lattice sites the same pairings are not possible. Instead we find that the phase between Ω_x and Ω_{x+1} varies with time.

A.2 The number of different Ω for S even and S odd

A second difference we found between devices with even and odd numbers of lattice sites is that the number of different values of Ω for odd values of S is $(S+1)/2$ whilst for even values of S it is $(S+2)/2$. This again supports the observation that it is harder for devices with even numbers of sites to produce balanced splitters than for those with odd numbers as there are more different Ω to match (as a fraction of the total S). Here we show why the number of different Ω for odd values of S is $(S+1)/2$ and why it is $(S+2)/2$ for even values of S.

The general Ω_x is given in equation A.1. The subscript x can take any integer value in the range $0 \leq x \leq S-1$ suggesting there are S different values of Ω for all S. However, as we shall now show $\Omega_x = \Omega_{S-x}$ for integer values of x in the range 1 to $(S-1)/2$. Consequently, since $S-1$ is even for odd values of S all the Ω_x pair up in this manner except Ω_0. The number of different Ω is therefore easily seen to be $(S+1)/2$. For even values of S, however, both $x=0$ and $x=S/2$ have no pair meaning the total number of different Ω is $(S+2)/2$ (since $\Omega_0 \neq \Omega_{S/2}$).

To show that $\Omega_x = \Omega_{S-x}$ we begin by writing Ω_x in the form

$$\begin{aligned} \Omega_x &= \frac{1}{S}\left(e^{i2Jt} + \sum_{n=1}^{S-1} e^{i2Jt\cos(2\pi n/S)+i2\pi xn/S}\right) \\ &= \frac{1}{S}\left(e^{i2Jt} + \sum_{n=1}^{S-1} \Theta_1(S, J, t, x, n)\right) \end{aligned} \tag{A.11}$$

and Ω_{S-x} in the form

$$\begin{aligned}\Omega_{S-x} &= \frac{1}{S}\left(e^{i2Jt} + \sum_{n=1}^{S-1} e^{i2Jt\cos(2\pi n/S)+i2\pi(S-x)n/S}\right) \\ &= \frac{1}{S}\left(e^{i2Jt} + \sum_{n=1}^{S-1} e^{i2Jt\cos(2\pi n/S)-i2\pi xn/S}\right) \\ &= \frac{1}{S}\left(e^{i2Jt} + \sum_{n=1}^{S-1} \Theta_2(S,J,t,x,n)\right). \end{aligned} \tag{A.12}$$

Putting $n = y$ (where y is an integer in the range $1 \leq y \leq S-1$) into $\Theta_1(S,J,t,x,n)$ gives

$$\Theta_1(S,J,t,x,y) = e^{i2Jt\cos(2\pi y/S)+i2\pi yx/S} \tag{A.13}$$

whilst putting $n = S - y$ into $\Theta_2(S,J,t,x,n)$ gives

$$\Theta_2(S,J,t,x,S-y) = e^{i2Jt\cos(2\pi y/S)+i2\pi yx/S} \tag{A.14}$$

and so $\Theta_1(S,J,t,x,y) = \Theta_2(S,J,t,x,S-y)$. We see, therefore, that

$$\begin{aligned}\Theta_1(S,J,t,x,1) &= \Theta_2(S,J,t,x,S-1) \\ \Theta_1(S,J,t,x,2) &= \Theta_2(S,J,t,x,S-2) \\ \vdots &= \vdots \\ \Theta_1(S,J,t,x,S-2) &= \Theta_2(S,J,t,x,2) \\ \Theta_1(S,J,t,x,S-1) &= \Theta_2(S,J,t,x,1) \end{aligned} \tag{A.15}$$

and consequently

$$\sum_{n=1}^{S-1} \Theta_1(S,J,t,x,n) = \sum_{n=1}^{S-1} \Theta_2(S,J,t,x,n). \tag{A.16}$$

It therefore directly follows that $\Omega_x = \Omega_{S-x}$.

Bibliography

[1] U. Dorner *et al.*, Phys. Rev. Lett. **102**, 040403 (2009).

[2] R. Demkowicz-Dobrzański *et al.*, Phys. Rev. A **80**, 013825 (2009).

[3] E. Schrödinger, Naturwissenschaften **23**, 807 (1935).

[4] C. Jönsson, Zeits. f. Physik **161**, 454 (1961).

[5] C. Jönsson, Zeits. f. Physik **42**, 4 (1974).

[6] A. Tonomura *et al.*, Am. J. Phys. **57**, 117 (1989).

[7] P. W. Shor, J. Sci. Statist. Comput. **26**, 1484 (1997).

[8] C. H. Bennett *et al.*, Phys. Rev. Lett. **70**, 1895 (1993).

[9] C. H. Bennett and G. Brassard, Proceedings of the IEEE International Conference on Computers, Systems and Signal Processing 175 (1984).

[10] W. Heisenberg, Zeitschrift für Physik **43**, 172 (1927).

[11] C. Gross *et al.*, Nature **464**, 1165 (2010).

[12] M. Zwierz, C. A. Pérez-Delgado, and P. Kok, Phys. Rev. Lett. **105**, 180402 (2010).

[13] D. Jaksch *et al.*, Phys. Rev. Lett. **81**, 3108 (1998).

[14] G. Sagnac, C. R. Acad. Sci. **157**, 708 (1913).

[15] J. J. Cooper, D. W. Hallwood, and J. A. Dunningham, J. Phys. B **42**, 105301 (2009).

[16] J. J. Cooper, D. W. Hallwood, and J. A. Dunningham, Phys. Rev. A **81**, 043624 (2010).

[17] J. J. Cooper, D. W. Hallwood, and J. Brand, arxiv:1101.3852 (2011).

[18] S. Bose, Z. Phys. **26**, 178 (1924).

[19] A. Einstein, Sitzungber. Preuss. Akad. Wiss. **1925**, 3 (1925).

[20] P. Kapitsa, Nature **141**, 74 (1938).

[21] J. F. Allen and A. D. Misener, Nature **141**, 75 (1938).

[22] F. London, Nature **141**, 643 (1938).

[23] F. London, Phys. Rev. **54**, 947 (1938).

[24] D. G. Fried *et al.*, Phys. Rev. Lett. **81**, 3811 (1998).

[25] M. H. Anderson *et al.*, Science **269**, 198 (1995).

[26] K. B. Davis *et al.*, Phys. Rev. Lett. **75**, 3969 (1995).

[27] C. C. Bradley, C. A. Sackett, J. J. Tollett, and R. G. Hulet, Phys. Rev. Lett. **75**, 1687 (1995).

[28] W. D. Phillips, Rev. Mod. Phys. **70**, 721 (1998).

[29] O. R. Frisch, Z. Physik **86**, 42 (1933).

[30] D. Wineland and H. Dehmelt, Bull. Am. Phys. Soc. **20**, 637 (1975).

[31] T. W. Hänsch and A. L. Schawlow, Opt. Comm. **13**, 68 (1975).

[32] S. Chu *et al.*, Phys. Rev. Lett. **55**, 48 (1985).

[33] H. F. Hess, Phys. Rev. B **34**, 3476 (1986).

[34] O. Morsch and M. Oberthaler, Rev. Mod. Phys. **78**, 179 (2006).

[35] I. Bloch, Nature Physics **1**, 23 (2005).

[36] V. Boyer *et al.*, Phys. Rev. A **73**, 031402(R) (2006).

[37] K. Henderson, C. Ryu, C. MacCormick, and M. G. Boshier, New J. Phys. **11**, 043030 (2009).

[38] D. Jaksch and P. Zoller, Ann. Phys. **315**, 52 (2005).

[39] A. Rey *et al.*, J. Phys. B **36**, 825 (2003).

[40] V. Giovannetti, S. Lloyd, and L. Maccone, Science **306**, 1330 (2004).

[41] S. L. Braunstein and C. M. Caves, Phys. Rev. Lett. **72**, 3439 (1994).

[42] C. M. Caves, Phys. Rev. D **23**, 1693 (1981).

[43] R. E. Slusher *et al.*, Phys. Rev. Lett. **55**, 2409 (1985).

[44] M. Xiao, L. A. Wu, and H. J. Kimble, Phys. Rev. Lett. **59**, 278 (1987).

[45] P. Grainger, R. E. Slusher, B. Yurke, and A. LaPorta, Phys. Rev. Lett. **59**, 2153 (1987).

[46] B. Yurke, Phys. Rev. Lett. **56**, 1515 (1986).

[47] L. Pezzé and A. Smerzi, Phys. Rev. Lett. **100**, 073601 (2008).

[48] C. K. Hong, Z. Y. Ou, and L. Mandel, Phys. Rev. Lett. **59**, 2044 (1987).

[49] P. Kok, H. Lee, and J. P. Dowling, Phys. Rev. A **65**, 052104 (2002).

[50] G. Pryde and A. White, Phys. Rev. A **68**, 052315 (2003).

[51] J. A. Dunningham and K. Burnett, J. Mod. Opt. **48**, 1837 (2001).

[52] J. Dunningham and D. Hallwood, Phys. Rev. A **74**, 023601 (2006).

[53] X.-B. Zou, J. Kim, and H.-W. Lee, Phys. Rev. A **63**, 065801 (2001).

[54] M. W. Mitchell, J. S. Lundeen, and A. M. Steinberg, Nature **429**, 161 (2004).

[55] C. A. Sackett, D. Kielpinski, and B. E. King, Nature **404**, 256 (2000).

[56] T. Nagata *et al.*, Science **316**, 726 (2007).

[57] P. Walther *et al.*, Nature (London) **429**, 158 (2004).

[58] I. Afek, O. Amber, and Y. Silberberg, Science **328**, 879 (2010).

[59] J. A. Jones *et al.*, Science **324**, 1166 (2009).

[60] M. J. Holland and K. Burnett, Phys. Rev. Lett. **71**, 1355 (1993).

[61] J. A. Dunningham, K. Burnett, and S. M. Barnett, Phys. Rev. Lett. **89**, 150401 (2002).

[62] J. A. Dunningham and K. Burnett, Phys. Rev. A **61**, 065601 (2004).

[63] Z. Hradil and J. Řeháček, Phys. Lett. A **334**, 267 (2005).

[64] N. L. Thomas-Peter, B. J. Smith, and I. A. Walmsley, arxiv:1007.0870v1 (2010).

[65] H. S. Eisenberg, J. F. Hodelin, G. Khoury, and D. Bouwmeester, Phys. Rev. Lett. **94**, 090502 (2005).

[66] K. T. Kapale and J. P. Dowling, Phys. Rev. Lett. **99**, 053602 (2007).

[67] J. Esteve *et al.*, Nature **455**, 1216 (2008).

[68] B. L. Higgins *et al.*, Nature **450**, 393 (2007).

[69] B. L. Higgins *et al.*, New J. Phys. **11**, 073023 (2009).

[70] R. Demkowicz-Dobrzański, Laser Physics **20**, 1197 (2010).

[71] S. Boixo *et al.*, Phys. Rev. Lett. **101**, 040403 (2008).

[72] S. Boixo, S. T. Flammia, C. M. Caves, and J. M. Geremia, Phys. Rev. Lett. **98**, 090401 (2007).

[73] S. M. Roy and S. L. Braunstein, Phys. Rev. Lett. **100**, 220501 (2008).

[74] T.-W. Lee *et al.*, Phys. Rev. A **80**, 063803 (2009).

[75] S. D. Huver, C. F. Wildfeuer, and J. P. Dowling, Phys. Rev. A **78**, 063828 (2008).

[76] J. J. Bollinger, W. M. Itano, D. J. Wineland, and D. J. Heinzen, Phys. Rev. A **54**, R4649 (1996).

[77] S. F. Huelga *et al.*, Phys. Rev. Lett. **79**, 3865 (1997).

[78] A. N. Boto *et al.*, Phys. Rev. Lett. **85**, 2733 (2000).

[79] M. D'Angelo, M. V. Chekhova, and Y. Shih, Phys. Rev. Lett. **87**, 013602 (2001).

[80] T. L. Gustavson, A. Landragin, and M. A. Kasevich, Class. Quantum Grav. **17**, 2385 (2000).

[81] A. A. Michelson, Astrophys. J **61**, 137 (1925).

[82] J. F. Clauser, Physica B & C **151**, 262 (1988).

[83] F. Riehle *et al.*, Phys. Rev. Lett. **67**, 177 (1991).

[84] O. I. Tolstikhin, T. Morishita, and S. Watanabe, Phys. Rev. A **72**, 051603(R) (2005).

[85] Y.-J. Wang *et al.*, Phys. Rev. Lett. **94**, 090405 (2005).

[86] S. Gupta *et al.*, Phys. Rev. Lett. **95**, 143201 (2005).

[87] P. L. Halkyard, M. P. A. Jones, and S. A. Gardiner, Phys. Rev. A **81**, 061602 (2010).

[88] J. P. Dowling, Phys. Rev. A **57**, 4736 (1998).

[89] G. M. D'Ariano and M. G. A. Paris, Phys. Rev. A **55**, 2267 (1997).

[90] J. Dunningham and T. Kim, J. Mod. Opt. **53**, 557 (2006).

[91] M. Reck, A. Zeilinger, H. J. Bernstein, and P. Bertani, Phys. Rev. Lett. **73**, 58 (1994).

[92] S. Zhang, C. Lei, A. Vourdas, and J. A. Dunningham, J. Phys. B **39**, 1625 (2006).

[93] A. Vourdas and J. Dunningham, Phys. Rev. A **71**, 013809 (2005).

[94] J. A. Dunningham and A. Vourdas, J. Phys. B **39**, 1579 (2006).

[95] K. Mattle *et al.*, Appl. Phys. B **60**, S111 (1995).

[96] T. Rasmussen, A. Bjarklev, and J. H. Povlsen, Electronics Lett. **30**, 583 (1994).

[97] M. Greiner, O. Mandel, T. W. Hänsch, and I. Bloch, Nature (London) **419**, 51 (2002).

[98] S. Cornish *et al.*, Phys. Rev. Lett. **85**, 1795 (2000).

[99] L. Amico, A. Osterloh, and F. Cataliotti, Phys. Rev. Lett. **95**, 063201 (2005).

[100] J. A. Dunningham and K. Burnett, Phys. Rev. A **70**, 033601 (2004).

[101] S. Scheel, J. Pachos, E. A. Hinds, and P. L. Knight, Lect. Notes Phys. **689**, 47 (2006).

[102] M. Jona-Lasinio *et al.*, Phys. Rev. Lett. **91**, 23 (2003).

[103] T. Y. Kwon *et al.*, Jpn. J. Appl. Phys. **42**, 924 (2003).

[104] M. Albiez *et al.*, Phys. Rev. Lett. **95**, 010402 (2005).

[105] C. Chin, R. Grimm, P. Julienne, and E. Tiesinga, arxiv:0812.1496v1 (2008).

[106] F. K. Fatemi and M. Bashkansky, Opt. Lett. **31**, 7 (2006).

[107] T. L. Gustavson, P. Bouyer, and M. A. Kasevich, Phys. Rev. Lett. **78**, 2046 (1997).

[108] C. P. Search, J. R. E. Toland, and M. Zivkovic, Phys. Rev. A **79**, 053607 (2009).

[109] S. Thanvanthri, K. T. Kapale, and J. P. Dowling, arXiv:0907.1138v1 (2009).

[110] J. Denschlag *et al.*, Science **287**, 97 (2000).

[111] D. W. Hallwood, T. Ernst, and J. Brand, Phys. Rev. A **82**, 063623 (2010).

[112] D. W. Hallwood, K. Burnett, and J. Dunningham, J. Mod. Opt. **54**, 2129 (2007).

[113] M. Girardeau, J. Math. Phys. **1**, 516 (1960).

[114] A. Lenard, J. Math. Phys. **5**, 930 (1964).

[115] T. Kinoshita, T. Wenger, and D. S. Weiss, Science **305**, 1125 (2004).

[116] B. Paredes *et al.*, Nature **429**, 277 (2004).

[117] L. Maccone and G. D. Cillis, Phys. Rev. A **79**, 023812 (2009).

[118] K. Banasek, R. Demkowicz-Dobrzański, and I. A. Walmsley, Nature Photonics **3**, 673 (2009).

[119] M. Kacprowicz *et al.*, Nature Photonics **4**, 357 (2010).

[120] S. K. Sheem, J. Appl. Phys. **52**, 3865 (1981).

[121] B. C. Sanders, H. de Guise, D. J. Rowe, and A. Mann, J. Phys. A **32**, 7791 (1999).

[122] A. Luis, J. Phys. A **34**, 8597 (2001).

[123] J. Söderholm, G. Björk, B. Hessmo, and S. Inoue, Phys. Rev. A **67**, 053803 (2003).